Structural Properties of Superconducting Bi-2223/Ag Tapes

Egeberg, Lotte Gottschalck

Publication date:
2001

Document Version
Publisher's PDF, also known as Version of record

Risø–R–1271(EN)

Structural Properties of Superconducting Bi-2223/Ag Tapes

Lotte Gottschalck Andersen

Risø National Laboratory, Roskilde, Denmark
May 2001

Abstract

The structural properties of silver clad high-T_c superconducting ceramic tapes of $(Bi,Pb)_2Sr_2Ca_2Cu_3O_x$ (Bi-2223) have been investigated by means of synchrotron X-ray diffraction, transmission electron microscopy (TEM) and scanning electron microscopy (SEM) with energy dispersive X-ray analysis (EDS).

By synchrotron X-ray diffraction *in situ* studies of the phase development during the transformation of $(Bi,Pb)_2Sr_2Ca_1Cu_2O_x$ (Bi-2212) into Bi-2223, the stoichiometry changes and the texture have been performed during annealing in 8% O_2 and in air. Furthermore, an annealing with a slow ramping (from 750 °C) followed by two high temperature cycles has been performed to study the equilibrium phenomena. In addition, a tape beforehand fully converted into Bi-2223 was studied *in situ* during a last annealing.

During heating the $(Ca,Sr)_2PbO_4$ phase is observed to decompose at temperatures between 700 °C and 840 °C. Simultaneously, the Bi-2212 lattice contracts, indicating an incorporation of Pb. Moreover, the grain mis-alignment decreases significantly. In air we have observed that Bi-2212 partly dissociates into $(Ca,Sr)_2CuO_3$ and a liquid phase at temperatures above 812 °C. At the annealing temperature Bi-2212 and the $(Ca,Sr)_2CuO_3$ phase react with the liquid to form Bi-2223. Both in 8% O_2 and in air we have observed that the final texture of Bi-2223 and Bi-2212 is identical, the Avrami plot exponents are in the range of 1–2 and the linewidth of Bi-2212 is constant during conversion into Bi-2223, indicating that no strain and finite-size broadening of the diffraction peaks occur. The transformation mechanism is discussed. During cooling in air below ∼750 °C the $(Ca,Sr)_2CuO_3$ phase and the liquid mainly transform into Bi-2201. Below ∼780 °C Bi-2223 decomposes to 3221. During cooling in 8% O_2 the Bi-2201 phase and $(Ca,Sr)_2PbO_4$ or 3221 are also observed to appear.

Using synchrotron radiation and the 3DXRD microscope setup the dynamic behavior of the individual grains within a ceramic was observed for the first time.

In addition, a two-step cooling experiment and a decomposition study have been performed in 8% O_2. The tapes were afterwards investigated by transport current measurements, SEM and synchrotron radiation. Our interpretation of the cooling experiments is that a slow cooling rate to 800 °C provides time for precipitation of a liquid phase used for mass transport when forming the Bi-2223 phase. A decomposition experiment has shown a very slow reaction where Pb-rich Bi-2223 transforms to Pb-poor Bi-2223 during post annealing at 650 °C. Simultaneously, the amount of a 3222 (Bi = 1.6 and Pb = 1.4) phase increases.

By TEM the grain and colony size in the *c*-axis direction and the angles of *c*-axis tilt grain boundaries are investigated. By high-resolution TEM the grain and grain boundaries are investigated on the atomic scale. The intergrowth content and distribution are examined. A fully processed tape has on average 50% thicker grains than a tape after the 1st annealing. The angles of *c*-axis tilt grain boundaries are on average 14° and 26° for the fully processed tape and the tape after the 1st annealing, respectively. The intergrowth content (15%) and distribution are similar in these two tapes.

Resumé

De strukturelle egenskaber af sølvindfattet høj-T_c superledende keramiske $(Bi,Pb)_2Sr_2Ca_2Cu_3O_x$ (Bi-2223) bånd er blevet undersøgt ved hjælp af synkrotron røntgendiffraktion, transmission elektronmikroskopi (TEM) og skanning elektronmikroskopi (SEM) med energi dispersiv røntgenanalyse (EDS) .

Ved hjælp af synkrotron røntgendiffraktion er *in situ* studier af faseudviklingen under omdannelsen af $(Bi,Pb)_2Sr_2Ca_1Cu_2O_x$ (Bi-2212) til Bi-2223, støkiometriændringerne og teksturen blevet udført under varmebehandlingen i 8% O_2 og i luft. Endvidere er en varmebehandling med en langsom temperaturstigning (fra 750 °C) efterfulgt af to høj-temperatur cykluser blevet udført for at studere ligevægtsfænomenerne. Yderligere er en tape, som allerede er konverteret til Bi-2223, studeret *in situ* under en sidste varmebehandling.

Under opvarmningen dekomponerer $(Ca,Sr)_2PbO_4$ fasen ved temperaturer mellem 700 °C og 840 °C. Samtidigt trækker Bi-2212 gitteret sig sammen, hvilket indikerer en inkorporation af Pb. Desuden øges ensretningen af kornene signifikant. I luft har vi observeret, at Bi-2212 delvis opløses til $(Ca,Sr)_2CuO_3$ og en væskefase ved temperaturer over 812 °C. Ved varmebehandlingstemperaturen reagerer Bi-2212 and $(Ca,Sr)_2CuO_3$ fasen med væsken for at danne Bi-2223. Både i 8% O_2 og i luft har vi observeret, at den endelige tekstur af Bi-2223 og Bi-2212 er identiske, Avrami plot eksponenterne ligger mellem 1–2 og Bi-2212 liniebredden er konstant under omdannelsen til Bi-2223, hvilket indikerer at ingen spænding og endeligstørrelse udbredning af diffraktionstoppen forekommer. Omdannelsemekanismerne diskuteres. Under afkølingen i luft under ∼750 °C omdannes $(Ca,Sr)_2CuO_3$ fasen og væsken hovedsagelig til Bi-2201. Under ∼780 °C dekomponerer Bi-2223 til 3221. Under afkøling i 8% O_2 dukker Bi-2201 og $(Ca,Sr)_2PbO_4$ eller 3221 ligeledes frem.

Ved hjælp af synkrotronstråling og 3DXRD mikroskopopsætningen er den dynamiske adfærd af de individuelle korn inde i en keramik observeret for første gang.

Yderligere er et to-trins afkølingseksperiment og et dekompositionsstudie udført i 8% O_2. Båndene blev bagefter undersøgt ved hjælp af transportstrømmålinger, SEM og synkrotronstråling. Vores fortolkning af afkølingseksperimentet er, at en langsom afkøling til 800 °C giver tid for udfældning af væskefasen, som benyttes til massetransport, når Bi-2223 fasen dannes. Et dekompositionseksperiment har udvist en langsom reaktion, hvor Pb-rig Bi-2223 omdannes til Pb-fattig Bi-2223 under efter-varmebehandlingen ved 650 °C. Samtidig øges mængden af en 3222 (Bi = 1.6 og Pb = 1.4) fase.

Ved hjælp af TEM er korn og kolonistørrelsen i *c*-akse retningen og *c*-akse vipnings korngrænsevinklerne undersøgt. Ved hjælp af højopløsnings TEM er kornene og korngrænserne undersøgt på atomar skala. Intergrowth indholdet og fordelingen er undersøgt. En fuldt processeret bånd har i gennemsnit 50% tykkere korn end et bånd efter den første varmebehandling. *c*-akse vipnings korngrænsevinklerne er i gennemsnit 14° og 26° for henholdsvis det fuldt processerede bånd og båndet efter den første varmebehandling. Intergrowth indholdet (15%) og fordelingen er ens i disse to bånd.

ISBN 87–550–2888–8
ISBN 87–550–2889–6 (Internet)
ISSN 0106–2840

Print: Danka Services International A/S · 2001

Contents

1 Introduction **8**

2 Theory **10**
2.1 Superconductivity 10
2.2 Crystal structure of Bi-2223 11

3 Experimental **16**
3.1 Tape processing 16
3.2 Samples 17
3.3 Synchrotron 18
3.3.1 Experimental setup 18
3.3.2 Data analysis 20
3.3.3 Pole figure 23
3.3.4 3DXRD 25
3.4 SEM/EDS 26
3.5 TEM 27
3.5.1 Orientation of the specimen 29
3.5.2 Equipment 31
3.5.3 Sample preparation 31

4 Phase development **33**
4.1 Phase diagram in 8% O_2 33
4.2 1st annealing in 8% O_2 34
4.2.1 Comparison with annealing in air 38
4.3 Last annealing in 8% O_2 39
4.4 Transformation kinetics 41
4.5 Equilibrium and kinetics 42
4.6 *In situ* study of individual grains by 3DXRD 44
4.7 Grain and colony thickness 46
4.8 Intergrowth 47

5 Texture **52**
5.1 Texture development 52
5.1.1 1st annealing in 8% O_2 52
5.1.2 Last annealing in 8% O_2 53
5.2 Final texture 54
5.2.1 Variation of processing 54
5.2.2 Variation of number of filaments 55
5.3 Angles of *c*-axis tilt 56
5.4 Comparison of TEM and synchrotron results 56

6 Cooling **59**
6.1 *In situ* cooling behavior 59
6.2 Two-step cooling 61
6.3 Decomposition 65

7 Summary and discussion with outlook **70**

Acknowledgements **73**

References **74**

List of papers **79**

1 Introduction

Superconductivity is a phenomenon that can be used in an impressive number of applications. Local brain activity can be observed by use of superconducting quantum interference devises (SQUID's), since these magnetometers can detect magnetic fluxes below 10^{-15} Tm^2. In the superconducting electric power technology the following applications can be mentioned: cables, superconducting magnet energy storage units (SMES), fault current limiters (FCLs), flywheel bearings, motors, generators, magnets and transformers. In Japan a 20 km long levitated high-speed transportation line has been constructed. The trains can reach speeds as high as 1000 km/h.

The energy consumption of the world is constantly increasing. Furthermore, this energy use is not evenly distributed over the day and seasons. The SMES offer a fantastic opportunity to store energy for later utilization. A superconducting magnet can produce a magnetic flux density of 10 T. A traditional electromagnet is only capable of producing 1–2 T. The magnetic resonance imaging (MRI) technique used for medical diagnostic, such as investigation of heart defects, needs a very stable static magnetic field (about 2 T), which only can be produced by a superconducting magnet.

In countries like Japan the subsoil is so densely packed that it leaves no space for further cables etc. in the future. Here the superconducting cables offer a great advantage. They are smaller and more efficient than conventional cables. Furthermore, they do not heat up. Conventional cables heat up due to the ohmic resistance and they have to be cooled with a lot of oil. The superconducting cables will reduce the energy loss by more than 40 per cent. Today the disadvantage of the superconducting cables is that the cost in \$/kAm is still too high. One way to solve this problem is to improve the superconducting core to obtain an enhancement of the critical current density J_c [1, 2, 3].

Ceramic high-T_c superconducting $(Bi,Pb)_2Sr_2Ca_2Cu_3O_x$/Ag (Bi-2223/Ag) tapes (also referred to as BSCCO (Bi-Sr-Ca-Cu-O)) are used for prototypes of the power cables[1]. In the center of the cable the tapes are wound around a former, wherein the liquid nitrogen that cools the tapes to 77 K is flowing. It is well known that the inter-grain-connectivity, grain alignment and flux pinning are some of the limiting factors of the superconducting critical current density J_c of the tapes. Today the critical current density for tapes is up to 80 kA/cm^2 [4] while thin films have $J_c = 1600$ kA/cm^2 [4]. In other words, the best J_c values obtained for tapes are only 5% of the theoretical possible value.

The purpose with the work described in this Ph.D. thesis is to further the understanding of the material properties of the Bi-2223/Ag tapes by comparing results from different advanced techniques. The overall aim is to improve the critical current density by using the obtained knowledge about the phase behavior and structure.

To fully understand the structural properties it is important to use different investigation techniques. Electromagnetic characterization methods, such as transport loss measurements, AC magnetization loss measurements and AC susceptibility measurements, are useful for examination of low frequency AC losses, produced by flux flow in the tape. The superconducting transition temperature T_c can also be found by AC susceptibility measurements. The intragranular critical current densities (the current within the grains) can be measured using DC magnetization. By comparing magnetization results and transport current measurements knowledge about whether the weak links are due to flux pinning or inter-grain-connectivity is

[1] Bi-2223/Ag tapes are also used for prototypes of SMES, FLCs, generators, magnets and transformers.

obtained. The density and distribution of micro-cracks produced during the tape processing can be investigated by magneto-optical imaging, which records the patterns of the flux penetration into the tape. Thermogravimetry investigations (DTA/TG) measure the heat exchange and weight change during the heat treatment. This technique is a useful supplement for structural investigations based on diffraction and microscopy. For structural investigation of Bi-2223/Ag tapes, techniques such as scanning electron microscopy (SEM) with energy dispersive X-ray analysis (EDS), transmission electron microscopy (TEM), X-ray diffraction (XRD) and neutron diffraction are used. Cu K_α XRD is an *ex situ* technique performed on quenched tapes. *In situ* high-temperature neutron diffraction makes it possible to examine the evolution of phase composition during heat treatment [5].

Besides transport current measurements the results presented in this thesis are obtained from SEM/EDS, TEM and synchrotron X-ray diffraction investigations[2].

High-energy synchrotron X-ray diffraction measurements give a unique possibility to examine the phase transformation, texture and stoichiometry changes during the annealing [6, 7, 8, 9]. This technique investigates the overall bulk properties by averaging over 1–2 mm^2. SEM/EDS is useful to study e.g. the secondary phases [10] and the local composition of Bi-2223 on the micrometer scale. TEM gives the opportunity to gain insight in the current path (sub-micron scale) including the grain thickness, colony thickness and the grain boundary angles [11, 12, 13]. By high-resolution TEM (HRTEM) one can investigate the grain boundaries on an atomic scale and detect the possible presence of non-superconducting phases. Also the intergrowth of Bi-22$(n-1)n$ phases with $n \neq 3$ can be studied.

This thesis is organized in the following way: Chapter 2 contains a brief introduction to the superconducting phenomenon followed by a section on the crystal structure of Bi-2223 supported by own TEM images. Chapter 3 gives information of the Bi-2223/Ag tape processing, the samples, the used experimental techniques and the data analysis. The results are divided into three chapters. The phase development and the texture studies are placed in chapter 4 and 5, respectively. In chapter 6 the emphasis has been placed on the last part of the heat treatment (cooling) due to the fact that the cooling procedure tends to degrade the quality of the tape structure. Finally, chapter 7 includes a summary of the results and a discussion with outlook.

In the thesis four papers are included. The main text can be read separately (with references to certain figures in the papers). However, additional results and details are found in Paper 1–4. Exceptionally the discussion in Paper 4 has to be read (preferable in connection with section 5.3).

This thesis contributes partly to the requirements for obtaining the Ph.D. degree at the Technical University of Denmark (DTU) at the Department of Physics. My supervisor at Risø National Laboratory (RISØ) has been senior scientist Henning Friis Poulsen at the Materials Research Department. The supervisor at DTU was initially Jørn Bindslev Hansen and finally Claus Schelde Jacobsen. The Engineering Science Center for Structural Characterization and Modeling of Material has financed the Ph.D. study. The experimental work has been performed at the Materials Research Department at RISØ, at the synchrotron facilities in Hamburg (HASYLAB) and Grenoble (ESRF) and at Electron Microscopy of Materials Science (EMAT) at the University of Antwerp (RUCA).

[2] Cu K_α XRD are used for a phase diagram study.

2 Theory

This chapter is divided into two theory parts. In section 2.1 a brief introduction to the superconducting phenomenon is given. A detailed presentation of superconductivity will be out of the scope of this thesis. For more information on the subject consult e.g. Ref. [1]. In section 2.2 the structural properties of $(Bi,Pb)_2Sr_2Ca_2Cu_3O_x$ are presented.

2.1 Superconductivity

At low temperatures some materials become superconductors. Superconductivity is a macroscopic quantum phenomenon based on electron-phonon interaction. The electrons combine in couples to *Cooper pairs*. There are two properties related to superconductivity:

- $R = 0$: The electrical resistance of a superconductor is identical zero.
- $B = 0$: The magnetic flux density inside a superconductor is identical zero (in the *Meissner state*).

These materials are only superconductors when the temperature is below a critical temperature T_c and in a magnetic field below a critical magnetic field H_c. Furthermore, the current density has to be below the critical current density J_c, else the superconductivity breaks down. Usually superconductors are classified in two different ways; high-T_c/low-T_c and type I/type II. The first observation of superconductivity was by Gilles Holst and Kamerlingh Onnes in 1911. They discovered the zero resistance in mercury (Hg) below 4.2 K. Several years later, in 1933, the superconductors ability to expel flux was discovered. The first superconductors that were discovered had a critical temperature below 10 K. These superconductors are now called low-T_c superconductors. To obtain such low temperatures liquid helium, which has a boiling point at 4.2 K at 1 atm., is used for cooling. The other class of superconductors is called high-T_c superconductors. These can be cooled below its critical temperature by liquid nitrogen, which boils at 77 K. In 1987 Paul C. W. Chu and Maw-Kuen Wu found that $YBa_2Cu_3O_3$ was superconducting below $T_c = 93$ K. This was the first time a material that can be cooled below its critical temperature by liquid nitrogen was observed. The discovery of high-T_c superconductors was very important because liquid nitrogen is much cheaper and easier to work with than liquid helium [1, 14].

The other way to classify superconductors regards to the way they respond to a magnetic field. When a type I superconductor is exposed to a field $H > H_c$, it immediately stops being superconductive i.e. $R \neq 0$ and $B \neq 0$ inside the superconductor. A type II superconductor has two critical fields H_{c1} and H_{c2}. In Fig. 1 the H-T phase diagram for a type II superconductor is shown. When the type II superconductor is exposed to a magnetic field below H_{c1} it is in the *Meissner state* with $R = 0$ and $B = 0$ (as a type I superconductor). The ability to expel flux is called the *Meissner effect*. H_{c1}(T) is the minimum applied field for which a single vortex is thermodynamically favored to be in the material. A vortex is a quantized flux line carrying a single flux quantum $\Phi_o = h/2e$, where h is Planck's constant and $2e$ is the charge of a Cooper pair. Each vortex has a supercurrent circulating around it. For increasing field in the range $H_{c1} < H < H_{c2}$ more and more vortices will penetrate the superconductor. This state is called the *vortex or mixed state*. The resistance is still identical zero but $B \neq 0$ inside the superconductor. When $H \geq H_{c2}$ the superconducting state with vortices is no

longer thermodynamically favored (the normal cores in the vortices overlap). The superconductor enter the normal state with a non-zero resistance.

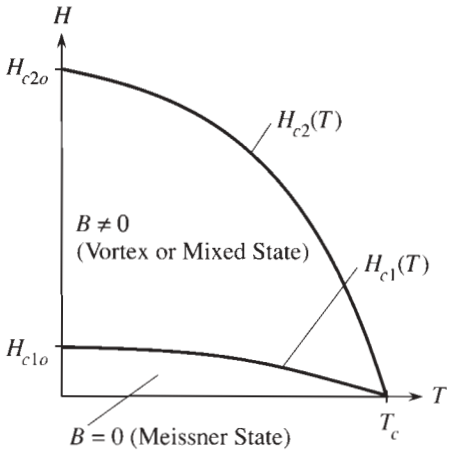

Figure 1. H-T phase diagram for a type II superconductor [1].

Type I and II superconductors can also be distinguished by comparing λ and ξ, where λ is the magnetic penetration depth and ξ is the coherence length (radius of the vortex). In the Ginzburg-Landau theory the *Ginzburg-Landau kappa* is defined as: $\kappa \equiv \lambda/\xi$. A type I superconductor has $\kappa < 1/\sqrt{2}$ and a type II has $\kappa > 1/\sqrt{2}$ [1].

High-T_c superconductors have very short coherence lengths ξ and are therefore type II superconductors. These type II superconductors are most often used for applications since they, besides have higher T_c values, remain superconductors in much higher magnetic fields than a type I superconductor.

That the penetration of vortices in the superconductor do not cause a DC resistance is only true if the vortices do not move. Otherwise a flux flow resistance appears. Fortunately in most applications the vortices are pinned on imperfections and interfaces to non-superconducting materials and the DC resistance will remain zero until the critical current density J_c is exceeded. When the current density is higher than J_c the pinning force is no longer strong enough and the vortices start moving. This movement causes a resistance [1]. The critical current density J_c is defined as the current density for which the voltage is 1 μV/cm.

2.2 Crystal structure of Bi-2223

$(Bi,Pb)_2Sr_2Ca_{n-1}Cu_nO_x$ (n = 1–3) is a ceramic type II superconductor. Bi-2201 ($n = 1$) has $T_c \approx 20$ K, Bi-2212 ($n = 2$) has $T_c \approx 85$ K and Bi-2223 ($n = 3$) has $T_c \approx 110$ K. The T_c value has a maximum for $n = 3$. For higher n-values T_c is decreasing [15].

The average crystal structure of $(Bi,Pb)_2Sr_2Ca_{n-1}Cu_nO_x$ has pseudo-tetragonal[3] symmetry. A half unit-cell consists of the following layer sequence along the c-axis: BiO-SrO-CuO_2-$(n-1)\times$(Ca-CuO_2)-SrO-BiO. One unit-cell consists of two of these sequences where the upper half unit-cell is shifted by $a/2$ with respect to the lower one. In other words, the structure consists of a double BiO layer with the perovskite type elements SrO, CuO_2 and Ca in between. An increase of one in the n-value implies one more layer of Ca and CuO_2 in the half unit-cell.

[3]Tetragonal geometry: $a = b \neq c$, $\alpha = \beta = \gamma = 90°$.

The superconductivity is associated with the CuO_2 planes. The unit-cell of the average crystal structure of Bi-2223 ($n = 3$) is shown[4] in Fig. 2. It has the lattice parameters $c \approx 37$ Å and $a \approx b \approx 5.4$ Å [16]. The critical current density parallel to the ab-planes is much higher than the critical current density along the c-axis ($J_c^{ab} \gg J_c^c$) [17].

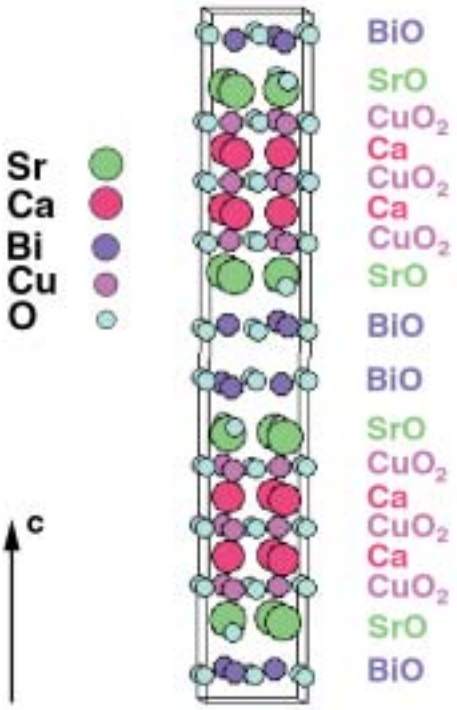

Figure 2. Unit-cell of the average structure of Bi-2223.

Another way to present the unit-cell is by a well focused high-resolution TEM image (cf. section 3.5) as in Fig. 3. The height of the inserted square corresponds to that of the unit-cell in the c-axis direction. The double BiO layers are the most prominent layers.

The crystallographic orientations can be determined by electron diffraction patterns from a single Bi-2223 grain. Fig. 4 shows three diffraction patterns of Bi-2223. The zone axes (the direction parallel to the incoming beam) are [110], [010] and [100], respectively. In all three diffraction patterns the c-axis direction is along the vertical lines of spots (smallest distance between the spots due to the reciprocal space) and the zone axes are perpendicular to the paper.

In the third diffraction pattern in Fig. 4 additional spots appear. These satellite reflections are due to modulation along the b-axis. The number of spots tells the perfection of the modulation. If only the first order satellite is visible (one spot to each site of the spots from the basic structure) the modulation is sinusoidal. An infinite number of spots is due to a step function modulation (superposition of sinusoidals). Defects imply a finite number of spots. The presented modulation has the period of $\sim 8b$ and the satellite spots are opposite the spots from the basic structure. The modulation is a Pb-type modulation. Another modulation is the Bi-type modulation. It has the period of $\sim 5b$. In this case the first order satellite spots is lying opposite the gab between the spots from the basic structure. With

[4]The unit-cell is drawn by using the input parameters from Ref. [11].

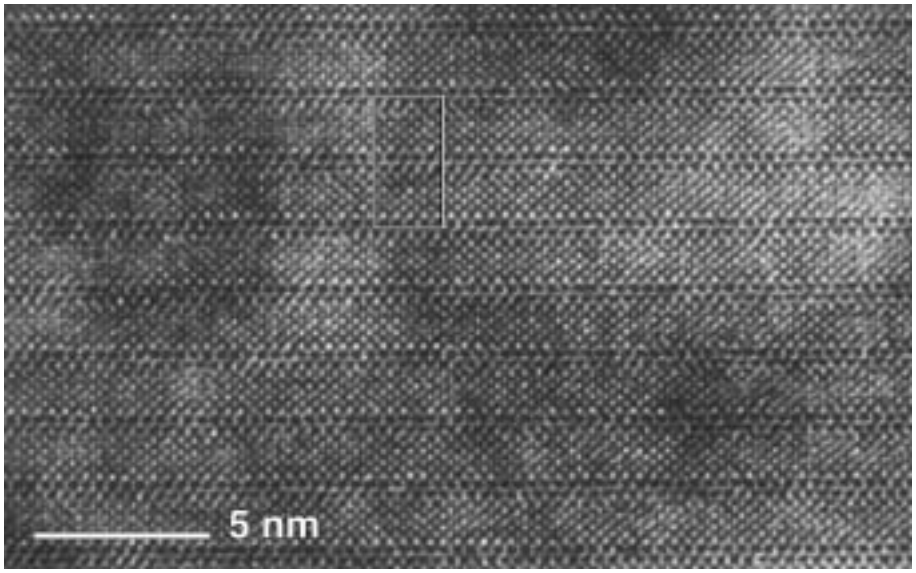

Figure 3. High-resolution TEM image of Bi-2223. The height of the inserted square is the unit-cell height in the c-axis direction.

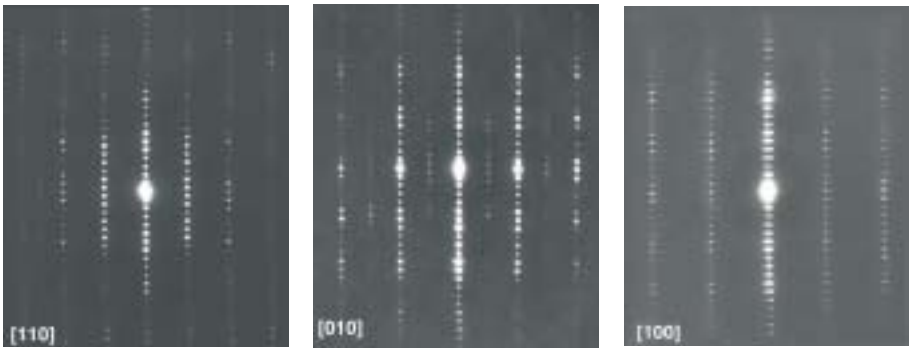

Figure 4. Diffraction patterns of Bi-2223. The zone axes are [110], [010] and [100], respectively.

an increasing Pb content in the precursor powder for the production of Bi-2223 superconducting tapes the modulated structure is changing from a Bi-type, via a mixed Bi/Pb-type, to a Pb-type modulation [18, 19, 20]. Zandbergen *et al.* [19, 20] have postulated models for the modulation. The model based on incorporation of extra oxygen in the (Bi,Pb)O layers obtains best agreement with the experimental results. The extra oxygen leads to a varied Bi-Bi distance alternating along the *b*-axis. In TEM images taken with the beam direction parallel to the *a*-axis direction the modulation is seen as a wavy contrast. An example of the Pb-type modulation is shown in Fig. 5.

By high-resolution TEM microscopy investigations another crystal structure phenomenon can be observed. The Bi-2223 grains consist not of pure Bi-2223 ($n = 3$) unit-cells, but intergrowth of half unit-cells of other periodicities e.g. Bi-2212 ($n = 2$) and Bi-2234 ($n = 4$) can be observed. This phenomenon is investigated in section 4.8.

Due to the layered crystal structure the Bi-2223 grains are elongated along *a* and *b*. The superconducting Bi-2223 grains grow in so-called colonies. A colony is a stack of grains with a common *c*-axis, but twisted within the *ab*-plane [13]. The [001] twist boundaries are between the BiO double layers. In Fig. 6 a schematic drawing of a colony is shown.

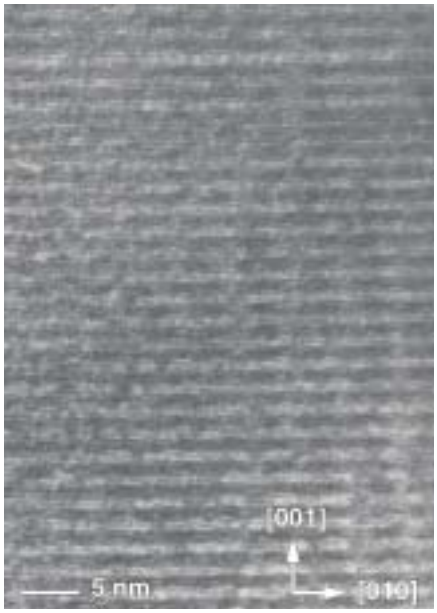

Figure 5. Modulation along the b-axis is seen as a wavy contrast in a TEM image.

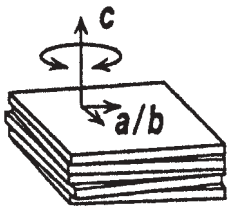

Figure 6. Schematic drawing of a colony [13]. It consists of a stack of Bi-2223 grains with a common c-axis, but twisted within the ab-plane.

Colonies can be connected to each other by two types of *c*-tilt grain boundaries [13]: small-angle *c*-axis tilt (SCTILT) boundaries (Fig. 7(a)) and edge-on *c*-axis tilt (ECTILT) boundaries (Fig. 7(b)). In TEM bright field images the *ab*-twist is seen as different gray levels. An example of a SCTILT boundary and a ECTILT boundary are shown is Fig. 8 and Fig. 9, respectively.

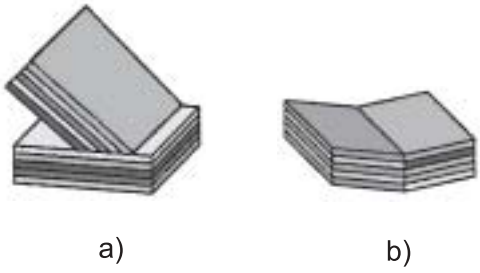

Figure 7. Grain boundaries: (a) small-angle c-axis tilt (SCTILT) boundary, (b) edge-on c-axis tilt (ECTILT) boundary. The different gray levels symbolize the twist between the grains.

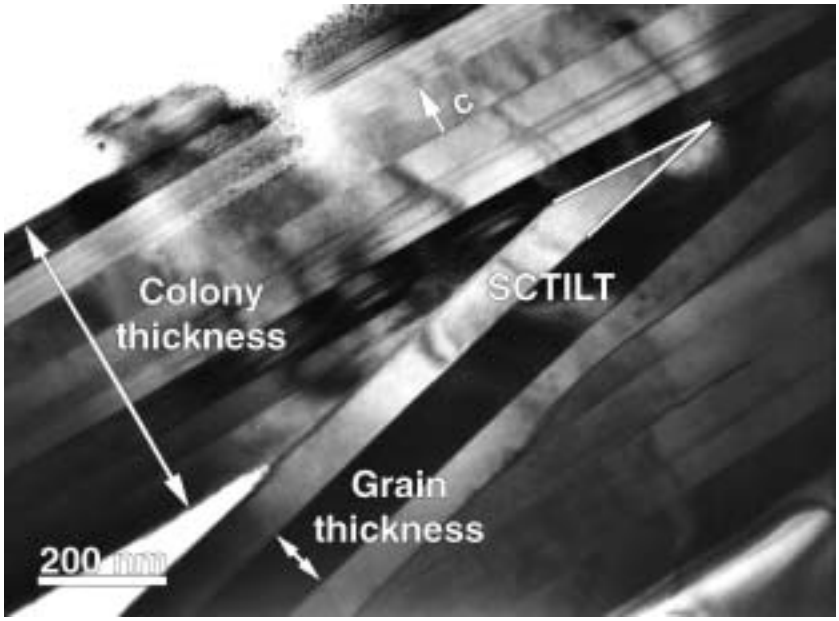

Figure 8. TEM bright field image showing two colonies forming a small-angle c-axis tilt (SCTILT) boundary. The different gray levels correspond to grains separated by ab-plane twist boundaries.

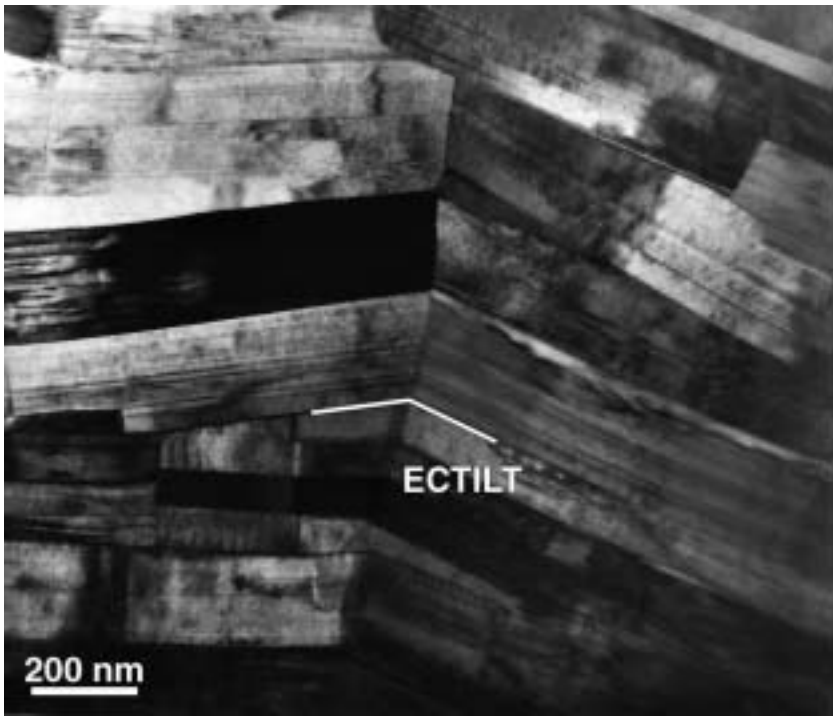

Figure 9. TEM bright field image showing edge-on c-axis tilt (ECTILT) boundaries.

3 Experimental

This chapter contains information of the processing of the Bi-2223/Ag tapes, the sample data and the setup of the synchrotron radiation measurements including a description of the data analysis. In addition, basic information of scanning electron microscopy (SEM) and transmission electron microscopy (TEM) is given.

3.1 Tape processing

Polycrystalline $(Bi,Pb)_2Sr_2Ca_2Cu_3O_x$ (Bi-2223) tapes are produced by the powder-in-tube (PIT) technique, where a randomly orientated powder of $(Bi,Pb)_2Sr_2CaCu_2O_x$ (Bi-2212) and secondary non-superconducting phases are filled into a silver tube. The tube with powder is first drawn then rolled to a so-called mono-filamentary green tape with the thickness of ∼0.2 mm [21]. If this process is repeated by putting a number (typically 19, 37, 55 or 85 filaments) of these mono-filamentary green tapes into a new silver tube a multi-filamentary green tape with the thickness of ∼0.2 mm is produced. A multi-filamentary tape yields a more robust and flexible current lead and has a higher critical current density. The powder in the tape is converted into Bi-2223 by a series of annealing steps with intermediate rolling and/or pressing steps. The annealing temperature is usually around 830 °C depending on the composition of the green tape and the surrounding atmosphere. During processing the *c*-axis of the Bi-2223 grains aligns to some extent to the tape normal (the grains are elongated along *a* and *b*). In Fig. 10 is shown an image of a part of a transversal cross-section of a 37-filamentary tape.

Figure 10. An backscattered SEM image (cf. section 3.4) of a part of a transversal cross-section of a 37-filamentary tape. The dark gray is the ceramic filaments and the light gray is the silver matrix. The dimensions of the tape segment are 0.2×2.0 mm^2. The direction of the nominal supercurrent will be perpendicular to the paper.

The Bi-Sr-Ca-Cu-O compound is doped with Pb. The substitution of Bi by Pb supports the crystallization of the Bi-2223 phase [22, 23]. Furthermore, it lowers the temperature of the stability range of the Bi-2223 phase [24].

The tapes were beforehand annealed in an environment of technical air. Today usually the surroundings are ∼ 8% O_2 and 92% N_2. During the tape processing an oxygen exchange through the silver takes place. The reduced oxygen in the surroundings result in a lowering of the melting point of Bi-2212, a lowering and a broadening of the temperature range within Bi-2223 is formed [25], a higher solubility of Pb in Bi-2212 [26], and a faster reaction rate (cf. section 4.2.1).

Today the strength of the tapes is increased by using silver alloys instead of pure silver. The company American Superconductor has produced high strength tapes with steel around the silver.

To obtain tapes with a higher value of the critical current density it is important to get a better alignment of the Bi-2223 grains, better connectivity between the grains, higher conversion into Bi-2223 (less secondary phases such as $(Ca,Sr)_2CuO_3$, $(Ca,Sr)_2PbO_4$, CuO, Bi-2201 and 3221[5]) and a better flux pinning.

[5] 3221 is short for $Pb_{3-x}Bi_xSr_2Ca_2CuO_y$.

The tape processing can be optimized by optimizing the powder composition, the powder-in-tube technique (e.g. use squared tubes instead of round tubes), the intermediate pressing/rolling, the annealing temperature, the heating and cooling rate, the duration of the annealing steps and the oxygen content in the surroundings.

3.2 Samples

Nordic Superconductor Technologies (NST) has supplied two long length tapes. Both have a length of 100 m. They are 37-filamentary tapes in a pure silver matrix. The composition of the used powder is $Bi_{1.8}Pb_{0.33}Sr_{1.87}Ca_2Cu_3O_x$. It has been calcined at 830 °C. The one is a green tape and the other is a processed tape, where only the last annealing has not been performed. For obtaining comparable results, these tapes are used in all investigations, except in the *in situ* synchrotron radiation experiments where a mono-filamentary tape is used. The width of the multi-filamentary tapes is 3.0 mm and the thickness is 0.2 mm. The area ratio between the silver and the superconducting core is Ag/SC = 3. It gives a cross-section area of the superconducting core of 0.15 mm^2. The quality of the tape can be expressed by the critical current I_c, the critical current density J_c or the engineering critical current density J_e, which is the critical current divided by the area of the total cross-section of the tape (and not only the superconducting core). Throughout this thesis the critical current values I_c are presented. This is partly because the samples are produced from the same green tape and thereby have the same size and Ag/SC ratio, and partly because it is the critical current I_c that is measured. With the given area of the superconducting core e.g. $I_c = 40$ A corresponds to $J_c = 27$ kA/cm^2.

The mono-filamentary green tape used for the *in situ* synchrotron radiation experiments in 8% O_2 is also embedded in a pure silver matrix. The composition of the powder and the calcination temperature used are identical to those used for the multi-filamentary green tape. The width of the tape is 2.8 mm and the thickness is 0.17 mm. When analyzing the *in situ* synchrotron radiation experiments the mono-filamentary tape was chosen because the multi-filamentary tape results in a lower signal-to-noise ratio.

The tape is cut in pieces of 4.5 cm [6]. After heat treatment of these pieces of tapes the critical current are measured at 77 K in self-field by the standard 4-point method with the criterion of 1 μV/cm.

Identification of samples used in TEM investigations and texture investigations by the synchrotron X-ray technique is shown in Table 1. Using the synchrotron radiation these five multi-filamentary tapes have been found to be fully converted (except local intergrowth) from Bi-2212 into Bi-2223. The critical currents I_c are obtained by averaging results for three tapes.

ID	Annealing in 8% O_2	I_c (A)
Sample 1	75 h (total), multi steps, intermediate pressing (fully processed)	44
Sample 2	<50 h, 1 step (1st annealing)	9
Sample 3	200 h, 1 step	20
Sample 4	Almost fully processed tape stopped at 650 °C for 3 weeks	22
Sample 5	Almost fully processed tape quenched during last annealing	26

Table 1. Sample identification.

[6] A tape length of 4.5 cm is sufficient for obtaining a representative I_c value and structure. However, structural changes occurred within the outmost 2 mm [8].

3.3 Synchrotron

A synchrotron is a circular particle accelerator which accelerates charged particles such as electrons/positrons or protons to relativistic velocities by magnetic fields. The particles are preaccelerated in a linear accelerator (Linac). The synchrotron is used for support of particles to storage rings where the particles traveling with nearly the speed of light. The storage ring facility is used for high energy particle physics (e.g. electron-proton collision experiments) or as sources for synchrotron radiation. The emitted synchrotron radiation is produced in bending magnets of accelerators or in special magnetic devices (wigglers and undulators) in the storage ring. The principle of the wigglers and undulators is to oscillate the electrons/positrons perpendicular to their direction of motion by magnetic fields of alternate signs. Radiation is then emitted by each wiggle [27].

The experimental synchrotron radiation work is performed at the BW5 beamline [28] at HASYLAB at DESY (Deutsches Elektronen-Synchrotron) in Hamburg. BW5 is a beamline with synchrotron radiation generated from wigglers in the storage ring called *Doris*. The circumference of Doris is 289 m and the maximum beam energy is 4.5 GeV. The particle type is positrons [29].

One study of grain growth mechanism is performed at the beamline ID11 at ESRF (European Synchrotron Radiation Facility) in Grenoble with the 3DXRD microscope setup (cf. section 3.3.4). The circumference of the storage ring at ESRF is 844 m and the operating energy is 6 GeV [30].

3.3.1 Experimental setup

The energy of the synchrotron radiation used for the X-ray diffraction studies in Hamburg is ∼100 keV. At this high energy the penetration depth is 650 μm for the silver and 600 μm for the Bi-2223. The high penetration depth enable an overall bulk study of the structural properties of Bi-2223/Ag tapes within the silver clad. This is an important property of high-energy X-ray due to the fact that the silver influences the phase relations significantly [31, 32, 33].

The white beam is defined by a pinhole of the size of 1×1 mm^2 or 2×2 mm^2 before it is monochromatized by an imperfect $SrTiO_3$ (200) crystal with a mosaicity of FWHM = 40" or a Si/Ge (111) gradient crystal. The monochromatic beam with an energy of ∼100 keV is then sent through a slit for defining it (Fig. 11). The gap of the slit is typically 1×1 mm^2. The incoming flux on the sample will be ∼10^{11} photons/s. The tapes are mounted on a horizontal ω rotation table. The rolling direction (RD) of the tape is placed vertically and the normal direction (ND) is parallel to the beam at $\omega = 0°$. By choosing the angle between the incoming beam and the normal direction of the tape to 75° we can observe many of the Bi-2212 and Bi-2223 reflections including the (115) and (00l) lines. For $\omega = 75°$ the effective thickness of a 200 μm thick tape is 770 μm. The transmitted diffracted beam is recorded online on a 2D detector. The detector has been a CCD camera or an image plate. The exposure times are typically 1–5 minutes. The beam illuminates a sample area of approximately the width of the tape. The distance between the sample and detector is chosen so the detector covers the 2θ range up to ∼4°. (This corresponds to ∼52° when using Cu K_α radiation). Due to symmetry normally only a quarter of the diffraction image is recorded by the CCD camera. Further details on the experimental setup are given in [34].

For *in situ* annealing experiments the tapes are placed in an aluminum furnace within a quarts tube or an Al_2O_3 tube. The environment within the tube is technical air or a flow of 8% O_2 and 92% N_2. For controlling the flow a tube is connecting the outlet to a bottle with water. Several tapes can be placed with $\omega = 75°$ in the sample holder. They can alternately be translated to the beam

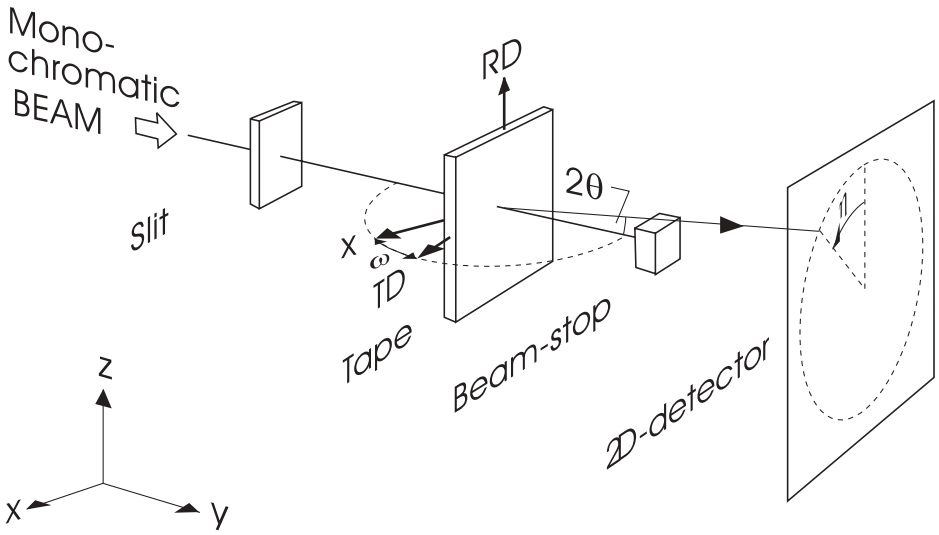

Figure 11. Schematic drawing of the experimental setup at the BW5 synchrotron beamline at HASYLAB. RD and TD refer to the rolling and transverse direction of the tape, respectively. The rotation angle ω, the Bragg angle θ and the azimuthal angle η around the Debye-Scherrer cones are illustrated.

by a xz translation table. Two thermocouples are placed near the tapes to ensure a correct temperature. Around the tube (to the right, below and left of the beam) a heater of Kanthal is placed. Between the tube and the furnace wall two silver radiation shields are inserted. In the environment outside the tube vacuum ($\sim 10^{-4}$ mbar) is established for minimizing the heat transport. The furnace has a double aluminum wall – except at the beam hitting area – where cooling water is flowing. In total the incoming beam has to penetrate a 1 mm Al window in the furnace wall, two 100 μm Ag heat shields, a 2.1 mm quartz tube (or a 2 mm Al_2O_3 tube) before it hits the tape. The diffracted beam has as well to penetrate the same in the opposite order. In Fig. 12 is shown the experimental hutch with the setup used for *in situ* annealing experiments.

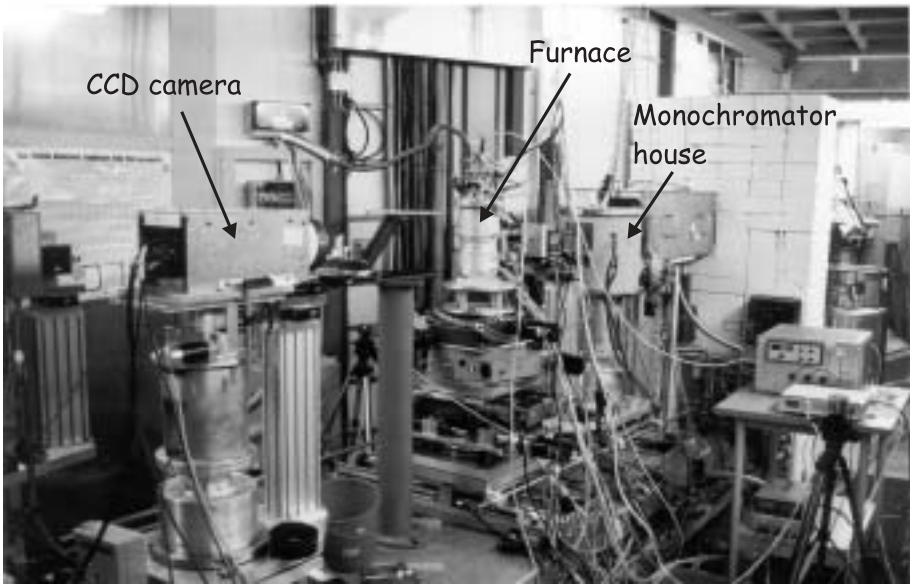

Figure 12. The experimental hutch at the BW5 beamline at HASYLAB with the setup used for in situ annealing experiments.

A heating experiment has been done in order to determine the thermal expansion of the sample holder within the furnace. The result is that the expansion is 0.19 ± 0.005 mm/100 °C. During an *in situ* annealing run the vertically position is adjusted with this value.

The current in the storage ring is varied over a period of approximately 12 hours from ∼140 mA just after an injection of positrons to ∼80 mA just before an injection. Either this current is read out for normalization of the data or a diode is placed in front of the sample for counting the flux. By using the Si/Ge (111) gradient monochromator it is necessary to use the diode as this monochromator is nonlinear.

3.3.2 Data analysis

An example of a raw diffraction image recorded by the CCD camera is shown in Fig. 13 (another example can be seen in Paper 1). Such single exposure gives in-

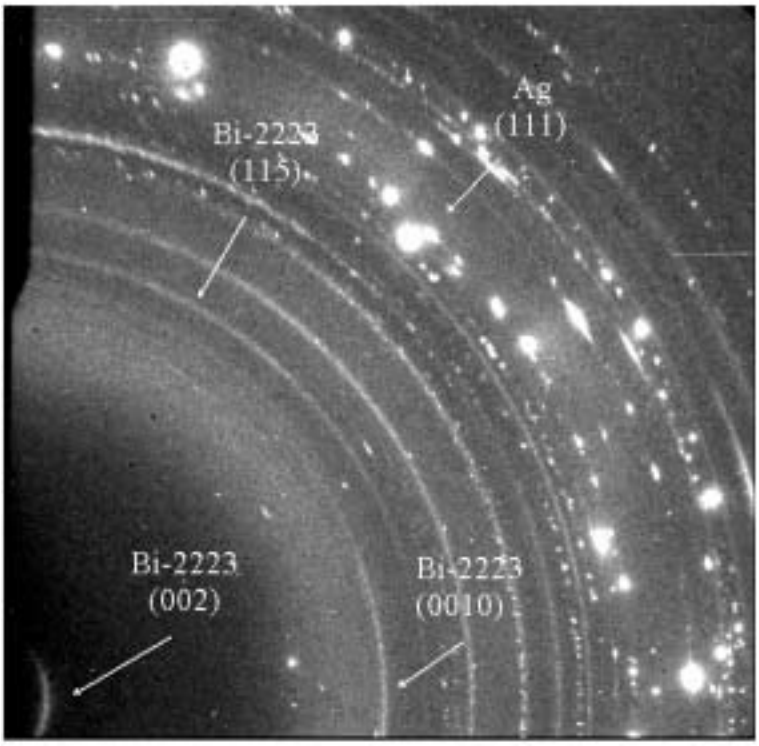

Figure 13. A raw image from the experiment described in Paper 2. The temperature of the sample is 860 °C and it has been annealed for 2440 min. Due to symmetry this quarter of the full diffraction pattern is adequate for the analysis. Note that this is not a typical image. The high temperature results in a high background level.

formation on the concentration and the texture of the dominant crystalline phases such as Bi-2223, Bi-2212, Bi-2201, $(Ca,Sr)_2PbO_4$ and $(Ca,Sr)_2CuO_3$. The different reflections are identified by *Bragg's Law*:

$$\lambda = 2d \sin\theta \tag{1}$$

For fixed wavelength λ of the X-rays (photons) it gives the relation between the *Bragg angle* θ and the d spacings (the spacing of the atomic planes).

Before analyzing the data the images have to be normalized. The normalization formulae is:

$$I_{norm} = \Big(I_{meas} - (\text{Read-out-noise} + \text{Dark current} \cdot t)\Big) \cdot \frac{c}{Doris \cdot t} \tag{2}$$

Here I_{meas} is the measured intensity,"Read-out-noise" is the read-out-noise of the CCD camera (the recorded intensity during a very short time period (1 s) without beam), "Dark current" is the recorded intensity (subtracted the read-out-noise) per minute without beam during a longer time period. "Read-out-noise + Dark current $\cdot$ t", which is zero for the image plate, can be replaced by a recorded intensity without beam during a time period equal to the exposure time. *Doris* is the current in the storage ring (called Doris) or the flux counted by the diode, t is the exposure time in minutes and c is a normalization constant.

The normalized two-dimensional images are analyzed by means of the program package FIT2D [35]. Input parameters for the program are the pixel size, the sample to detector distance and the wavelength λ of the photons. $\lambda = hc/E$, where h is Planck's constant, c is the velocity of light and E is the photon energy. $E \approx 100$ keV gives a wavelength of $\lambda \approx 0.12$ Å. We analyze the data by means of two one-dimensional projections of the image. By integrating the images along the azimuthal angle η in the Debye-Scherrer cones we obtain so-called 2θ projections as shown in Fig. 14 (one segmented ring in Fig. 13 corresponds to one peak in Fig. 14).

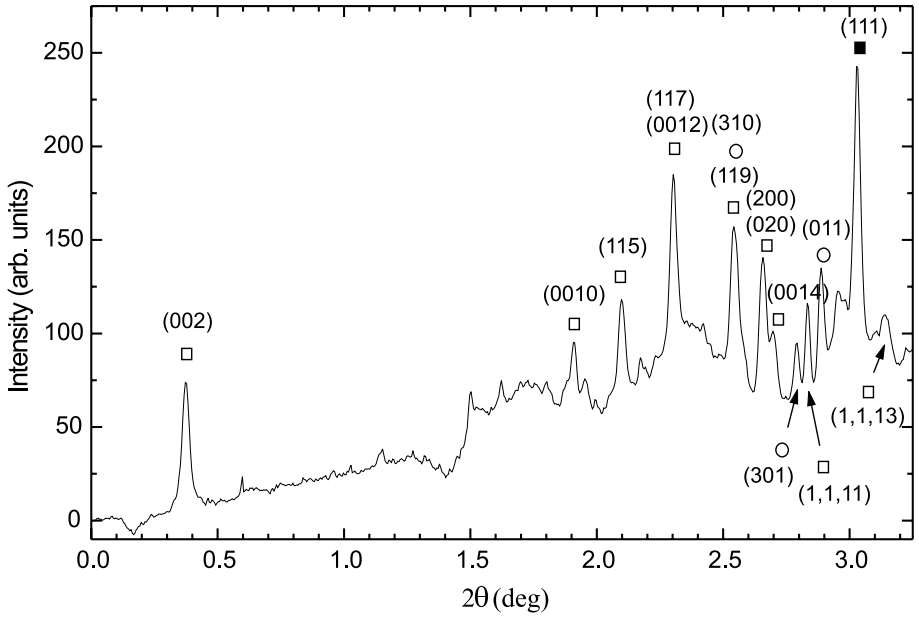

Figure 14. A 2θ projection of the data based on an analysis of the image shown in Fig. 13. The symbols refer to: (□) Bi-2223, (○) $(Ca,Sr)_2CuO_3$ and (■) Ag. Note that the background level at $2\theta > 1.5°$ origins in scattering from a partial liquid due to an unusual high temperature.

A peak in the 2θ projections is fitted to a squared Lorentz distribution (also referred to as a Breit-Weigner distribution) and a sloping linear background. The amplitude times the full width at half maximum (FWHM) is a measurement of the integrated intensity. The integrated intensities of the peaks are used to estimate the relative concentrations (the maximum of the integrated intensity of Bi-2212 is set to 100% and the concentrations of other phases are evaluated based on their structure factors). Likewise, the accurate 2θ position of the midpoint and the FWHM of the peaks provide information on the stoichiometry and grain sizes/internal strain, respectively. From the "background" information on the development of a presence liquid can be obtained (cf. Paper 2 and Fig. 14).

The selected peaks for Bi-2212 and Bi-2223 are usually the non-overlapping (115) reflections. From the data in [34] (based on the concentration relation: $C_{2201}+C_{2212}+C_{2223}=100\%$) the corrections of the intensities compared to Bi-2212 (115) due to different structure factors are calculated (Table 2).

I_{2201} (115)	$= 1.00 \times I_{2201}$ (115) (measured)
I_{2223} (115)	$= 1.43 \times I_{2223}$ (115) (measured)
I_{CPO} (110)	$= 2.46 \times I_{CPO}$ (110) (measured)

Table 2. Corrections of the synchrotron intensities used for estimation of relative concentrations compared to Bi-2212 (115). CPO is short for $(Ca,Sr)_2PbO_4$.

For the *in situ* experiment "1st annealing in 8% O_2" the (00l) reflections are used for analysis of the phase development due to the (115) reflection of Bi-2223 unfortunately has disappeared behind the Al_2O_3 rings from the tube in the furnace (and Bi-2223 (117) is overlapping in the 2θ projection with Bi-2223 (0 0 12) and Bi-2212 (0 0 10)). The "structure factor" of Bi-2223 is found by equalizing the slope of the integrated intensities versus the annealing time of Bi-2212 and Bi-2223 (preservation of Bi-2212 + Bi-2223) in the range 600-900 min (cf. Fig. 28). The correction of the Bi-2223 (0 0 10) intensities compared to Bi-2212 (008) is written in Table 3. By converting the integrated intensities to concentrations the maximum of the integrated intensity of Bi-2212 (008) is set to 100%.

I_{2223} (0 0 10)	$= 0.83 \times I_{2223}$ (0 0 10) (measured)

Table 3. Correction of the Bi-2223 (0 0 10) intensities used for estimation of relative concentrations compared to Bi-2212 (008).

The other projection of the two-dimensional normalized images is a so-called texture profile, where the radially integrated intensities within a 2θ range around a selected reflection are plotted as function of the azimuthal angle η. The smaller the full width at half maximum FWHM of this texture profile the better the alignment of the superconducting crystals in the tape. From the η-texture profile a background is subtracted.

The texture profile as function of η has to be transformed to a function of the polar coordinate α (Fig. 15) before finding the FWHM of the (squared Lorentz[7]) profile as a measurement of the texture or grain mis-alignment. This measurement of the texture is only correct if the texture of Bi-2212 and Bi-2223 is fiber-symmetric with (00l) aligned along ND. In section 3.3.3 the texture to a good approximation is shown to be fiber-symmetric with (00l) aligned along ND. The transformation from $\eta \rightarrow \alpha$ is given by [34]:

$$\cos(\alpha) = |\cos(\theta)\sin(\eta)\sin(\omega) + \sin(\theta)\cos(\omega)| \tag{3}$$

The (115) or (117) reflection is selected for the texture analysis. (00l) is not a good choice because the central part of the distribution is not accessible due to absorption (cf. section 3.3.3).

[7]The squared Lorentz distribution is found to be the best fit of the profile.

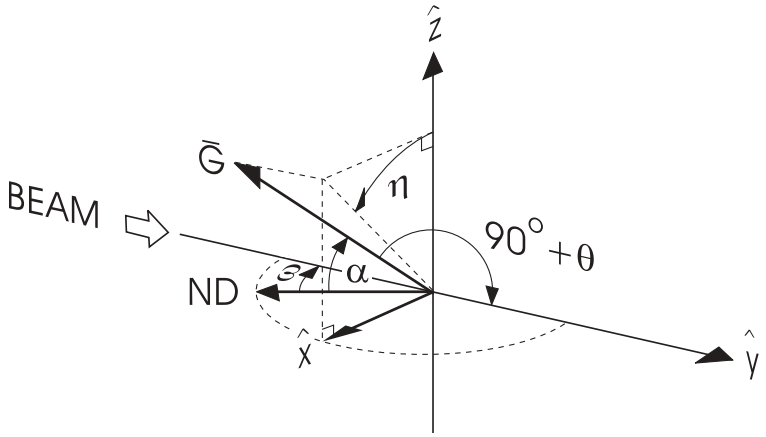

Figure 15. Illustration of the definition of the angle α used for texture analysis of Bi-2212 and Bi-2223. $\overline{G}$ is the scattering vector and ND is the normal direction of the tape [34].

3.3.3 Pole figure

During the texture analysis of the synchrotron data an assumption of fiber texture was used. The textures called fiber textures exhibit rotational symmetry, e.g. produced by an axially symmetric deformation. The crystallographic direction is most commonly parallel or nearly parallel to the deformation axis. Wires produced by e.g. drawing and rolling usually develop preferred orientations that can be described by fiber textures [36]. In this section it will be verified that the fiber symmetric approximation is valid.

Pole figures are a simple way of describing the texture of materials. A pole figure is a stereographic projection. An illustration of construction of a pole figure for a single crystal (grain) is shown in Fig. 16. A general treatment of the use of hard X-rays for texture characterization is given in Ref. [37].

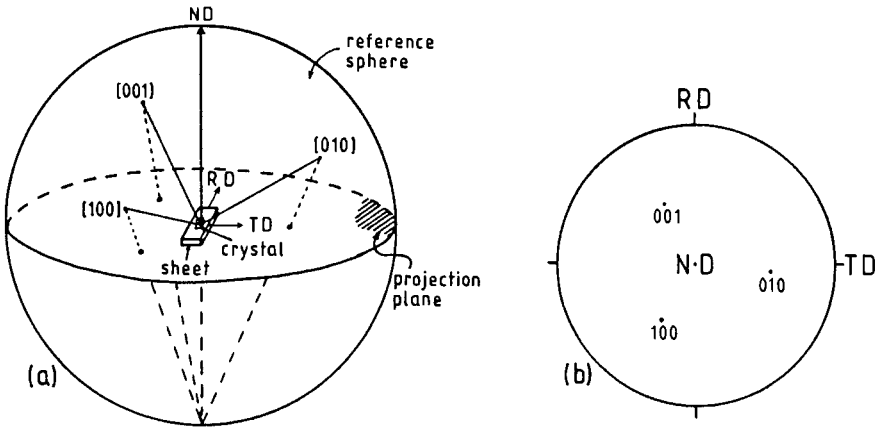

Figure 16. (a) An illustration of construction of a pole figure (b) The corresponding pole figure [36].

For producing a pole figure of the Bi-2223/Ag tapes a fully processed tape was illuminated at the beamline BW5 at HASYLAB in Hamburg using 97.4 keV X-rays. The Si/Ge (111) gradient monochromator was placed so that the energy spread was minimized. The diffraction pattern images were recorded in the whole η range (0°–360°) in the range of the rotation angle ω of 0° to 85° in 5° steps,

where the incoming beam is parallel to the tape normal (ND) for $\omega = 0°$. The exposure time for each rotation angle was 100 s. The size of the pinhole before the monochromator was $1{\times}1$ mm^2.

For each rotation angle ω a texture profile (intensity I versus the azimuthal angle η) is produced of the Bi-2223 (115) reflection from the diffraction pattern image (cf. section 3.3.2). A background subtraction is performed before further analysis.

The trace of the η-scan is transformed in the pole figure to two curves for each ω values (one for each hemisphere). In Fig. 17 is shown the tracks in the TD-RD plane for different ω values.

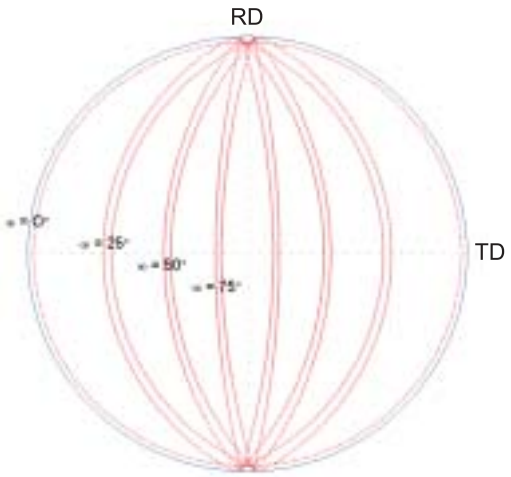

Figure 17. Construction of the pole figure: The pairs of lines for different ω values show the position of the intensities along the Debye-Scherrer ring (η) after transforming to the RD-TD plane. Only the tracks of $\omega = 0°$, $25°$, $50°$ and $75°$ are shown.

When ω is changing the absorption and the volume of the illuminated part of the tape are changing. Therefore, the intensity has to be normalized to these two quantities. The corrected intensity I_{cor} is:

$$I_{cor}(\omega, \eta, \theta) = \frac{1}{V(\omega) \cdot A(\omega, \eta, \theta)} \cdot I(\eta) \tag{4}$$

where $V(\omega)$ is the illuminated volume and $A(\omega, \eta, \theta)$ is the absorption coefficient (transmitted part). The penetration depth μ for silver and Bi-2223 is nearly the same and the tape can therefore be approximated by a slab of thickness t. Due to small Bragg angles θ and narrow texture profiles ($\Delta\eta$ small) the absorption coefficient can be approximated by the $2\theta \to 0$ limit. In this limit the absorption coefficient $A(\omega, \eta, \theta)$ becomes (cf. [34]):

$$A(\omega) = e^{-\frac{t}{\mu \cos \omega}} \tag{5}$$

where t is the tape thickness and μ is the penetration depth. The illuminated volume is:

$$V(\omega) = \frac{t}{\cos \omega} \cdot W(\omega) \tag{6}$$

where $W(\omega)$ is the illuminated width of the tape. The expression for the corrected intensity becomes:

$$I_{cor}(\omega, \eta) = \frac{\cos \omega}{t \cdot W(\omega)} e^{\frac{t}{\mu \cos \omega}} \cdot I(\eta) \tag{7}$$

where $t = 200$ μm, $\mu = 645$ μm and $W(\omega) = 3000$ μm $\cdot \cos\omega$ if this value is less than 1000 μm else $W(\omega) = 1000$ μm (beam width).

The texture profile results for the Bi-2223 (115) reflections are transformed into a pole figure in the TD-RD plane (Fig. 18). The pole figure shows a well-defined ring at ω angles below $\sim 60°$ with a spread of 10% (this uncertainty is due to the interpolation over 5°). For higher ω values the absorption correction is not good enough. As supplement to the pole figure a $\omega = 0°$ texture profile of the (200)/(020) reflection can be used. In Ref. [34] this plot shows an approximately horizontal line. We can thereby conclude that the Bi-2223 texture to a good approximation is fiber-symmetric with (00l) aligned along ND. This implies that it is enough to select one well considered ω value and one reflection for texture analysis. Due to the absorption a too high ω value cannot be selected (90° would be ideal). By choosing $\omega = 75°$ the cut of (115) or (117) will be nearly perpendicular. Furthermore, the tail of the distribution of the (00l) reflections will also be cut.

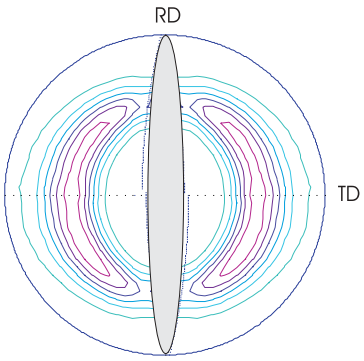

Figure 18. Pole figure of the (115) reflection of Bi-2223 showing fiber texture with (00l) aligned along ND. The hatched area corresponds to $|\omega| \geqslant 80°$. This area cannot be investigated because of too large absorption.

3.3.4 3DXRD

The setup at HASYLAB in Hamburg gives the opportunity to study the average stoichiometry changes and orientation of the Bi-2212 and Bi-2223 grains. However, with these data one cannot directly test models of the texture and transformation mechanisms, due to the fact that transformation rates etc. vary with grain size, grain stoichiometry and grain orientation. With the 3DXRD microscope [38, 39] we aim at following the kinetics of the individual embedded grains inside the Ag during annealing.

The difference between the 3DXRD microscope setup and the setup at HASYLAB is that the beam can be focused to a micron-size spot at the 3DXRD. The focused monochromatic beam is obtained by sending it through a bent Laue crystal for vertical focusing and a laterally graded multi-layer for horizontal focusing [40]. By using this unique setup of optics all the photons are available whereas slits would have cut off a lot of photons and thus the intensity would be too low.

In the experiment with a mono-filamentary green Bi-2223/Ag tape the beam had the energy of 80 keV. It was focused to a 5 μm horizontal line by the Laue crystal, and limited horizontally to 40 μm by a slit (the gab of the slit was 120 μm). The multi-layer was removed (unfortunately).

The tape was mounted as at HASYLAB in the aluminum furnace on a horizontal ω rotation table. The rolling direction (RD) of the tape was placed vertically. The

diffracted beam was monitored by a CCD camera while oscillating the tape by 0.5° (with 100 steps/s) around $\omega = 75°$. The exposure time was 5 min. Reflections from individual grains of Bi-2212 and Bi-2223 are clearly visible as dots on the detector. The grain volume is proportional to the integrated intensity of the dots and the grain stoichiometry is related to the 2θ angle. Due to identical a/b-axes the transformation of Bi-2212 into Bi-2223 will give rise to spots appearing with identical azimuthal angle in the images, if and only if the grain orientation is conserved. In this way essential information on the transformation mechanism should be available ("intercalation" vs. "growth on top" vs. "random nucleation"). To test whether the full integrated intensity was monitored validation tests were made continuously by increasing the rocking angle (with the period kept constant) or the beam width every second exposure. The intensity of the spot has to be constant when the beam width is increased and has to decrease by the same factor as the rocking angle velocity is increased to be valid. Due to an unfortunate setting most grains "rotated out" of the volume as function of time. The kinetics of a few constantly valid diffraction spots are being analyzed in section 4.6.

The prospect arising from this experiment leads beyond high-T_c superconductivity. With the 3DXRD microscope, it will in general be feasible to perform statistics on the volumes, strains, stoichiometry and orientation of the embedded grains in a powder, provided the grain volumes are $\sim$1 μm^3.

3.4 SEM/EDS

Scanning electron microscopy (SEM) with energy dispersive X-ray analysis (EDS) is useful to study the surface of a bulk specimen on the micrometer scale.

The principle in the scanning microscope is as follows: an electron gun generates electrons and accelerates them to energies between 2 keV and 40 keV. Condenser lenses demagnify the electron beam to a diameter of 2–10 nm at the point where it hits the specimen. Scan coils ensure that the electron beam is scanned across the specimen. In front of the specimen an aperture is inserted. When the incident beam hits the specimen elastic and inelastic scattering processes will take place until the electrons are stopped or escape from the specimen through the surface they entered. Radiation in form of backscattered electrons, secondary electrons and X-rays is generated. A detector picks up these signals.

Backscattered electrons (BE) are electrons from the primary beam that escape from the specimen. They leave the surface still having a large fraction of the incident energy. Secondary electrons (SE) are electrons that leave the surface with energies below $\sim$50 eV. A smaller fraction of these are primary electrons that leave the surface with an energy of only few eV (10–50 eV). But the majority of SE are electrons near the surface that have gained a small amount of energy from inelastic scattering such as phonon scattering and plasmon scattering of nearby primary electrons, which have just entered the specimen.

Electrons can be backscattered only if they are a fraction of a micron away from the surface. The diameter of the sampling volume in a material of medium atom number is $\sim$0.1 μm. Since secondary electrons most often are generated as primary electrons enter the specimen the diameter of the sampling volume is only a little larger than the incident beam. Therefore, this signal has the highest spatial resolution.

For topographic imaging usually SE are used. More SE are generated for tilted areas of the specimen since the yield (δ) varies with the tilt of the specimen (θ) as $\delta = \delta_o/\cos\theta$. The yield ($\eta$) of BE increases monotonically for increasing atomic number (Z). BE are therefore used for compositional imaging.

The X-ray signal is used to determine the composition of the phases identified

with different gray levels in the backscattered image. By spot analysis at a selected area an energy dispersive spectrum (EDS) with number of counts versus the X-ray energy can be produced. An efficient production of X-rays requires that the accelerated electrons have an energy of about two times the characteristic X-ray energy. Since the X-rays signal generated deep in the interaction volume (where the electrons penetrate) can escape from the specimen the sampling volume is almost as large as the interaction volume. The interaction volume is smallest for elements with high atomic numbers and for low electron beam energy. The smallest obtainable volume is $\sim$1 μm^3 [41].

The microscope used for the experimental SEM work is a JEOL JSM-840. The filament material of the electron gun is LaB_6. Accelerating voltage of 10 kV is used for SE and BE imaging and 20 kV for EDS. The lines of the elements used for the EDS analysis are Sr-L, Ca-K, Cu-K, Pb-L and Bi-L. The "live time" during an analysis is 100 s (with a "dead time" of 25–30%). The resulting atom % of the five elements are used to determine the phase composition. In addition, the number of counts are checked for observing whether the examined area could be a hole. Since η increases with Z the Ca/Cu-rich phases are seen as "dark", Bi-2223 as "gray" and Bi/Pb-rich phases as "white" in the BE image[8]. An example of a BE image is shown in Fig. 19.

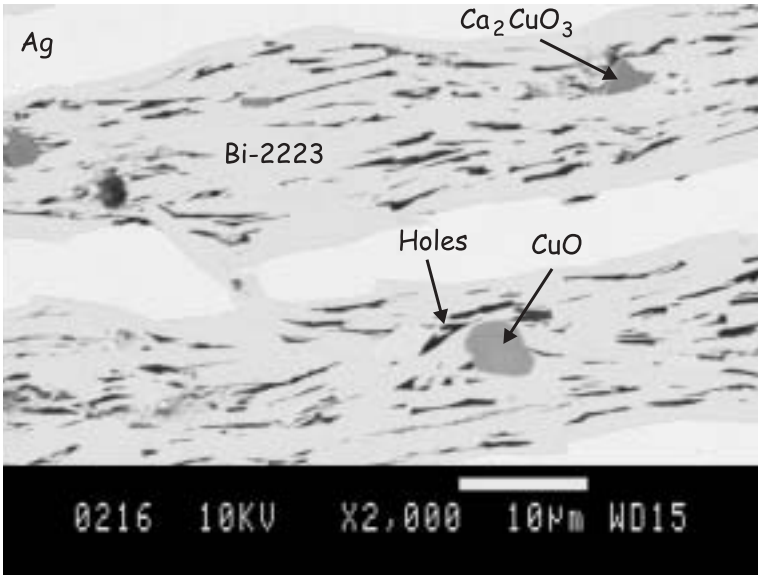

Figure 19. A backscattered image showing composition contrast. The phase composition is determined by spot analysis of the X-ray signal (EDS). In the image a transversal cross-section of two pieces of filaments can be seen.

Usually, a SEM specimen contains both a transversal and a longitudinal cross-section of 1–4 differently heat treated tapes. The pieces of tapes are embedded in epoxy and the well polished surface of the specimen is coated with a thin conducting layer of carbon for avoiding charging effect.

3.5 TEM

Transmission electron microscopy (TEM) gives the opportunity to study an electron transparent specimen (20–200 nm) of a material on micron scale down to an atomic scale. In addition, the transmission electron microscope can both produce

[8] Z = 20, 29, 38, 82 and 83 for Ca, Cu, Sr, Pb and Bi, respectively.

a magnified image and a diffraction pattern. EDS analysis with a higher resolution than at the SEM is also possible.

From the top of the transmission electron microscope a thermionic emission gun accelerates the electrons to energies of typically 100–400 keV. Below the electron gun a set of condenser lenses for demagnifying the beam are placed. These lenses also control the diameter (spot size) and the incoming angle (convergence angle) as the beam hits the electron transparent specimen. In Fig. 20 is shown the diagram for the further ray propagation of the two different operation modes. The objective lens which is focused on the specimen forms an intermediate image. An objective aperture ensures that all electrons which have been scattered with a higher angle than a certain angle get stopped. In the imaging mode (Fig. 20(b)) the intermediate lens magnifies this image further and passes it to the projector lens for display on a viewing screen. In the diffraction mode (Fig. 20(a)) the intermediate lens is refocused at the back focal plane of the objective lens. Finally, the diffraction pattern is passed to the projector lens for display on the screen. The intermediate lens (also called diffraction or first projector lens) is switched when changing operation mode. A selected area diffraction (SAD) aperture is used to focus on a smaller part of the specimen. The SAD aperture is located in the image plane of the objective lens (intermediate image 1) i.e. it creates a virtual aperture at the plane of the specimen.

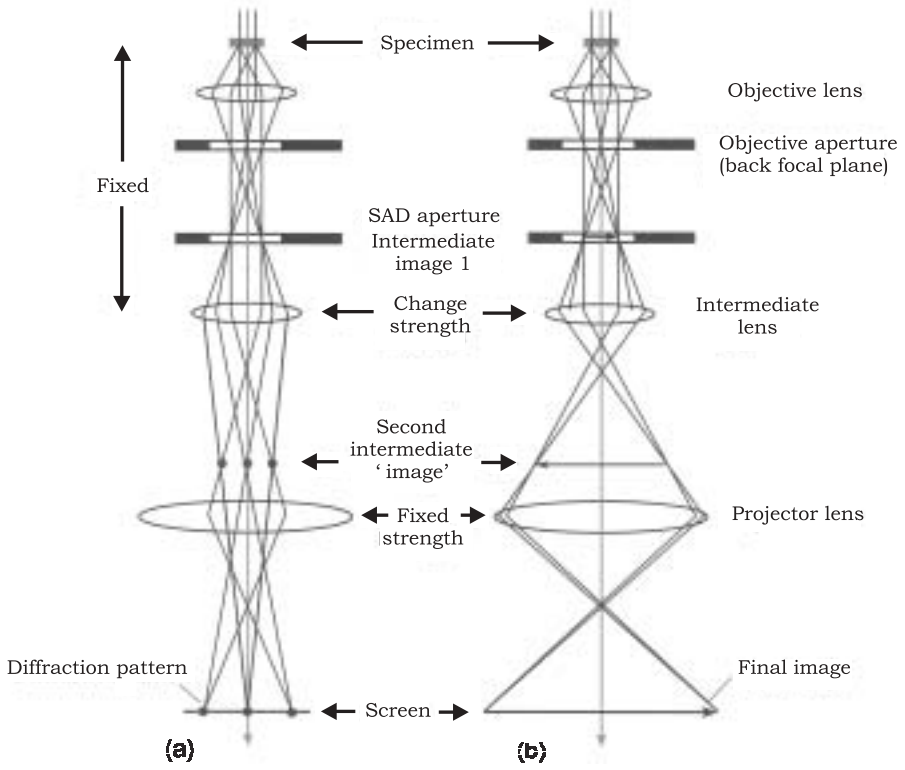

Figure 20. Ray diagram for the transmission electron microscope in the two different operation modes. (a) Diffraction mode: the intermediate lens has the back focal plane of the objective lens as its object. (b) Imaging mode: the intermediate lens has the image plane of the objective lens as its object [42].

For a specimen with constant thickness containing a crystalline material the contrast in the image is due to the crystal orientation (diffraction contrast). The SAD pattern contains a bright central spot from undiffracted electrons and a number of spots from the diffracted beam. By inserting an aperture (objective

aperture) into the back focal plane of the objective lens either the central spot or some/all of the scattered electrons can the selected. A bright field (BF) image is created if the objective aperture is centered over the direct beam and a dark field (DF) image is created if the objective aperture is centered over the diffracted beam. For DF imaging usually the beam is tilted so that the scattered electrons is centered on the optical axis (CDF) for obtaining higher resolution [41, 42].

The TEM work presented in this thesis is based on BF imaging (and diffraction patterns). The DF imaging could have been used for e.g. seeing precipitation or if the specimen had contained both Bi-2212 and Bi-2223, a diffraction spot from e.g. Bi-2212 could have been selected by the SAD aperture, and a DF image with Bi-2212 bright and Bi-2223 dark could have been obtained.

In Fig. 4 (chapter 2) is shown three electron diffraction patterns from a selected area of a Bi-2223 grain which is oriented to the low index zone axis [110], [010] and [100], respectively. A BF image can be seen in Fig. 8 and Fig. 9. The darkest grain in each image is oriented in the Bragg condition (equation 1) near to one of the three low index zone axes. By using a transmission electron microscope with an acceleration voltage of $\geq$ 400 kV high-resolution images on an atomic scale can be made. An example of a high-resolution BF image of a segment of a single Bi-2223 grain is seen in Fig. 3.

3.5.1 Orientation of the specimen

Before taking images it is imported to align the transmission electron microscope. The beam has to be directed along the optical axis for obtaining images with high resolution. After obtaining a well focused BF image the contrast can be improved by tilting the specimen, which is placed in a double tilt specimen holder, until one grain is oriented with the incoming beam parallel to one of the low index zone axes. In addition, the beam has to be a Bragg angle θ from one of the low index planes in order that a diffraction spot can be observed. θ is so small that the electron beam will be diffracted from electron planes almost parallel to it (Fig. 21).

Kikuchi lines are used for helping finding a low index zone axis. Inelastic scattering of electrons give a diffuse background with an intensity that varies with the angle of scattering and is maximal in the forward direction. Kikuchi lines are created by inelastically scattered electrons that subsequently are elastically scattered. Kikuchi lines consist of pairs of parallel light and dark lines separated with 2θ. The intensity of the Kikuchi lines and the diffraction spots increase and decrease, respectively, with increasing thickness of the specimen. The position of the Kikuchi lines is very sensitive to the specimen orientation whereas the diffraction spots only change intensity. Typically, a tilt of 1° shifts the Kikuchi lines 3 cm [41]. By switching the intermediate lens to the diffraction mode without inserting the SAD aperture the Kikuchi pattern can be seen at the viewing screen. By tilting the specimen until a prominent cross-over point in the Kikuchi pattern is centered over the central beam a well-oriented grain is obtained. By inserting the SAD aperture a final small adjustment of the specimen tilt can be done to obtain a nice symmetric diffraction pattern.

For identifying the diffraction pattern Bragg's Law: $\lambda = 2d\sin\theta$ (equation 1) is used. For small θ angles it becomes:

$$\lambda \cong 2d\theta \tag{8}$$

In Fig. 21 is shown the geometry of the diffraction pattern formation. The distance from the specimen to the screen is called the camera length L. The diffracted beam hits the screen a distance r from the undiffracted beam. We have: $\tan 2\theta = r/L$ and for small angles: $2\theta \cong r/L$. Combining this with equation 8, we find:

$$rd \cong L\lambda \tag{9}$$

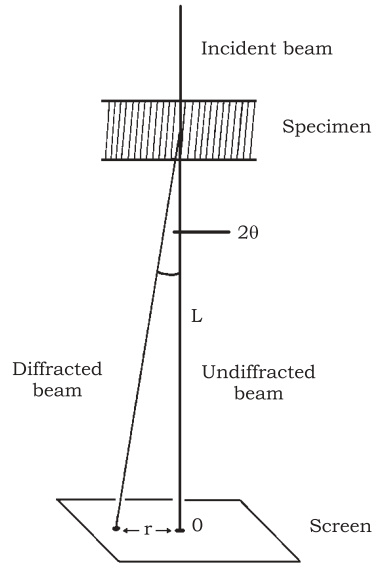

Figure 21. Schematic drawing of the geometry of diffraction pattern formation [41].

The camera length L and the wavelength λ of the electrons are constant for a specific setting. $L\lambda$ is called the *camera constant* [41]. It can be seen that the distance r at the diffraction pattern is inversely proportional with the interplanar spacing d of the diffracting planes. The ratio between the spacing of spots in the two different directions becomes (Fig. 22):

$$\frac{r_1}{r_2} \cong \frac{d_2}{d_1} \tag{10}$$

This formula can be used for checking whether the diffraction pattern originates from e.g. Bi-2212 or Bi-2223 or for determining the zone axis. For a tetragonal geometry the relationship between the d spacing and the lattice parameters is:

$$\frac{1}{d_{hkl}^2} = \frac{1}{b^2}(h^2 + k^2) + \frac{1}{c^2}l^2 \tag{11}$$

In Fig. 22 is shown a computer simulated diffraction pattern with [110] as zone axis (the corresponding TEM pattern can be seen in Fig. 4). The 002 and $2\overline{2}0$ reflection is indicated [18]. We can now check, as an example of identifying a diffraction pattern, whether it is from the Bi-2212 or Bi-2223 phase by finding d_2 by taking the ratio r_1/r_2 and multiply it with $d_1 = d_{002} = \frac{1}{2}c$ (equation 10 and 11). If we assume it is from the Bi-2223 phase $c \approx 37$ Å ($c \approx 31$ Å for Bi-2212), and $d_2 = d_{2\overline{2}0}$ becomes ~1.9 Å ($r_1/r_2 \approx 0.1$). By using equation 11, we find: $b = \sqrt{8}\ d_{2\overline{2}0}$ and b becomes 5.4 Å. Since this is the correct value for b, it is a diffraction pattern from Bi-2223.

For measuring the thickness of the grains and colonies along the c-axis direction one grain in the colony first has to be aligned for ensuring that the c-axis is lying in the image plane. The ab-plane twist ([001] twist boundary) of the grains inside a colony is investigated by orienting two grains besides each other along the same zone axis. In this way the specimen tilt difference is the ab-twist. The specimen tilt can be calculated from the two rotation labels at the microscope ("degree" and "second tilt indication").

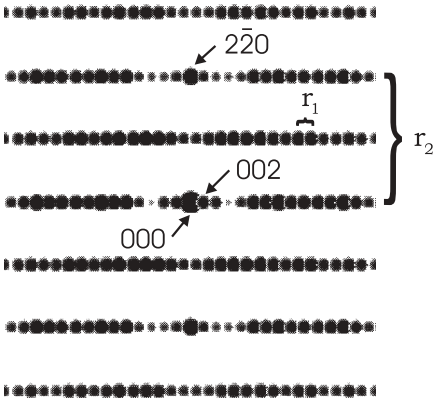

Figure 22. A segment of a computer simulated diffraction pattern of Bi-2223. The zone axis is [110]. The input parameters are the technical data of the JEOL 4000EX microscope (Table 4). The camera length is set to 1000 mm.

3.5.2 Equipment

The transmission electron microscopy (TEM) study is performed at EMAT, University of Antwerp (RUCA). For grain morphology and grain boundary angle investigations a Philips CM20 (200 kV) is used. High-resolution TEM (HRTEM) is carried out on a JEOL 4000EX (400 kV) with a point-to-point resolution of 1.7 Å. Further technical data of the two transmission electron microscopes is listed in Table 4.

Philips CM20	
Acceleration voltage:	200 kV
Electron gun:	LaB_6

JEOL 4000EX	
Acceleration voltage:	400 kV
Electron gun:	LaB_6
Spherical aberration coefficient C_s:	1.0 mm
Convergence semi-angle:	0.55 mrad
Spread of defocus:	80 Å
Size of objective aperture:	0.70 $Å^{-1}$ (in reciprocal space)
Point-to-point resolution:	1.7 Å

Table 4. Technical data of the transmission electron microscopes.

3.5.3 Sample preparation

It is crucial to have samples of high quality for TEM investigations. The sample preparation is difficult and has to be carried out very carefully. For high-resolution TEM imaging the sample may not be thicker than 20 nm at the places for examination. At the same time the original structure has to remain the same after the preparation of the sample.

From each tape both a longitudinal and a transversal cross-section TEM sample

are prepared by stacking two pieces of tape (cut at a length of $\lesssim$ 3 mm) together. This stack is sandwiched between two pieces of glass (Fig. 23).

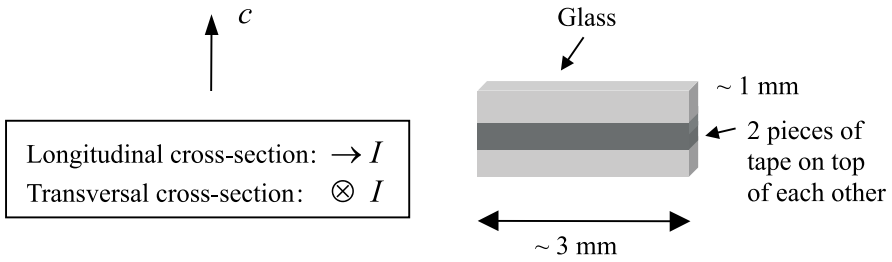

Figure 23. Preparation of TEM sample: Sketch of a stack of two pieces of tape sandwiched between two pieces of glass. The direction of the nominal c-axis of the Bi-2223 grains is shown. The direction of the superconducting current flow for the longitudinal and transversal cross-section TEM sample is also given.

It is mechanically polished by first using SiC paper and afterwards diamond papers with decreasing crystal size from 6 μm to 0.5 μm. After polishing the second side the thickness is $\sim$20 μm.

A copper grid ring with a diameter of 3 mm is then glued to one of the sides of the sample. In this way the sample fits into the microscope sample holder.

Finally, the sample is thinned by ion-milling. During the ion-milling the sample is lying with the copper grid down and exposed to the Ar ion beam from one of the "glass sides" (Fig. 24). The incident angle of the Ar ions is $\sim$10°. The ion-milling process is carried out at 4 kV and 1–2 mA. Afterwards the sample is turned upside down and is exposed from the same "glass side", now with an incoming angle of $\sim$5° and else with the same settings. The sample is ion-milled until some part of it near the hole (made by the Ar ions) is electron transparent. The electron transparent places can be seen in an optical microscope as "green light".

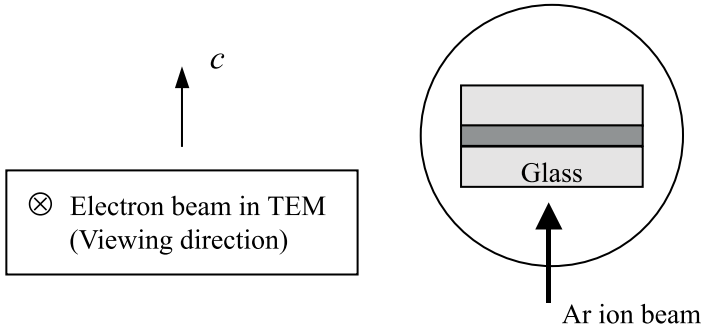

Figure 24. Preparation of TEM sample: Sketch of the sample on a copper grid showing the direction of the Ar ion beam. The later on direction of the electron beam in TEM is also given.

4 Phase development

The phase assembly of the green tapes (cf. section 3.2) has been investigated using Cu K_α X-ray diffraction (XRD) and SEM/EDS. Reflections corresponding to Bi-2212, Ca_2PbO_4, $(Ca,Sr)_{14}Cu_{24}O_{41-x}$ (14:24), Ca_2CuO_3 (2:1) and CuO are present in the XRD spectrum. By SEM/EDS a large amount of 14:24 particles with a size of ≤ 4 μm^2 are observed. In addition, 2:1 particles as large as $\sim$20 μm^2 are found.

The heat treatments used for the phase development studies have mainly been performed in 8% O_2. However, initially the annealings were performed in air. Therefore, the results presented in Paper 1 and 2 are from "air annealings". The equilibrium phenomena and kinetics are only investigated in air (cf. section 4.5).

The work presented in this thesis includes only one phase diagram study. For information on the phase equilibria in the Bi-Sr-Ca-Cu-O system, it is recommended to consult the review paper by Majewski [43].

4.1 Phase diagram in 8% O_2

In order to determine the temperature dependence of the phase profile in 8% O_2 a phase diagram is produced by taking twelve pieces of a multi-filamentary green tape (cf. section 3.2) and annealing them in 8% O_2 for $4\frac{1}{2}$ days (108 h) at the temperature 500 °C, 600 °C, 700 °C, 750 °C, 800 °C, 810 °C, 820 °C, 825 °C, 830 °C, 835 °C, 840 °C and 850 °C, respectively. The heating ramp was 100 °C/h. After 108 h at the annealing temperature the tapes were quenched vertically in oil to obtain a fast quenching, and thereby "freezing" the phases created at the annealing temperature. Unfortunately the temperature oscillated with $\pm$ 3 °C due to the vertical flow of 8% O_2 and 92% N_2.

The phases are identified by X-ray diffraction (XRD) using Cu K_α radiation ($\lambda = 1.54$ Å). The XRD was carried out on the surface of the tape after polishing away the outer silver sheath. All pieces of tapes are illuminated in 60 s per step, where each step is 0.05°.

The results are shown in Fig. 25. Bi-2223 is created at temperatures higher than $\sim$810 °C. In the range $\sim$810–825 °C Bi-2223 and Bi-2212 coexist. At temperatures below $\sim$820 °C the secondary phases $(Ca,Sr)_2PbO_4$, 3221 (from 750 °C) and $(Ca,Sr)_{14}Cu_{24}O_{41-x}$ (14:24) are present. Bi-2201 is not observed. The tapes contain CuO for all twelve annealing temperatures. It also seems to $(Ca,Sr)_2CuO_3$ (2:1) is present at all temperatures, but many of these reflections are overlapping with reflections from other phases. To examine the cuprates further, three tapes (500 °C, 820 °C and 840 °C) were selected for SEM/EDS analysis. In the tape annealed at 500 °C a large amount of 14:24 were found. At 820 °C the 1:1 phase ($(Ca,Sr)CuO_2$) was observed. At 840 °C the tape contains many big CuO particles of the size of $\sim 5 \times 5$ μm^2. In addition, smaller pieces of 2:1 were detected. The Bi-2223 grains close to big CuO particles are mis-aligned i.e. the big secondary phases should be avoided during the tape processing.

In Fig. 26 and Fig. 27 are shown the XRD intensities of Bi-2212/Bi-2223 and the secondary phases, respectively. The intensities are the raw intensities. Normalization to the background level and/or the silver amount (multiplying with the silver peak intensity for correction of the filling factor) gave curves with the same trend. Due to the difficulty in normalization a large uncertainty is associated with the XRD intensity values. In addition, a texture effect is present. The peak for Bi-2212 at 820 °C is due to a better texturing.

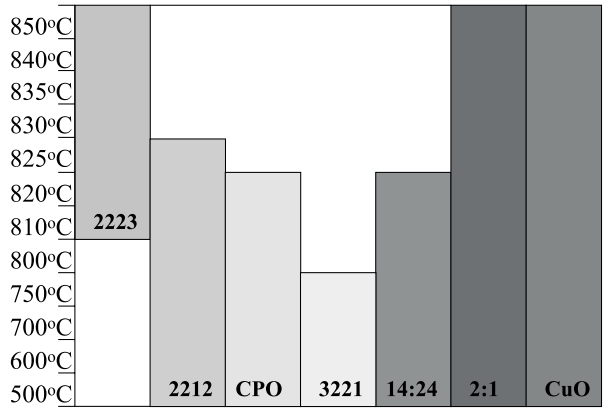

Figure 25. Phase diagram showing the phases in tapes annealed for 108 h in the temperature range 500–850 °C. CPO is short for $(Ca,Sr)_2PbO_4$.

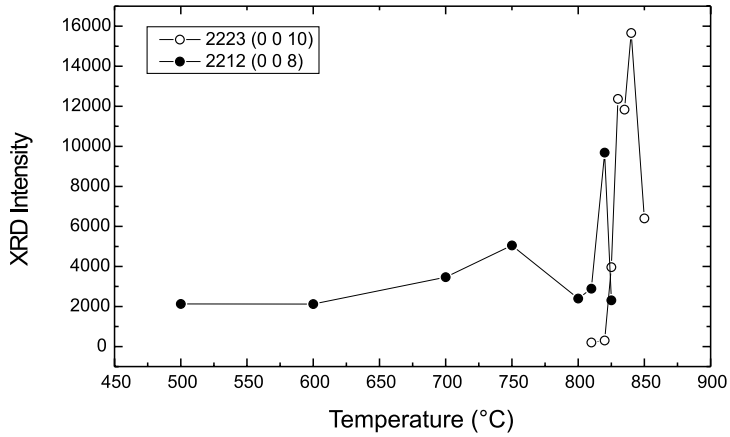

Figure 26. XRD intensities of Bi-2212 and Bi-2223 at the different annealing temperatures.

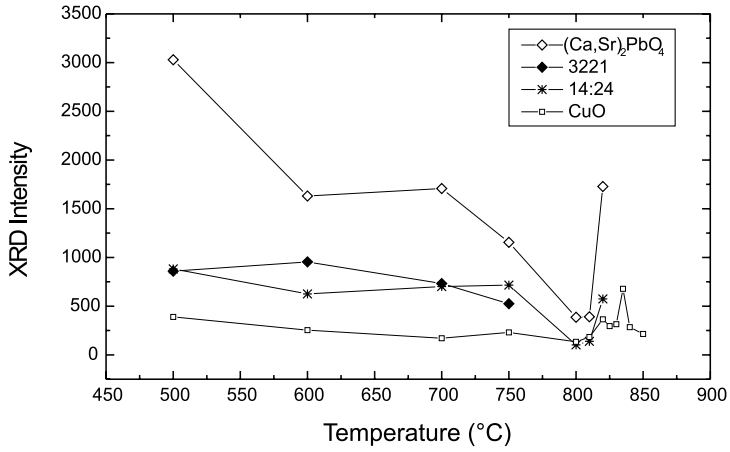

Figure 27. XRD intensities of secondary phases at the different annealing temperatures.

4.2 1st annealing in 8% O_2

At the synchrotron source in Hamburg an *in situ* X-ray diffraction experiment has been performed on a mono-filamentary green tape in 8% O_2. The duration of the

annealing was ∼11.5 h at the temperature of 829.5 °C. The heating and cooling ramp was 100 °C/h.

The data is analyzed as explained in section 3.3.2. In Fig. 28 is shown the phase development of Bi-2212, Bi-2223, Bi-2201, $(Ca,Sr)_2PbO_4$ and $(Ca,Sr)_2CuO_3$ during the annealing[9]. At temperatures below ∼500 °C during heating a constant amount of Bi-2212, the secondary phases $(Ca,Sr)_2PbO_4$ and $(Ca,Sr)_2CuO_3$ (reflection at $d \approx 6.2$ Å, the amount of this phase is somewhat uncertain) is present in the tape. When the temperature reaches 790 °C the $(Ca,Sr)_2PbO_4$ phase decomposes quickly and disappears at 829 °C. The Bi-2212 content decreases just after the annealing temperature is reached while the desired Bi-2223 phase appears and increases during the annealing. The Bi-2223 content saturates after 10 h annealing on a level of 93%. During cooling at 729 °C the $(Ca,Sr)_2PbO_4$ phase appears again and exists down to ∼500 °C, where the measurement was stopped. The Bi-2201 phase appears during cooling at the temperature of 740 °C and remains there until the measurement was stopped.

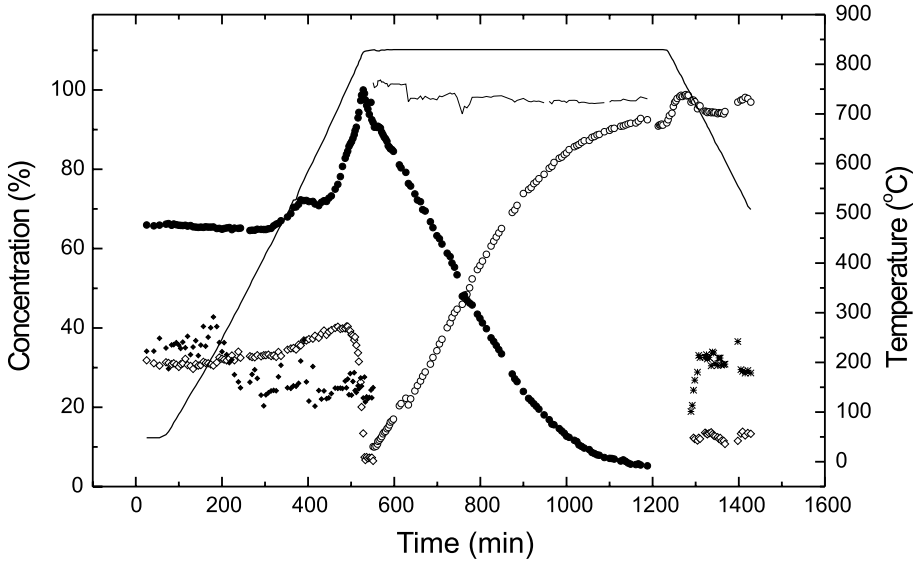

Figure 28. Relative concentrations of the different phases during annealing. The symbols refer to: (●) Bi-2212 (008), (○) Bi-2223 (0 0 10), (∗) Bi-2201 (006), (◇) $(Ca,Sr)_2PbO_4$ (020), (⧫) $(Ca,Sr)_2CuO_3$ (200) and (—) Bi-2212 + Bi-2223. Bi-2201 and $(Ca,Sr)_2CuO_3$ are in arbitrary units. The thick solid line marks the temperature profile with reference to the temperature scale at the right-hand side.

A multi-filamentary tape, placed beside the mono-filamentary tape, was illuminated at every second exposure. In the raw 2D images a similar phase development can be observed for the multi-filamentary tape during the annealing. The present phases are the same. A small difference in the reaction rate has been found. The intensity of the Bi-2212 (008) and Bi-2223 (0 0 10) reflection are identical 50 min earlier for the multi-filamentary tape compared to the mono-filamentary tape. Furthermore, a room temperature synchrotron radiation measurement of a multi-filamentary tape annealed in the same way has been performed. The observed phases are Bi-2223, $(Ca,Sr)_2PbO_4$ and Bi-2201. This is in good agreement with the final phases observed in the *in situ* experiment on the mono- (and multi-) filamentary tape.

[9] 14:24 and CuO cannot be detected by the synchrotron X-ray diffraction due to a lower resolution and signal-to-noise ratio (because of the present silver sheath) compared to the Cu K_α XRD.

The evolution of the full width at half maximum (FWHM) of a Bi-2212 and a Bi-2223 diffraction peak in the 2θ projection is presented in Fig. 29. The Bi-2212 linewidth decreases during heating and then levels off (for 5 h) after the annealing temperature is reached (the subsequent increase of the Bi-2212 linewidth is due to a fitting error because of an increasing tail from the nearby Bi-2223 (0 0 10) reflection). The linewidth of Bi-2223 decreases quickly in the beginning and levels off afterwards to a value higher than Bi-2212. A decrease in the linewidth indicates that the strain relief and/or the crystal size increases during the annealing. By analyzing several (00l) reflections from previous experiments (presented in Paper 1 and 2), where the (002) reflection is visible, it has been found that the decrease of the Bi-2212 linewidth corresponds primarily to a decrease of the strain, while the decrease of the Bi-2223 linewidth corresponds to an increase of the grain size[10].

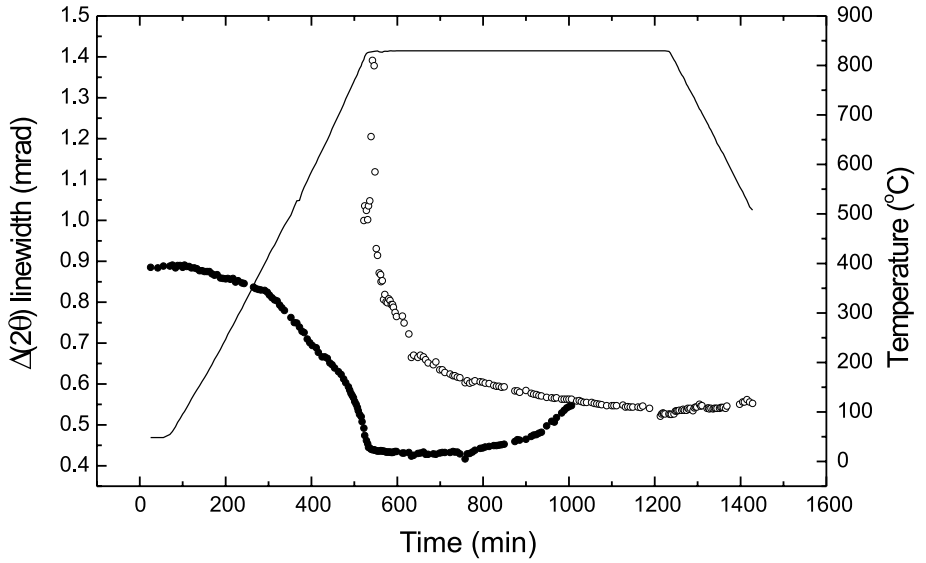

Figure 29. The evolution of the linewidth (2θ FWHM). The symbols refer to: (•) Bi-2212 (008) and (○) Bi-2223 (0 0 10). Data points from Bi-2212 are removed after 1000 min because of an unreliable fitting due to vanishing intensities. The solid line marks the temperature profile with reference to the temperature scale at the right-hand side.

Fig. 30 shows the 2θ position of the midpoint of the Bi-2212 (008) and the Bi-2223 (0 0 10) reflection during the annealing. The changes in 2θ due to the thermal lattice expansion/contraction are drawn as a line. At 700 °C the Bi-2212 2θ midpoint begins to deviate from the theoretical curve. This means that the d spacing is also changing due to another effect than thermal expansion. In addition, the integrated intensity for the Bi-2212 peak increases steeply between 670 °C and 825 °C (Fig. 28) where the contraction also takes place. Two possible causes for the contraction of the lattice can be strain and changes in the stoichiometry. From previous experiments performed in air (presented in Paper 1 and 2) we have observed that the 2θ midpoint of the Ag peak follows the expected temperature variation. Several groups have reported on an incorporation of Pb and possible Ca into the Bi-2212 lattice during the last part of the heating [44, 45]. This is in agreement with the fact that the solubility of Pb in Bi-2212 is higher at higher temperatures (the Pb solubility has maximum at 850 °C in air for pressed pellets without silver) [46]. Our results of lattice contraction can be explained by this incorporation of Pb and/or Ca in the Bi-2212 lattice [26, 47], and the increase

[10] $\mathrm{FWHM}_{strain}(2\theta) \propto \tan 2\theta \approx 2\theta$ and $\mathrm{FWHM}_{size}(2\theta) \propto \frac{1}{\cos 2\theta} \approx 1$.

in the integrated intensity is due to changes in the structure factor (more details can be found in Paper 1). Furthermore, the increase in the integrated intensity of the Bi-2212 peak and the decrease in the $(Ca,Sr)_2PbO_4$ peak seems to follow each other. This is consistent with a model where Bi-2212 and $(Ca,Sr)_2PbO_4$ react to form Pb-rich Bi-2212 before it converts into Bi-2223.

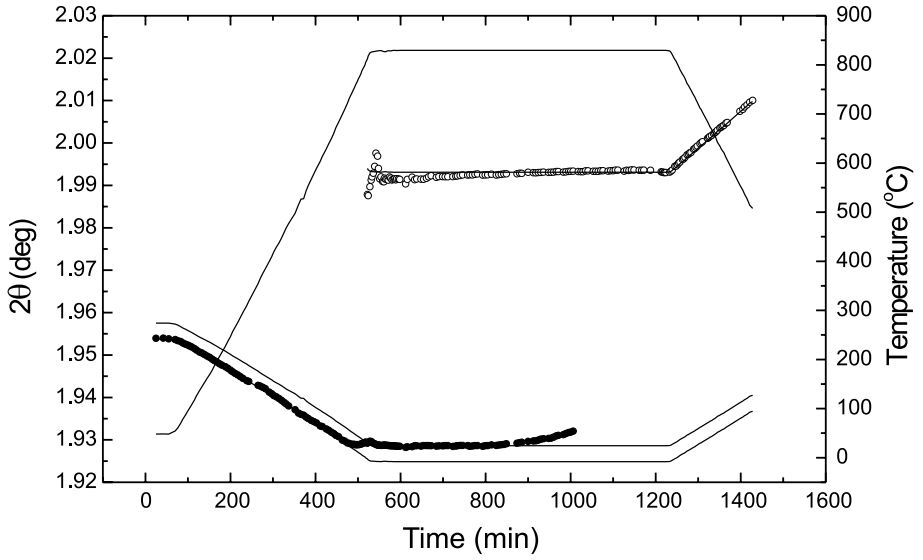

Figure 30. The position of the Bi-2212 (008) (•) and the Bi-2223 (0 0 10)(○) peak midpoint in the 2θ projection as function of the annealing time. The lines are the theoretical lattice expansion curves under the assumption that the changes in the 2θ position only are related to thermal expansion/contraction. The linear thermal expansion coefficient is $\alpha = 19\times10^{-6}\ K^{-1}$ and $\alpha = 26\times10^{-6}\ K^{-1}$ for Bi-2212 and Bi-2223, respectively. Data points from Bi-2212 are removed after 1000 min because of an unreliable fitting due to vanishing intensities. A line is also marking the temperature profile with reference to the temperature scale at the right-hand side.

The reduction of the integrated intensity of the Bi-2212 peak at 825 °C, 23 min before the Bi-2223 phase appear, can be due to a partial dissolution of Bi-2212 into a liquid. This is confirmed by the fact that the background level, which is proportional to the amount of liquid, begins to increase at this annealing time. This is also consistent with the study by Giannini *et al.* [5] showing a decrease in the total crystalline matter at this stage.

The Bi-2223 2θ midpoint is following the thermal expansion/contraction curve during the whole annealing except at the time where the Bi-2223 concentration is very small. Since the Bi-2223 2θ midpoint follows the thermal curve, the increase of the integrated intensity at the very end of the annealing may be due to other effects than stoichiometry changes such as a real concentration increase or more likely a sample holder contraction (the integrated intensity of Bi-2212 is also increasing at this time. The data points are removed because of an unreliable fitting due to vanishing intensities). Using *in situ* neutron diffraction in air Giannini *et al.* [5] have observed that the Bi-2212 amount increases during cooling simultaneously with the Bi-2223 phase remains constant. They interpret this result as the recrystallization of Bi-2212 does not correspond to a decomposition of Bi-2223, but is associated with a decrease of the Bi-2201 and $(Ca,Sr)_{14}Cu_{24}O_{41-x}$ (14:24) phase. In our studies performed in 8% O_2 and in air (cf. figure 2 Paper 1) the amount of the Bi-2201 phase increases during cooling simultaneously with an increase of the integrated intensity of the Bi-2212 phase.

As supplement to the synchrotron X-ray diffraction results phases found by Cu K_α XRD can be measured. Liu *et al.* [48, 49] has performed a study of the phase evolution at the early annealing stage by annealing multi-filamentary tapes at 830 °C in 8% O_2 for different durations between 0–52 h followed by an air quench. The XRD intensities show 14:24 from 0 h annealing (the temperature has just reached 830 °C) with a maximum after 1 h. The successive decay of 14:24 has a rate similar to the Bi-2212 decay. 14:24 disappears again after 20-30 h. CuO appears after ∼10 h annealing and Bi-2201 after ∼5 h, which is from solidified liquid. In addition, Ca_2PbO_4 and $(Ca,Sr)_2CuO_3$ (2:1), which also can be detected by the synchrotron, have been observed. Ca_2PbO_4 disappears after 1 h and 2:1 is detected for all durations from 0–52 h with a maximum after ∼10 h. Furthermore, Fahr *et al.* [50] have by *in situ* neutron diffraction studied the phase development of a multi-filamentary tape during the first annealing for 25 h in a reduced oxygen atmosphere. The Bi-2223 phase, Ca_2PbO_4 and 14:24 are shown from the annealing temperature at 825 °C is reached [50]. The amount of 14:24 increases until 2.5 h annealing time and then decreases. The Ca_2PbO_4 phase disappears after ∼8 h annealing time. In our study this phase disappears at ∼0 h annealing time. This difference can be explained by the fact that the precursor powder used by Fahr *et al.* [50] contains more Pb (Pb = 0.4) than our powder (Pb = 0.33). In addition, the reaction rate of the study in Ref. [50] is slower, most probably due to the lower annealing temperature.

4.2.1 Comparison with annealing in air

Before the experiment "1st annealing in 8% O_2" a 1st annealing experiment in air has been performed. The annealing temperature was 835 °C. The results and a detailed analysis are presented in **Paper 1**.

By comparing the relative concentration vs. the annealing time of the annealing in 8% O_2 and air[11] (Fig. 28 and figure 2 Paper 1), we observe that the phases presented in the X-ray patterns are similar and that the development of these has nearly identical trends. The $(Ca,Sr)_2CuO_3$ (2:1) phase is an exception. In the 8% O_2 annealing it seems to this phase is present in the tape from the beginning of the annealing. In the case of the annealing in air 2:1 appears when the Bi-2212 concentration starts to decrease and it decreases successively with a rate similar to Bi-2212 (Bi-2212 → liquid + $(Ca,Sr)_2CuO_3$). From the Cu K_α XRD results in 8% O_2 [48] and the neutron diffraction results in reduced oxygen [50] presented in the end of the previous section, we observe that the evolution of 14:24 is similar to the evolution of 2:1 from the annealing in air (figure 2 Paper 1). One hypothesis could be that 14:24 "replaces" 2:1 in 8% O_2 and the reaction becomes: Bi-2212 → liquid + $(Ca,Sr)_{14}Cu_{24}O_{41-x}$.

The conclusions of the analysis of the evolution of the linewidth and the position of the 2θ midpoint are similar for the annealing in 8% O_2 and air. An exception is that for the annealing in air the Bi-2212 lattice expands (the 2θ midpoint decreases) during the conversion into Bi-2223 (figure 5 Paper 1), indicating that the remaining Bi-2212 grains contain less and less Pb. In contrast to this, the annealing in 8% O_2 indicates no further stoichiometry changes after the incorporation of Pb.

By analyzing the steep increase of the Bi-2212 concentration during heating we observe an increase of ∼30% and ∼20% in the case of annealing in 8% O_2 (Fig. 28) and in air (figure 2 Paper 1), respectively. This is consistent with the fact that a lower oxygen partial pressure results in a higher Pb solubility of Bi-2212 [26].

[11] Note that the nominal powder composition of the tapes used in these two experiments is not identical.

The phases present and their evolution are as mentioned similar, but an important difference is the reaction rate. For the annealing in 8% O_2 an equal content of Bi-2212 and Bi-2223 is obtained after 230 min at the annealing temperature, whilst for the annealing in air this is not the case until 560 min at the annealing temperature. In other words, the conversion in 8% O_2 is more than twice as fast as in air. Of course this comparison only makes sense if the annealing temperatures are comparable, as in the case where the temperatures are chosen so the reaction rate is fastest for both the annealing in 8% O_2 and in air.

4.3 Last annealing in 8% O_2

An *in situ* synchrotron radiation experiment has been performed on a monofilamentary tape, which beforehand was annealed in 8% O_2 and was "fully" converted into Bi-2223. The last annealing at the synchrotron was also performed in 8% O_2.

Unfortunately, we had problems with the furnace during this experiment, meaning that the temperature in the furnace rapidly decreased after 480 min. Therefore, only a limited amount of the data from the planned annealing is available. The temperature profile of the last annealing can be seen in Fig. 31.

In the diffraction patterns, we have observed reflections from $(Ca,Sr)_2PbO_4$ and Bi-2223. No other phases are present. The background level in the vicinity of the $(Ca,Sr)_2PbO_4$ reflection is very steep and high. Therefore, it cannot be fitted. The $(Ca,Sr)_2PbO_4$ reflection can be observed in the raw images from the beginning at the experiment at 311 °C and is present until 825 °C. The (115) reflection is selected for analysis of the Bi-2223 phase development. The concentration (in arbitrary units) during the annealing is shown in Fig. 31. Within the uncertainty the Bi-2223 phase seems to be constant. The linewidth of Bi-2223 (115) shown in Fig. 32 also seems to be constant.

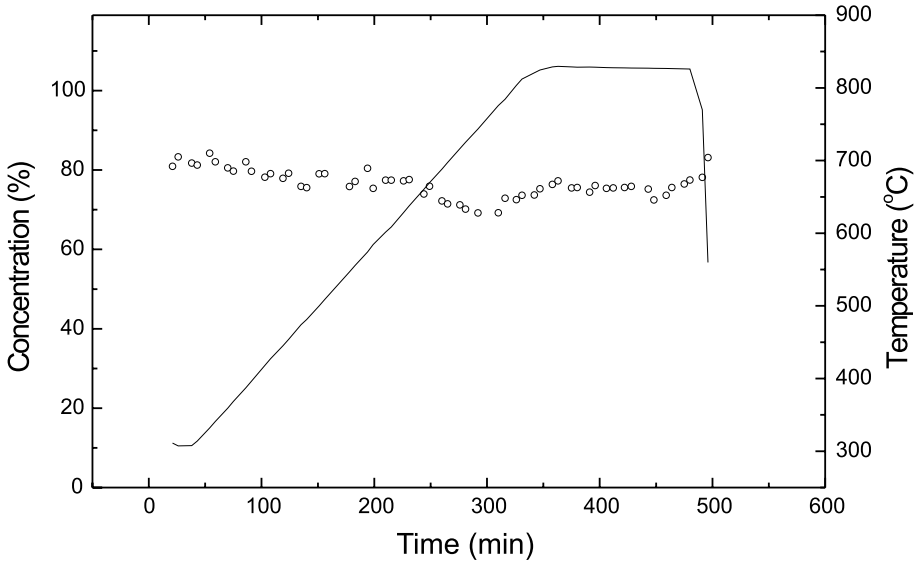

Figure 31. Concentration (in arbitrary units) of Bi-2223 (115) (○) during annealing. An injection took place around 300 min. The solid line marks the temperature profile with reference to the temperature scale at the right-hand side.

The evolution of the 2θ midpoint of the Bi-2223 (115) reflection follows closely the thermal expansion curve (Fig. 33). Thus, it can be concluded that the Bi-2223

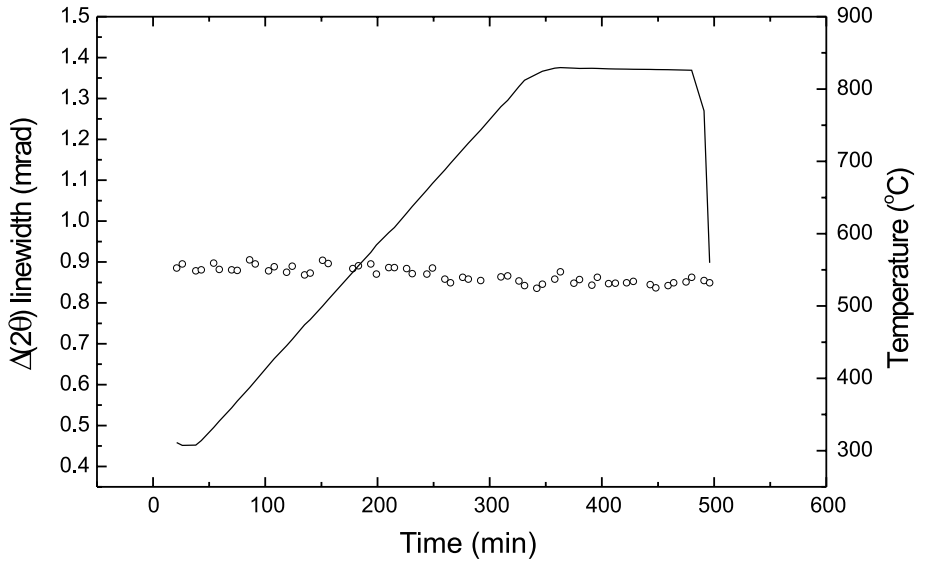

Figure 32. The evolution of the linewidth (2θ FWHM) of Bi-2223 (115)(○). The solid line marks the temperature profile with reference to the temperature scale at the right-hand side.

phase does not change stoichiometry in the last part of the heating as is the case for the Bi-2212 phase.

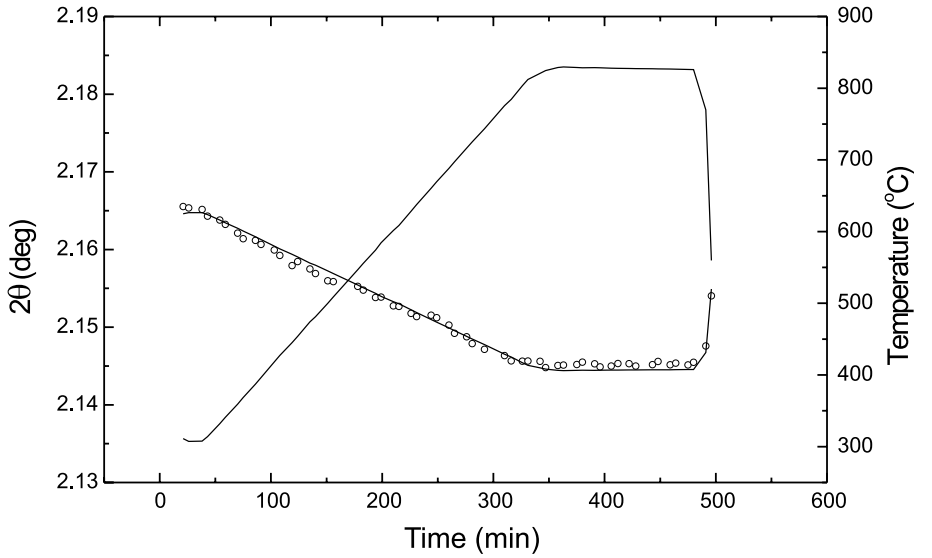

Figure 33. The position of the Bi-2223 (115) peak midpoint (○) in the 2θ projection as function of the annealing time. The line is the theoretical lattice expansion curve under the assumption that the changes in the 2θ position only are related to thermal expansion/contraction. The linear thermal expansion coefficient is $\alpha = 18 \times 10^{-6}\ K^{-1}$. A line is also marking the temperature profile with reference to the temperature scale at the right-hand side.

4.4 Transformation kinetics

In **Paper 1** an analysis and a discussion of the transformation kinetics based on the *in situ* synchrotron radiation experiment "1st annealing in air" are presented. This section is a summary of the conclusions reached there.

The exponents (reaction orders) of the fractional conversion equation referred to as the Johnson-Mehl-Avrami relation of the transformation kinetics are found to be: $1 < m < 2$ for both the Bi-2212 and the Bi-2223 phase[12]. According to Matsubara *et al.* [51] the m value gives information on the growth dimension, the nucleation rate and what the growth is controlled by during the phase transformation. The range of m values that we find is consistent with a diffusion controlled 2D or 3D growth with decreasing nucleation rate ($2 < m < 3$ corresponds to phase-boundary controlled).

The m values are also found to be between 1 and 2 by analyzing the data from the "1st annealing in 8% O_2". The corresponding Johnson-Mehl-Avrami plots for Bi-2223 and Bi-2212 can be seen in Fig. 34 and Fig. 35, respectively.

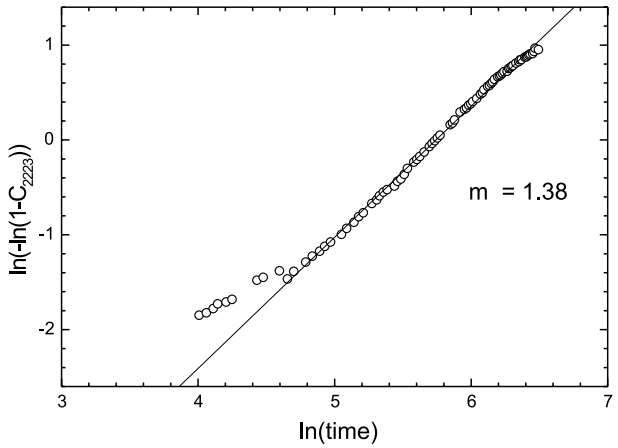

Figure 34. A Johnson-Mehl-Avrami plot (∘) using the Bi-2223 concentrations displayed in Fig. 28 as the fractional conversion C, where $C(t) = 1 - \exp(-(Kt)^m)$ *and K is the rate constant. The plot is constructed by setting t = 0 at 528 min, where the Bi-2212 concentration is 100% and the annealing temperature is reached (cf. Fig. 28). The line is a linear fit to the data set truncated by the first 9 points. The fitted slope is* $m = 1.38$ *and* $m \ln K = -7.94$.

Two different transformation mechanisms have been postulated in the literature, an intercalation model and a nucleation-and-growth model. Our results show that the texture of the Bi-2223 grains follows the texture evolution of the Bi-2212 grains (figure 3 Paper 1). This is in agreement with both models if the Bi-2223 grains nucleate on exiting Bi-2212 colonies. The linewidth of Bi-2212 is found to be constant during the conversion into Bi-2223 (figure 4 Paper 1), indicating that no or low strain and finite-size broadening of the diffraction peaks occur. An intercalation process may imply strain along the *c*-axis. The results point to a mechanism where only few Bi-2212 grains transform at a given time and the transformation of each grain is very fast. The most probable transformation mechanism is concluded to be a nucleation-and-growth model with a fast decomposition of the individual Bi-2212 grains, followed by a growth of the Bi-2223 phase from Bi-2212 melt reacting with $(Ca,Sr)_2CuO_3$.

Due to the high similarity of the results from annealing in air and in 8% O_2

[12] Analysis of other *in situ* experiments in air have also given values of m between 1 and 2.

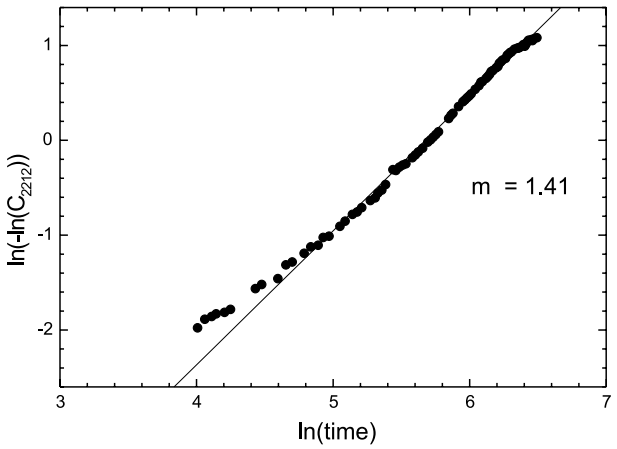

Figure 35. A Johnson-Mehl-Avrami plot for the Bi-2212 concentration (•). The line is a linear fit to the data set truncated by the first 8 points. The fitted slope is $m = 1.41$ and $m \ln K = -8.02$.

the arguments of the transformation mechanism can be transferred to the annealing in 8% O_2. The growth of Bi-2223 are then from Bi-2212 melt reacting with $(Ca,Sr)_{14}Cu_{24}O_{41-x}$ (14:24) if our hypothesis is correct.

4.5 Equilibrium and kinetics

In **Paper 2** an *in situ* study by synchrotron X-ray diffraction with a slow ramping starting from 750 °C, followed by two high temperature cycles to study equilibrium phenomena and kinetics is presented. This section contains a selection of the analysis related to this high temperature cycling.

For the first time, the amount of the partial liquid is directly monitored. The liquid phase is found by investigation of the background level at $2\theta = 2.15°$.

A comparison of the phase development of Bi-2212, Bi-2223, 3221 (or 3321), $(Ca,Sr)_2PbO_4$ and the liquid is shown in Fig. 36. In addition to the results obtained from the annealing shown in Fig. 28, we observe a Pb-rich 3221 phase, which dissolves and disappears at 789 °C during heating (Fig. 36).

In Fig. 37 a close-up of the last third of the annealing is shown. This figure also include the $(Ca,Sr)_2CuO_3$ phase. Above 839 °C Bi-2212 partially melts as the liquid phase and $(Ca,Sr)_2CuO_3$ increase. The change in the concentrations of the liquid phase and $(Ca,Sr)_2CuO_3$ follows the temperature change. During the high temperature cycles, the concentrations of the different phases have approximately the same values whenever the temperature is 845 °C. This implies that the melting and precipitation process is reversible. However, the reaction of $(Ca,Sr)_2CuO_3$ is less reversible. In the close-up on the second high temperature cycle shown in Fig. 38, we also observe that the formation and decomposition kinetics of $(Ca,Sr)_2CuO_3$ are slower. This may be due to the fact that the grains are much larger than those of the other phases ($(Ca,Sr)_2CuO_3$ appears as dots in the raw 2D image and in SEM imaging this cuprate is seen as big particles).

Due to the high similarity of the results obtained from annealing in air and in 8% O_2 one should expect that most of the equilibrium and kinetics results also are valid in the case of 8% O_2. An exception is if the $(Ca,Sr)_2CuO_3$ (2:1) obtained in air is "replaced" by 14:24 when annealing in 8% O_2, and since the 14:24 particles not are quite as big as the 2:1 particles the kinetics of 14:24 may not be as slow as the 2:1 kinetics.

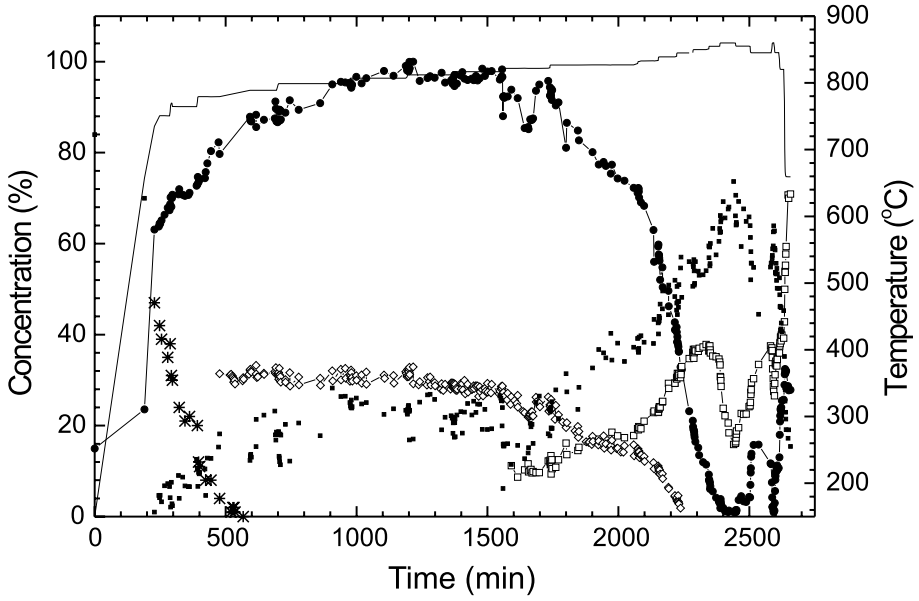

Figure 36. Relative concentrations of Bi-2212 (115) (•), Bi-2223 (115) (□) and $(Ca,Sr)_2PbO_4$ (110) (◇) during annealing in air. In addition, points proportional to the amount of 3221 and liquid are marked by (∗) and (■), respectively. The line marks the temperature profile with reference to the temperature scale at the right-hand side.

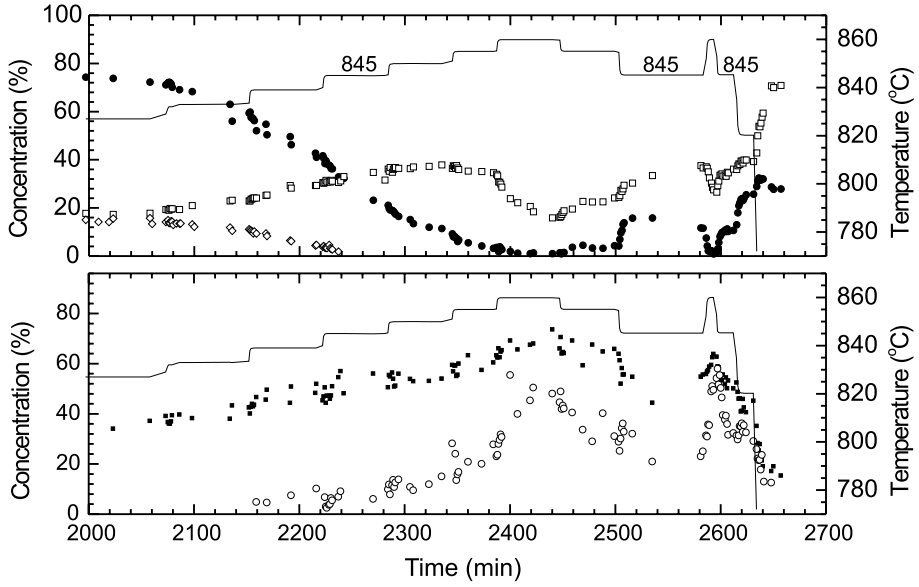

Figure 37. Close-up on the last third of the annealing. Shown above are the relative concentrations of Bi-2212 (•), Bi-2223 (□) and $(Ca,Sr)_2PbO_4$ (◇) (cf. Fig. 36). Shown below are the relative concentrations of $(Ca,Sr)_2CuO_3$ (○) and a liquid (■). The lines mark the temperature profile with reference to the temperature scale at the right-hand side.

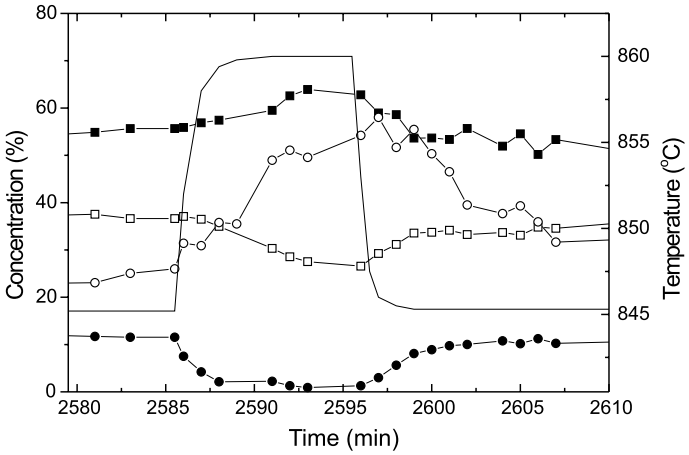

Figure 38. Close-up on the second high temperature cycle. The relative concentrations of Bi-2212 (•), Bi-2223 (□), $(Ca,Sr)_2CuO_3$ (○) and a liquid (■) as function of the annealing time. Data points are identical to the ones presented in Fig. 36 and Fig. 37. The line without dots marks the temperature profile with reference to the temperature scale at the right-hand side.

4.6 *In situ* study of individual grains by 3DXRD

In section 3.3.4 the overall idea and principles of the 3DXRD microscope experiment were explained. The results are placed in this section.

The green mono-filamentary tape was annealed in air for 12 h of annealing at 838.5 °C. At the beginning of the annealing the diffraction pattern consisted of segmented Debye-Scherrer powder rings. At 825 °C the diffraction spots from grains appeared. In Fig. 39 is shown an example of a raw 2D image showing the diffraction spots from grains.

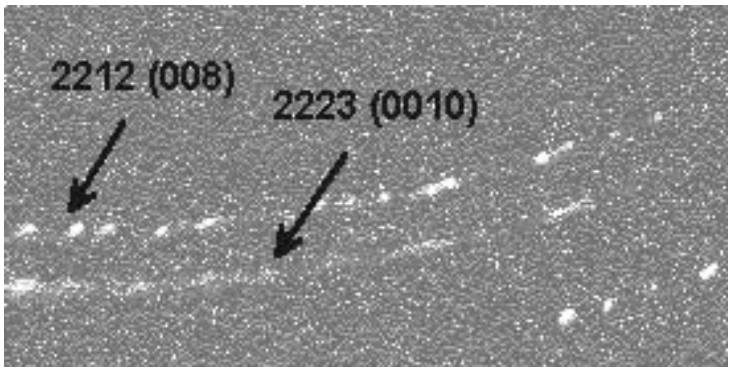

Figure 39. Detail of image acquired after 11.5 h of annealing at 838.5 °C in air. Dots appearing on the (008) and (0 0 10) Debye-Scherrer rings associated with the Bi-2212 and Bi-2223 phases, reflect the transformation from Bi-2212 to Bi-2223.

The diffraction patterns contain approximately 60 diffraction spots. Due to an unfortunate setting of the beam size only four diffraction spots were found to be approximately "valid" (cf. section 3.3.4). In Fig. 40 the evolution of the intensity of the four constantly valid diffraction spots are shown. One of them is from a Bi-2223 grain (○) and the others are from Bi-2212. The integrated intensity, which

is proportional to the grain volume, does in all cases increase to a maximum where after they decrease and finally disappear. The appearance of new Bi-2212 grains after ∼4–7 h annealing time indicates a dynamic behavior, where the individual grains crystallize again and transform at different times.

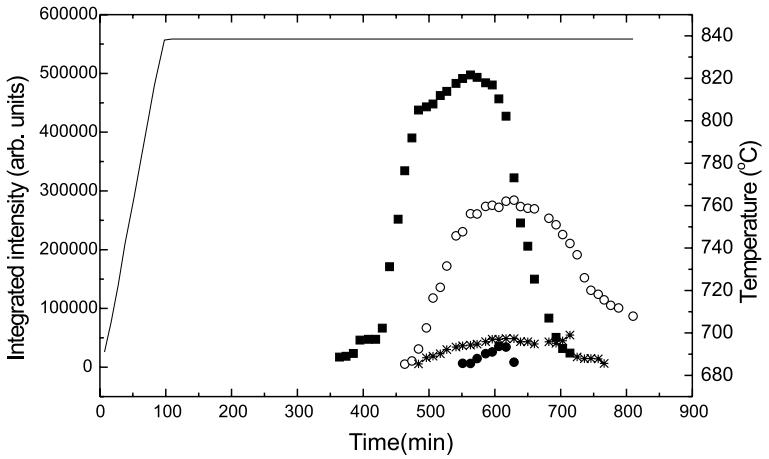

Figure 40. Relative integrated intensities of four diffraction spots during annealing in air. The symbols refer to: (•) Bi-2212 (117), (■) Bi-2212 (117), (○) Bi-2223 (119) and (∗) Bi-2212 (020). The solid line marks the temperature profile with reference to the temperature scale at the right-hand side. The (•) spot appears after 7.4 h at the annealing temperature and is present for 1.3 h, (■) after 4.3 h for 5.8 h, (∗) after 6.3 h for 4.7 h and the (○) spot from Bi-2223 appears after 5.9 h and is still present at the last exposured image 5.8 h later.

The position of the dots during the annealing is illustrated in Fig. 41. The uncertainty of the beam center is too large to determine whether the spots only are moving along the Debye-Scherrer rings as they would if the grain is rotated or a change in the radial angle θ as in the case of stoichiometry changes is also present.

This was the first time that the behavior of the individual grains within a ceramic was observed. In general, it will be feasible to study the kinetics as a function of the stoichiometry, orientation and/or grain size by using the 3DXRD microscope.

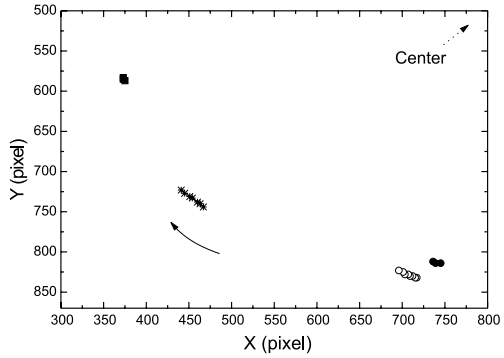

Figure 41. Position of the four diffraction spots during annealing. The symbols refer to: (•) Bi-2212 (117), (■) Bi-2212 (117), (○) Bi-2223 (119) and (∗) Bi-2212 (020). The arrow indicates the direction of the spots movements.

4.7 Grain and colony thickness

In **Paper 4** TEM results of grain and colony thickness, angles of c-axis tilt grain boundaries and intergrowth are presented. Tapes with different process parameters have been compared with respect to the microstructure. The identification of the sample 1–3 is shown in Table 1 in section 3.2 or in table 1 Paper 4. In this section a summary of the grain and colony thickness results is placed. The intergrowth results are presented in section 4.8 and the angles of c-axis tilt in section 5.3. A discussion based on the effect of the annealing time and intermediate pressing of the results related to the grain and colony thickness, angles of c-axis tilt, the intergrowth and the I_c values is found in Paper 4.

We have studied the grain and colony thickness in many different areas for each TEM sample (both in the transversal cross-section and in the longitudinal cross-section). The results are shown in Fig. 42 and Table 5. The average grain thickness for sample 1 is 30.5 ± 1.3 unit-cells[13]. The peak maximum is at 25–28 unit-cells. In sample 2 the average grain thickness is found to be 20.7 ± 1.1 unit-cells. The peak maximum is at 13–24 unit-cells. The grains in the fully processed tape are on the average 50% thicker than after 1st annealing. The grains in sample 3 are found to be thicker than in sample 2. In sample 3 the average grain thickness is 27.9 ± 1.3 unit-cells. The distribution of the grain thickness for sample 3 shows a larger variation of the grain thicknesses. The histogram has a peak maximum at the same thicknesses as sample 2 plus lower peaks at higher grain thicknesses. The average value of grain thickness for sample 1 and 3 are similar but the distributions are not.

	Colony thickness			Average grain thickness (unit-cells)	Number of grains per colony
	Min (μm)	Max (μm)	Average (μm)		
Sample 1	0.4	1.2	0.73 ± 0.09	30.5 ± 1.3	6.5 ± 1.1
Sample 2	0.1	0.8	0.40 ± 0.03	20.7 ± 1.1	5.2 ± 0.7
Sample 3	0.2	1.7	0.69 ± 0.09	27.9 ± 1.3	6.7 ± 1.2

Table 5. The minimum, maximum and average values of the colony thickness for sample 1–3. The average values of grain thickness and number of grains per colony are also listed.

Besides the grain thickness the colony thickness is also important for the current path. The minimum, maximum and average values of the colony thickness are shown in Table 5 for sample 1–3. The fully processed tape (sample 1) has thicker colonies than the tape after the 1st annealing (sample 2). Sample 3, which has been annealed for a longer time than sample 2, also has thicker colonies. The colony thicknesses of sample 1 and sample 3 are similar. Furthermore, the average number of grains per colony is calculated (Table 5). Within the statistical uncertainty, this number has the same value for each sample. These results indicate that the grain growth and colony growth are correlated.

We have observed that longer annealing times result in thicker grains and colonies (compare sample 2 and 3) and that the effect of intermediate pressing on the average value of the grain and colony thickness is relatively small (compare sample 1 and 3). But variations of grain and colony thickness for sample 3 are larger than for sample 1 indicating that the intermediate pressing has an effect of narrowing these parameters.

[13]Standard error $= \sigma/\sqrt{n-1}$, where n is the number of observations and the standard deviation (of each observation) $\sigma = (E(X^2) - (E(X))^2)^{1/2}$. Here $E(X)$ is the average grain thickness and $E(X^2)$ is the average squared grain thickness.

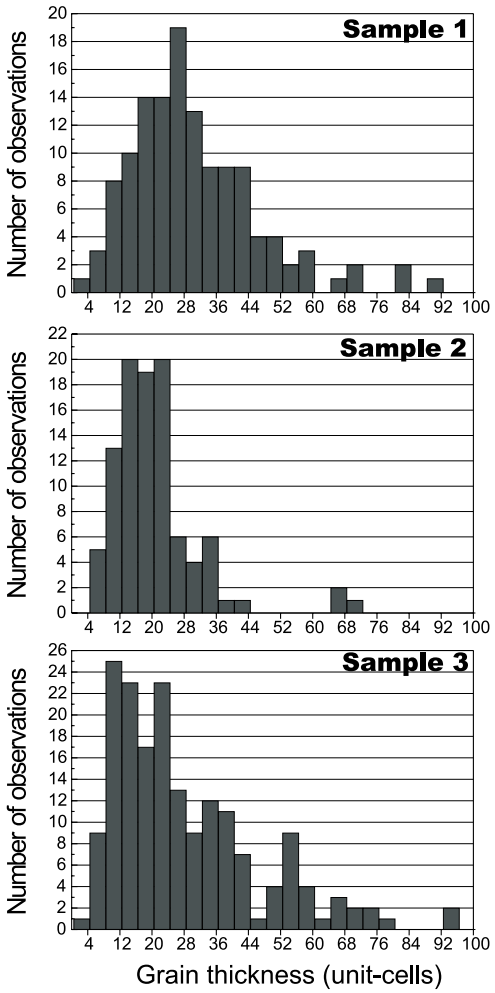

Figure 42. Histograms showing the distributions of grain thicknesses (in the c-axis direction). The number of observations is 128, 98 and 179 grains for sample 1–3, respectively.

4.8 Intergrowth

The Bi-2223 grains mainly consist of pure Bi-2223 ($n = 3$) unit-cells, but intergrowth of half unit-cells of other periodicities e.g. Bi-2212 ($n = 2$) and Bi-2234 ($n = 4$) is observed. The intergrowth content and distribution can be easily investigated by high-resolution TEM (HRTEM). Fig. 43, Fig. 44 and figure 5 Paper 4 show examples of intergrowth near twist boundaries. In Fig. 45 and Fig. 46 intergrowth near SCTILT boundaries can be seen. The distribution of half unit-cells (building units) in sample 1 and in sample 2 (cf. Table 1 in section 3.2) is summarized in Table 6. The intergrowth varied from 3% to 39% at different places in the sample. We have seen both small and high content of intergrowth near twist, SCTILT and ECTILT boundaries. It was often observed that there is intergrowth just next to a grain boundary. The total intergrowth in the fully processed tape (sample 1) as well as in sample 2 is about 15%. About 70% of the intergrowth in both tapes is Bi-2212 ($n = 2$). Almost all of the grain boundaries are free of non-superconducting phases. Only at one twist boundary in sample 2 we have found an intermediate amorphous phase.

Bi-2212 has $T_c \approx 85$ K (compared to $T_c \approx 110$ K for Bi-2223). This value of T_c is close to 77 K, therefore it could be possible that the intergrowth will lower the

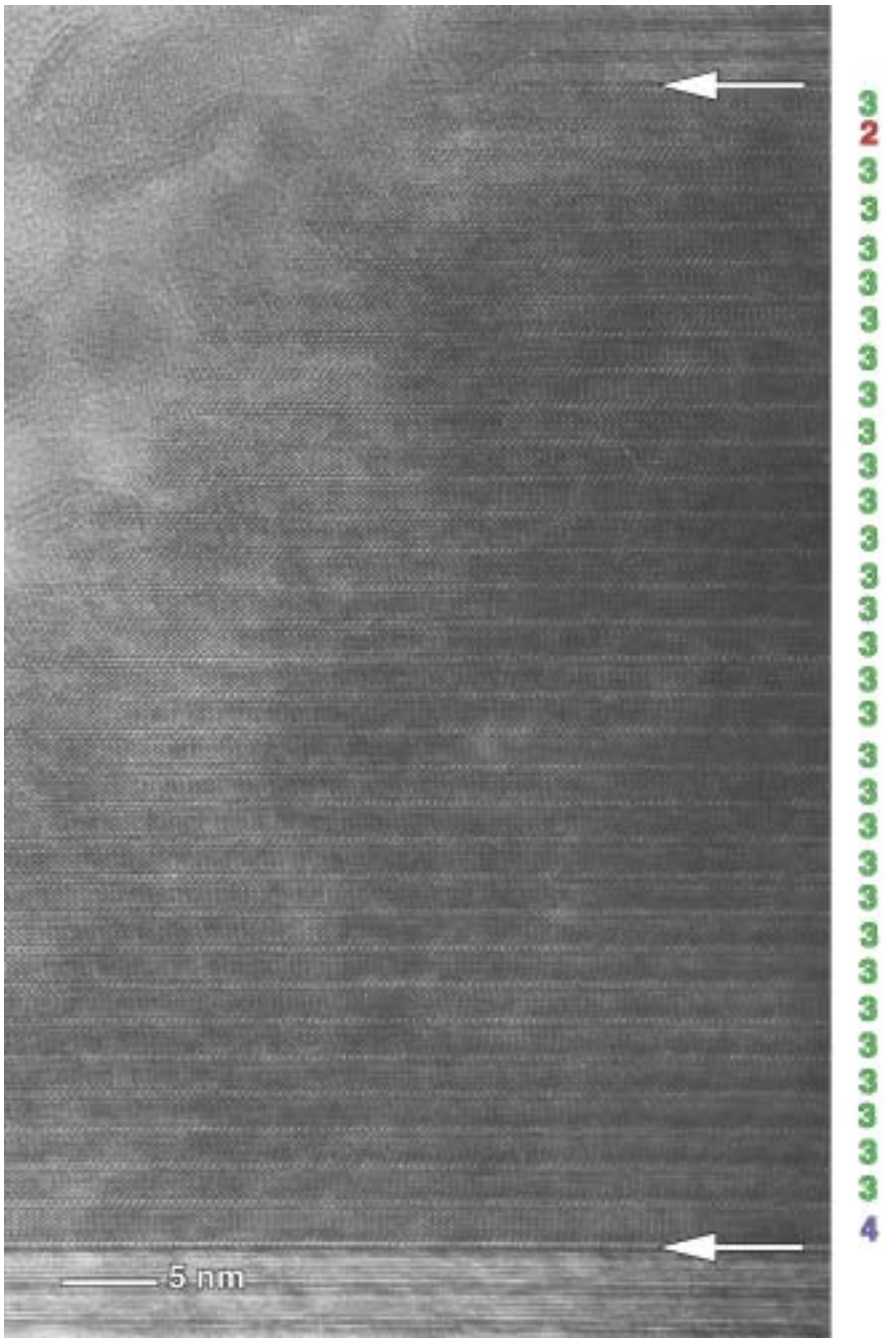

Figure 43. A high-resolution TEM image of a transversal cross-section of sample 1 showing a grain separated by two twist boundaries (marked by arrows). The grain is orientated along the [110] or the [010] direction. The numbers indicate half unit-cells of Bi-2223 (3) and intergrowth of Bi-2212 (2) and Bi-2234 (4).

critical current density J_c. But since the intergrowth content and distribution are the same in sample 1 (the fully processed tape) and sample 2 (the tape after 1st annealing), the intergrowth is not responsible for the lower J_c value (cf. Table 1 in section 3.2) in sample 2, as compared to the value of J_c in sample 1.

By means of synchrotron X-ray diffraction [8, 10], neutron diffraction [5] and Cu K_α XRD [52, 53] the fraction of Bi-2223 in fully processed tapes is measured to be as high as 98% [10]. All these techniques do not take intergrowth into account because the intergrowth domains are too small to be detected. The presented

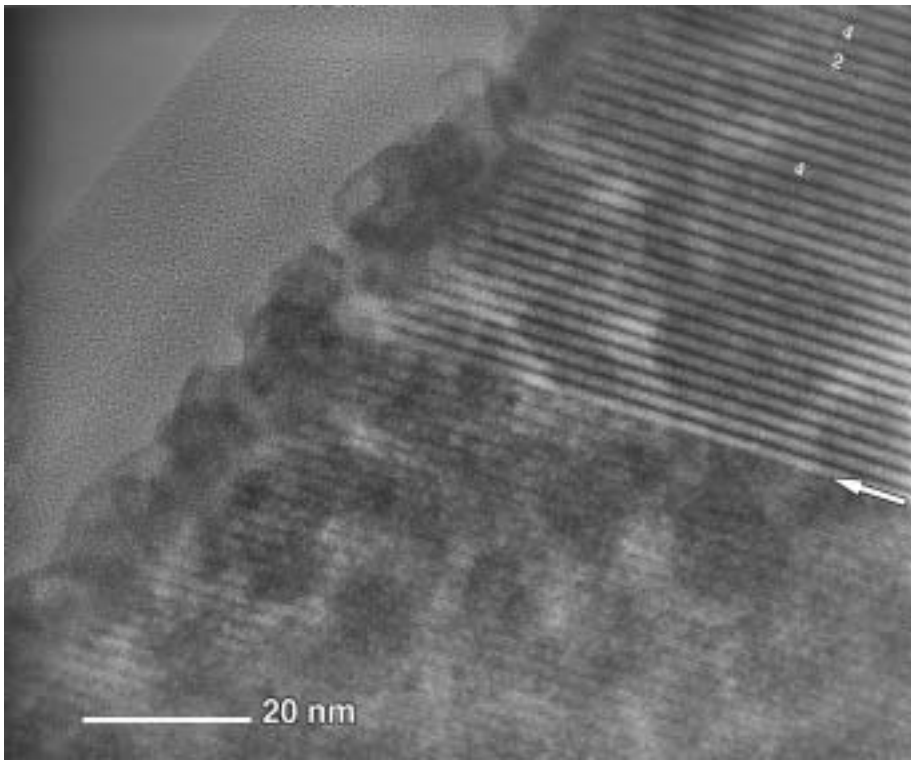

Figure 44. A high-resolution TEM image of a longitudinal cross-section of sample 1 showing two grains separated by a twist boundary (marked by an arrow). The lower grain is orientated along the [110] or the [010] direction. The numbers indicate intergrowth of Bi-2212 (2) and Bi-2234 (4). A close-up on a segment of the lower grain can be seen in Fig. 3.

$(Bi,Pb)_2Sr_2Ca_{n-1}Cu_nO_x$	Sample 1		Sample 2	
	Number of half unit-cells	%	Number of half unit-cells	%
$n = 3$	389		315	
Intergrowth				
$n = 2$	50	11	45	12
$n = 4$	17	4	20	5
$n = 5$	1	0.2	0	0
Total intergrowth		15		17

Table 6. The percentage of intergrowth in sample 1 and 2.

intergrowth results show that the content of intergrowth in the fully processed tape is 15%. This result is obtained near grain boundaries, but because the thickness of the grains is only 30 unit-cells, our result is general and the conversion into Bi-2223 is only about 83%.

According to Holsinger *et al.* [54] the Cu content in the Bi-2223 composition is a good measure for the presence of Bi-2212 intergrowth. This idea is based on previous studies by EDS in the TEM of intergrowth-free regions, which show only small variations in the Cu content in the solid solution region of Bi-2212 [55]. By EDS in the SEM the Bi-2223 compositions of sample 1–3 are investigated (Table 7).

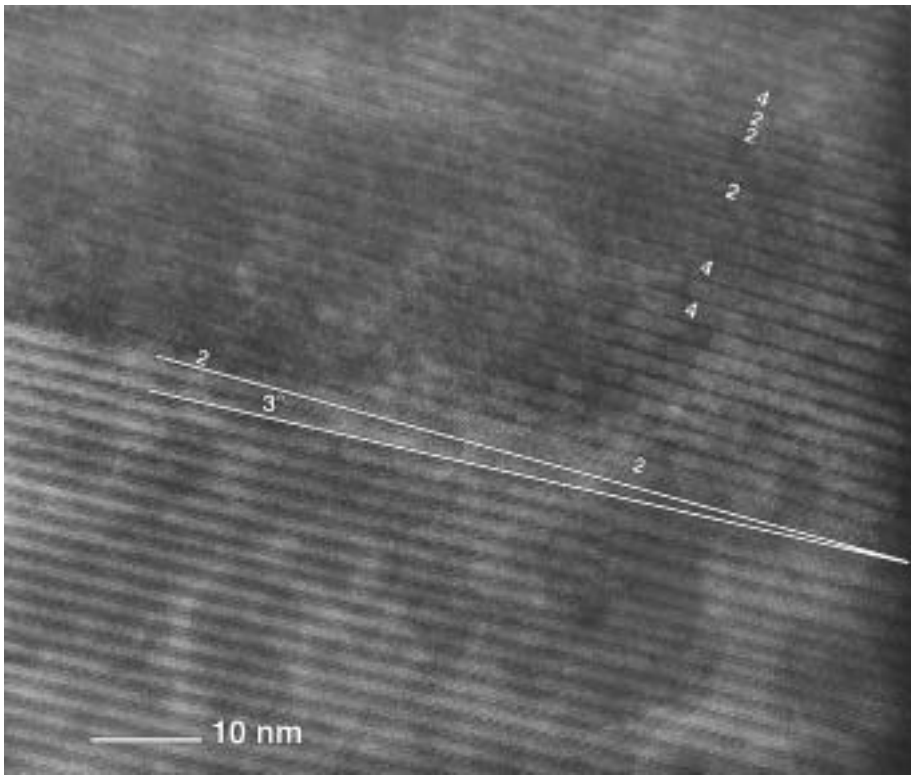

Figure 45. A high-resolution TEM image of a longitudinal cross-section of sample 1 showing two grains separated by a SCTILT boundary of 3°. The upper grain is orientated along the [110] or the [010] direction. The numbers indicate intergrowth of Bi-2212 (2) and Bi-2234 (4).

Based on the TEM intergrowth results, we should expect the Bi-2223 composition including the intergrowth to be: Cu $\approx$ 2.93 and Ca $\approx$ 1.93[14]. We observe that the Bi-2223 average composition found by EDS in the SEM of the fully processed tape (sample 1) is in good agreement with the intergrowth content and distribution found by TEM. In addition, the Cu content of Bi-2223 of sample 3 (the tape annealed for 200 h) indicates an intergrowth similar to sample 1. This is consistent with the observations by TEM that have indicated a constant intergrowth content during the tape processing (after the conversion into Bi-2223). Finally, the Cu content of Bi-2223 of sample 2 (cf. Table 7) is found to be 2.76. This value is not in agreement with that mentioned above. One might argue that the TEM study is not performed on representative grains in sample 2, but the low value of the Cu content corresponds to an intergrowth of 48% if an intergrowth-ratio Bi-2212/Bi-2234 of 3 is assumed. An intergrowth content of 48% is not reasonable. Therefore, this argument can be rejected. Another explanation is that since sample 2 contains smaller Bi-2223 colonies and most likely more secondary phases [48] than sample 1 and 3 it is possible that the resulting composition is not only that of Bi-2223 grains but also of secondary phases, since the sampling volume ($\sim$1 μm^3) is larger than the colony thickness (cf. Table 5). But this is in contradiction to the fact that secondary phases usually are Cu-rich or Pb-rich (note the low Pb content for sample 2). It is possible that the Bi-2223 phase actually contains less Cu after the 1st annealing since more Cu-rich secondary phases are present in the tape at this processing stage. To clarify this EDS investigations in the TEM are needed (with a sample holder that is not made of Cu), since the EDS in the TEM

[14]Cu: $0.04 \times 4 + 0.11 \times 2 + 0.85 \times 3 = 2.93$, Ca: $0.04 \times 3 + 0.11 \times 1 + 0.85 \times 2 = 1.93$.

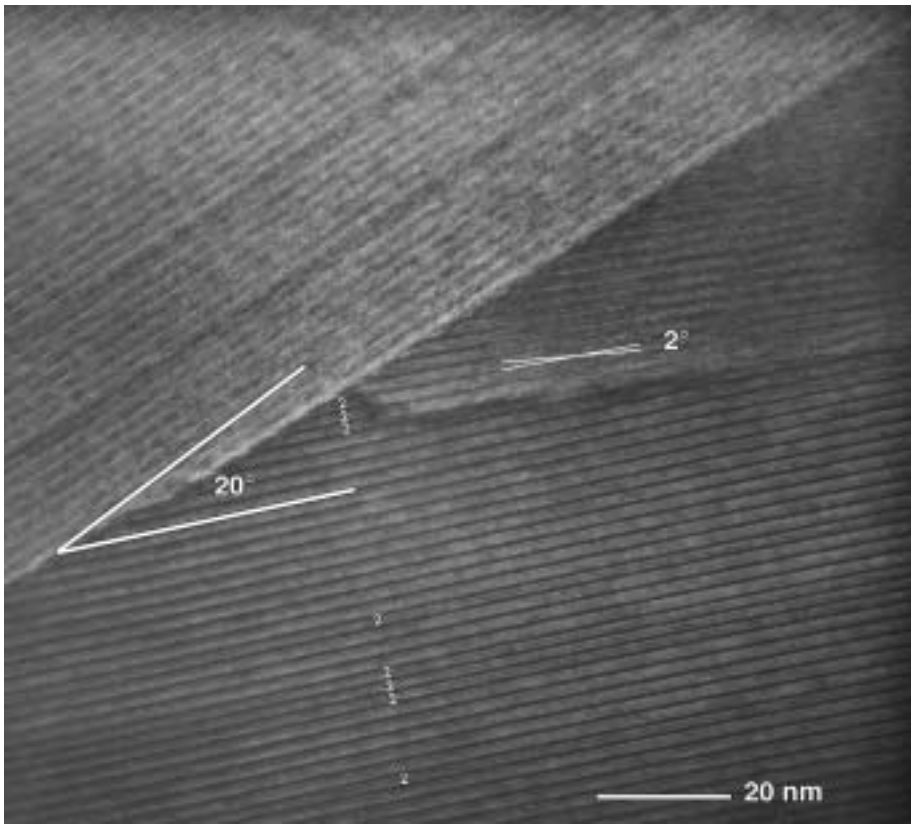

Figure 46. A high-resolution TEM image of a transversal cross-section of sample 1 showing two grains separated by a SCTILT boundary of 20° near a third grain. The number (2) indicates intergrowth of Bi-2212.

has a smaller sampling volume.

ID	Bi	Pb	Sr	Ca	Cu
Sample 1	2.00 ± 0.02	0.44 ± 0.02	1.70 ± 0.02	1.94 ± 0.02	2.93 ± 0.02
Sample 2	2.31 ± 0.04	0.28 ± 0.01	1.85 ± 0.02	1.80 ± 0.03	2.76 ± 0.03
Sample 3	1.99 ± 0.02	0.42 ± 0.02	1.65 ± 0.04	2.00 ± 0.02	2.94 ± 0.02

Table 7. EDS analysis in the SEM of the Bi-2223 composition. The composition (atom % × $\frac{9}{100}$) are found by averaging over 10, 10, and 12 different Bi-2223 areas in a transversal cross-section for sample 1–3, respectively.

5 Texture

This chapter contains texture results obtained from *in situ* synchrotron radiation experiments, room temperature synchrotron radiation measurements and angles of *c*-axis tilt grain boundaries measured by TEM imaging of differently processed tapes. In the end of the chapter a comparison of the synchrotron radiation and TEM result is placed.

5.1 Texture development

From the *in situ* synchrotron X-ray diffraction experiments the texture development can be investigated (cf. section 3.3.2). The texture evolution of a monofilamentary tape during the "1st" and "last" annealing in 8% O_2 is presented in section 5.1.1 and 5.1.2, respectively. In addition, in section 5.1.1 a comparison of these data with the texture results obtained from annealing in air (Paper 1) and with the texture results on a multi-filamentary tape using neutron diffraction performed by Fahr *et al.* [50] is found.

5.1.1 1st annealing in 8% O_2

In Fig. 47 the evolution of the average mis-alignment angle $\Delta\alpha$ of the *c*-axis (FWHM of the texture profile in α coordinates) for Bi-2212 and Bi-2223 is shown. The texture evolution is seen to take place primarily during the initial stage of the first heat treatment before the conversion into Bi-2223. After ∼7 h at the annealing temperature the $\Delta\alpha$ widths are identical of the two phases within the uncertainty. After ∼8 h the widths level off to $\Delta\alpha = 26° \pm 1°$. The Bi-2223 texture is observed to be constant during cooling.

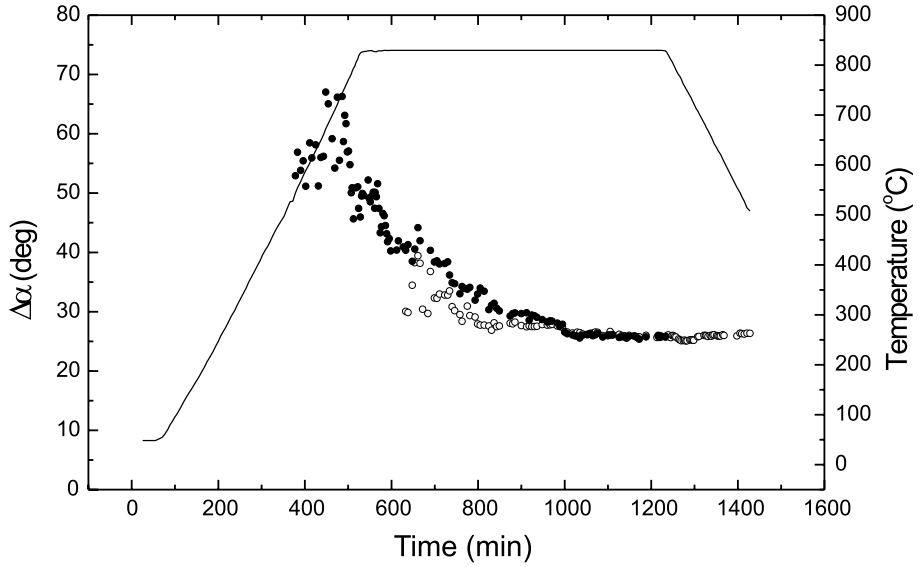

Figure 47. Texture evolution during the "1st annealing in 8% O_2". The FWHM of the texture profiles ($\Delta\alpha$) of the Bi-2212 (115) (•) and the Bi-2223 (117)(○). The line marks the temperature profile with reference to the temperature scale at the right-hand side.

The texture development obtained from annealing in air (figure 3 Paper 1) shows a similar evolution. In this case the $\Delta\alpha$ width levels off after ∼16 h at

the annealing temperature to a value of $\Delta\alpha = 23° \pm 1°$. The texturing in the annealing is approximately twice as slow as in the case of the annealing in 8% O_2. The comparison of the phase evolution showed (cf. section 4.2.1) a similar time difference.

The initial texture of Bi-2223 is seen to have a value of the $\Delta\alpha$ width similar to the final width. After the initial good texture the mis-alignment increases to the value of the Bi-2212 mis-alignment angle (figure 3 Paper 1 and Fig. 47). This result is demonstrated clearly in a later *in situ* study by Fahr *et al.* [50] using neutron diffraction on a multi-filamentary tape. Their texture results during a first annealing – after the annealing temperature of 825 °C is reached – in reduced oxygen are shown in Fig. 48 (note that they have plotted the texture degree). They find that after 7 h the texture evolution of Bi-2212 and Bi-2223 is the same and that the improvement of the texture saturates after 13 h. An explanation of the high texture degree of Bi-2223 in the beginning of the annealing is found by the authors using SEM/EDS analysis of a quenched sample after 2 h and 10 h annealing. The initial Bi-2223 grains appear only near the silver interface and here the colonies of grains are well aligned. During further annealing grains in the interior of the filament with worse texture also appear [50]. Since the multi-filamentary tape has a much higher amount of silver interfaces this texture effect is more clear in the multi-filamentary tape compared to the mono-filamentary tape.

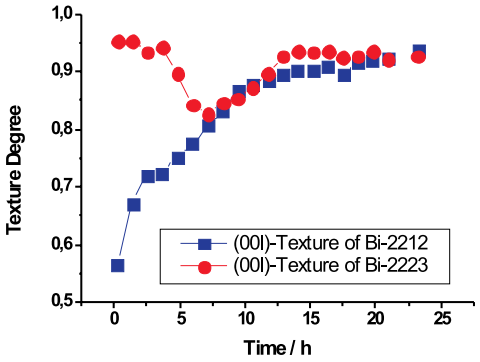

Figure 48. Development of textures of Bi-2212 and Bi-2223 in situ detected at 825 °C [50].

That the initial growth of Bi-2223 is near the silver interface may be due to the fact that the presence of silver lowers the melting temperatures and thereby increases the amount of liquid, which also is important for the texturing [31, 33]. The results of Fahr *et al.* [50] are in agreement of the previous results of Yi *et al.* [56], who also have found that the Bi-2223 phase always forms first (at lower temperatures) near the silver interface and that the Bi-2223 colonies align to the interface. In 1991 Yamada *et al.* [57] have also observed the better texturing near the interface. Lelovic *et al.* [58] have found that the Bi-2223 colonies near the silver sheath carry most of the current in the tape.

5.1.2 Last annealing in 8% O_2

The texture development as function of the annealing time (cf. section 4.3) of a mono-filamentary tape beforehand annealed in 8% O_2 and "fully" converted into Bi-2223 is shown in Fig. 49. The average grain mis-alignment is constant during this last annealing in 8% O_2 within the uncertainty. The $\Delta\alpha$ width is found to be $\Delta\alpha = 24° \pm 1°$, $\sim 2°$ lower than after the 1st annealing in 8% O_2.

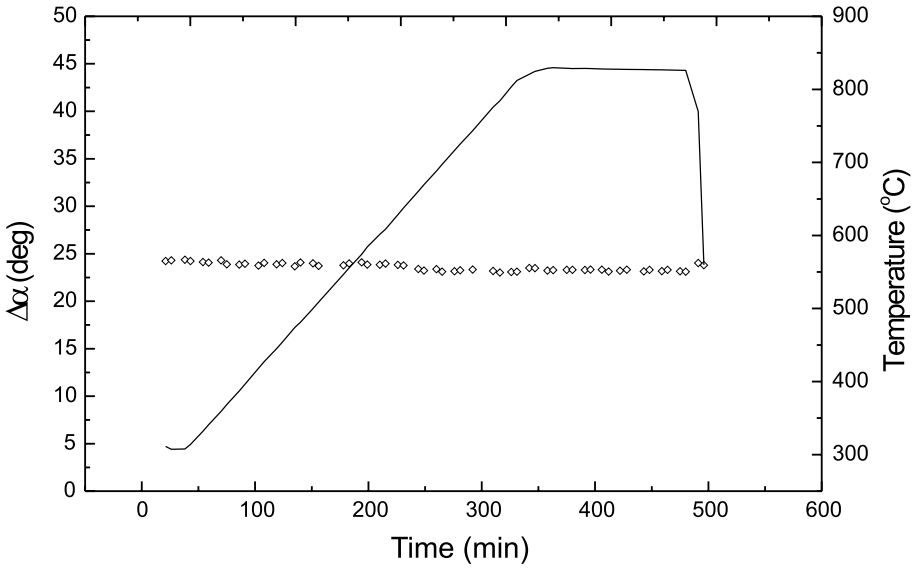

Figure 49. Texture evolution during the "last annealing in 8% O_2". The FWHM of the texture profile ($\Delta\alpha$) of the Bi-2223 (117)(○). The line marks the temperature profile with reference to the temperature scale at the right-hand side.

5.2 Final texture

The final texture is investigated in tapes with different process parameters (section 5.2.1) and with different numbers of filaments and initial pressings (section 5.2.2) by synchrotron X-ray diffraction.

5.2.1 Variation of processing

In Table 1 section 3.2 is shown the identification of five multi-filamentary tapes processed in different ways. The annealing steps were performed in 8% O_2. The texture of these five tapes has been investigated using synchrotron X-ray diffraction. In all cases the analysis is based on the 2223 (117) reflection. The texture results can be seen in Table 8.

One should expect that the fully processed tape (sample 1) and the almost fully processed tape quenched during the last annealing (sample 5) have an identical texturing. The results are 15.2° and 16.6° for sample 1 and 5, respectively. The almost fully processed tape stopped at 650 °C for 3 weeks (sample 4) has $\Delta\alpha = 15.6°$. This means that the average texture does not change during the 3 weeks. From sample 2 and 3 it seems that the texture degree is increased further, after the primary evolution, with the duration of the annealing. Sample 2 (< 50 h annealing) has $\Delta\alpha = 18.8°$ and Sample 3 (200 h annealing) has $\Delta\alpha = 13.7°$.

ID	Processing	$\Delta\alpha$ (deg)
Sample 1	Fully processed	15.2
Sample 2	1st annealing	18.8
Sample 3	200 h	13.7
Sample 4	3 weeks at 650 °C	15.6
Sample 5	Quenched during last annealing	16.6

Table 8. FWHM of synchrotron texture profiles ($\Delta\alpha$). More details of the processing can be seen in Table 1 section 3.2.

A check of the variations in the long length tape has been performed at three fully processed tapes (unfortunately the last annealing was performed in air instead of 8% O_2). The texture results are 17.3°, 17.1° and 17.1°. This shows none variation in the long length tape at the three places over ∼10 cm.

We have observed a better texturing in the multi-filamentary tape compared to the mono-filamentary tape. Since the multi-filamentary tape has a larger amount of silver interfaces this result is in agreement with the better texturing near the interfaces [50, 56, 57].

5.2.2 Variation of number of filaments

A study of the texture dependence of the filament thickness and the density has been performed on three tapes with an initial square geometry (instead of circular) with 37, 55 and 85 filaments, respectively[15]. The thickness of the filaments decreases with the number of filaments. The density is changed by pressing the green tapes with 0, 7.5 and 15 tons, respectively. After pressing, the tapes are annealed for 50 h at 828 °C in air (should have been in 8% O_2). The heating and cooling ramp was 100 °C/h. Due to the mistake of the surrounding atmosphere the conversion into Bi-2223 is only 55–60% (Table 9). At this conversion stage the texture evolution has maybe not leveled off yet. This may give a additional uncertainty of the synchrotron texture results shown in Table 10.

Conversion (%)	37 fila.	55 fila.	85 fila.
0 ton	55	57	58
7.5 tons	55	60	58
15 tons	57	56	58

Table 9. The percentage of conversion into Bi-2223 examined by the synchrotron X-ray diffraction.

$\Delta\alpha$ (deg)	37 fila.	55 fila.	85 fila.
0 ton	17.5	15.9	15.2
7.5 tons	17.9	17.4	16.5
15 tons	16.2	14.5	13.7

Table 10. FWHM of synchrotron texture profiles ($\Delta\alpha$) for tapes with different numbers of filaments and applied pressures before annealing.

We can observe a general trend showing that an increase in the number of filaments gives rise to a smaller mis-alignment angle ($\Delta\alpha$) and that the texture is best for pressing with 15 tons and worst for 7.5 tons. Again the result from different numbers of filaments is in agreement with the better texture near the silver interfaces [50, 56, 57] due to the 85-filamentary tape has thinner filaments and thereby a larger amount of interfaces.

A better texture for thinner filaments and the improvement during further annealing (cf. section 5.2.1) is in agreement with a model where the texture evolution is determined by continued nucleation and two-dimensional grain growth in the confined volume given by the filament thickness [60].

[15]These tapes are produced by the Department of Manufacturing Engineering (IPT) at the Technical University of Denmark (DTU). More homogeneous tapes are obtained by this geometry after flat rolling [59].

As the three tapes have the same dimensions we should expect that the critical current is highest for the 85-filamentary tape, since this tape contains the thinnest filaments and has a higher silver interface area with a texture well aligned to the interface [56]. For tapes after 1st annealing of the 37, 55 and 85-filamentary tape the critical current values are shown to be almost equal. This could be the result of the fact that the thin filaments are not always lying flat.

5.3 Angles of *c*-axis tilt

By TEM the angles of *c*-axis tilt grain boundaries (cf. Fig. 8 and Fig. 9) are measured in sample 1–3. The results and a discussion are found in **Paper 4**. The results are summarized in this section.

The grain boundaries have been examined both in longitudinal cross-section and in transversal cross-section. In the two different directions the *c*-tilt angles have been found to produce the same distribution. Furthermore, the two different *c*-tilt angles (SCTILT and ECTILT) have also the same distribution. Therefore, all the *c*-tilt angles are plotted in the same graph (Fig. 50). The average *c*-tilt angle is found to be 14.4° ± 1.3° in sample 1 (Table 11). The peak maximum is at 7°–9°. The highest observed angle is 41°. Sample 2 has a wider distribution with a lot of large-angle *c*-tilt boundaries up to 90° besides similar small angles as in sample 1. The average *c*-tilt angle is found to be 26.0° ± 1.7°. A comparison between sample 1 and 2 indicates that the pressing and further annealing removes the highest *c*-tilt angles from the tape. In sample 3 the average *c*-tilt angle is found to be 18.6° ± 1.7°. The peak maximum is at 7°–12°. If the four observations with highest *c*-tilt values are removed the average value becomes 16.1° ± 1.2°. The distribution for sample 3 is within the statistical uncertainty similar to the distribution for sample 1. This suggests that further annealing without pressing in between should also provide grain boundaries with lower *c*-tilt values.

ID	Annealing	Average *c*-tilt angle (deg)
Sample 1	75 h (total), pressing	14.4 ± 1.3
Sample 2	<50 h	26.0 ± 1.7
Sample 3	200 h	18.6 ± 1.7

Table 11. The average values of c-tilt angle observed by TEM for sample 1–3.

The I_c values of sample 1 and 3 are 44 A and 22 A, respectively, even though the two samples have similar average values of *c*-tilt angle and grain thickness. Thus, other parameters are also important current limiting factors. In sample 3 we have observed that an amorphous phase between grains is present or quickly forms in the electron beam, indicating a bad grain connectivity. Using the SEM, a low density is observed in sample 3 (this sample contains a large amount of elongated holes). These observations of the grain connectivity and the density can explain the low I_c value of sample 3. Obviously, the intermediate pressing densifies the structure efficiently.

5.4 Comparison of TEM and synchrotron results

The synchrotron texture results and the TEM angle of *c*-axis tilt results are not directly comparable. By the synchrotron X-ray technique we examine the FWHM of the texture distribution related to the three dimensional *c*-axis mis-alignment

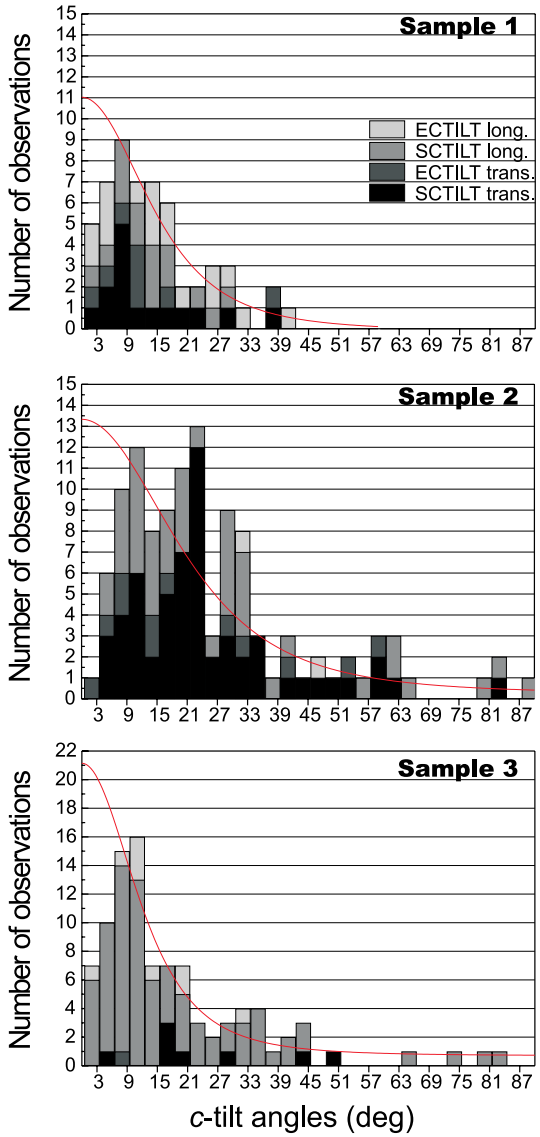

Figure 50. Histograms showing the distributions of c-tilt angles of SCTILT and ECTILT boundaries. "long." and "trans." refer to the longitudinal cross-section direction and the transversal cross-section direction, respectively. The number of observations is 55, 115 and 96 angles for sample 1–3, respectively. The line is a squared Lorentz fit with the midpoint fixed to zero to the data set truncated by the first two columns.

with respect to the tape normal[16]. The TEM results are an average value of a projection of the *c*-axis tilt angles between two connected grains. If we assume that the colonies grow independently of each other we could in principle by mathematical treatments relate these two differently ways of expressing the texture. It will not be done in this thesis.

By fitting the distributions of *c*-tilt angles (Fig. 50) to a squared Lorentz distribution with the midpoint fixed to zero we can compare the trend of the results obtained by TEM and the synchrotron. The fitting results are shown in Fig. 50. The data set has been truncated by the first two columns since these numbers of observations could be too low because boundaries with angles lower than 6°

[16]Note that in the case of a tape with the grains "lying in slalom" the synchrotron result is higher than the "current meeting" grain mis-alignment.

will not be observed at images recorded at low magnifications. The fit of especially sample 2 does not look good, but it is mainly due to binning of the data. The FWHM results of the squared Lorentz curves are listed together with the synchrotron FWHM results in Table 12. By comparing the results we observe a similar trend in the data. The factor of ∼2 between the synchrotron and TEM results seems reasonable, since we expect a value between 1 and 2. In the case of the two connecting grains lying "around a plane parallel to the tape plane" the angle in the 2D plane measured by TEM is equal to the sum of the two angles measured by the synchrotron.

ID	Synchrotron $\Delta\alpha$ (deg)	TEM FWHM (deg)
Sample 1	15.2	29.7
Sample 2	18.8	41.9
Sample 3	13.7	24.3

Table 12. FWHM results.

It is worth noting that due to the variation of the texture throughout the filament [57] it is necessary to investigate a huge number of grain boundaries by TEM to ensure a representative data set. This problem does not exist in the synchrotron results since these are obtained from an averaging over the tape width.

6 Cooling

Since secondary phases form during the cooling ramp down to room temperature this part of the annealing has been examined more thoroughly. An investigation of the cooling behavior in air by *in situ* synchrotron X-ray diffraction is placed in section 6.1. The results from an optimization experiment using different "two-step" temperature profiles for the last annealing in 8% O_2 in order to improve the critical current density are presented. For further analysis of the cooling behavior the decomposition mechanism is studied in 8% O_2 in section 6.3.

6.1 *In situ* cooling behavior

During the analysis of the *in situ* synchrotron X-ray diffraction results presented in Paper 1 and Paper 2 the emphasis has been placed on the structural changes taking place during the thermal treatment in air prior to the cooling. In **Paper 3** the phase transformations taking place during the cooling of the heat treatments presented in Paper 1 (Tape A) and Paper 2 (Tape B) are investigated. A summary of the results and the cooling model are placed in this section.

Tape A was cooled at a constant rate of 50 °C/h. In Fig. 51 is shown the concentration variations of the majority phases during the cooling. In addition, a small amount of Bi-2201 forms during cooling. At temperatures above 730 °C the $(Ca,Sr)_2CuO_3$ (and the liquid) is transformed into Bi-2212 and Bi-2223. Below 780 °C the 3221 phase or $(Ca,Sr)_2PbO_4$ appears. Finally, we observe that the Bi-2223 concentration decreases from 93% to 75% between 730 °C and 600 °C. Below 780 °C a smaller shift – than predicted by thermal contraction – of the diffraction peaks (cf. figure 4 Paper 3) for Bi-2223 indicates a change in stoichiometry, which can be due to Pb leaving Bi-2223, simultaneously with the growth of 3221 or $(Ca,Sr)_2PbO_4$. The Bi-2212 stoichiometry is seen to be constant during the cooling.

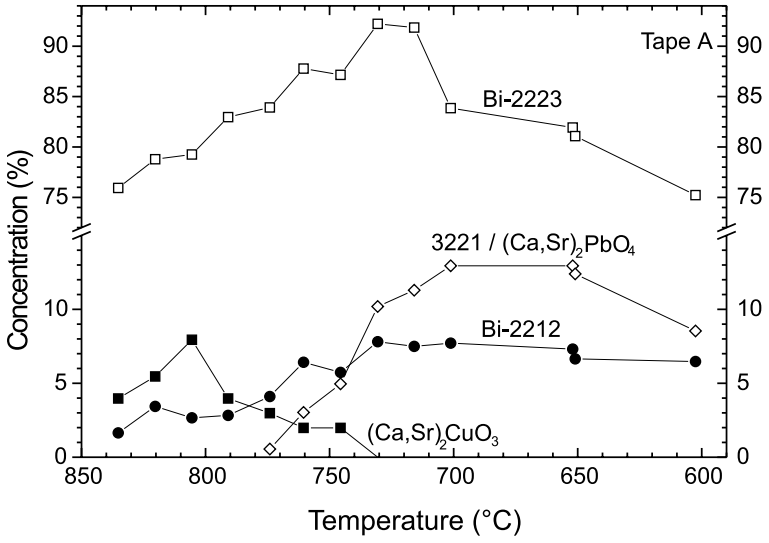

Figure 51. The concentration variations of Bi-2212 (115) (•), Bi-2223 (115) (□) and $(Ca,Sr)_2CuO_3$ (011) (■) during cooling of Tape A. In addition, the concentration of a Pb rich phase (◇) is plotted. This may be either $(Ca,Sr)_2PbO_4$ or 3221 – with nearly identical XRD spectra. The concentration values shown relate to $(Ca,Sr)_2PbO_4$. Data points are identical to the ones presented in figure 2 Paper 1.

Tape B was cooled from 860 °C by means of sequential quenches to the intermediate temperatures at 845 °C, 820 °C and 660 °C. The concentration changes of the majority phases the during cooling are shown in Fig. 52. $(Ca,Sr)_2CuO_3$ and the liquid phase are seen to fade simultaneously. These two phases are primarily transformed into Bi-2223 + Bi-2212, Bi-2212 and Bi-2201, after the quenches to 845 °C, 820 °C and 660 °C, respectively. At 660 °C the 3221 phase or $(Ca,Sr)_2PbO_4$ forms. At the same time the Bi-2223 concentration decreases (from 40% to 35%). The kinetics of these two events is found to be similar, and much slower than the liquid solidification and formation of Bi-2201. From the diffraction peak shifts (cf. figure 6 Paper 3) we observe that the stoichiometry of Bi-2223 is constant until the 3221 phase or $(Ca,Sr)_2PbO_4$ appears (analogous to Tape A), following the quench to 660 °C. Furthermore, below 820 °C the Bi-2212 phase does not change stoichiometry, in accordance with the results for Tape A.

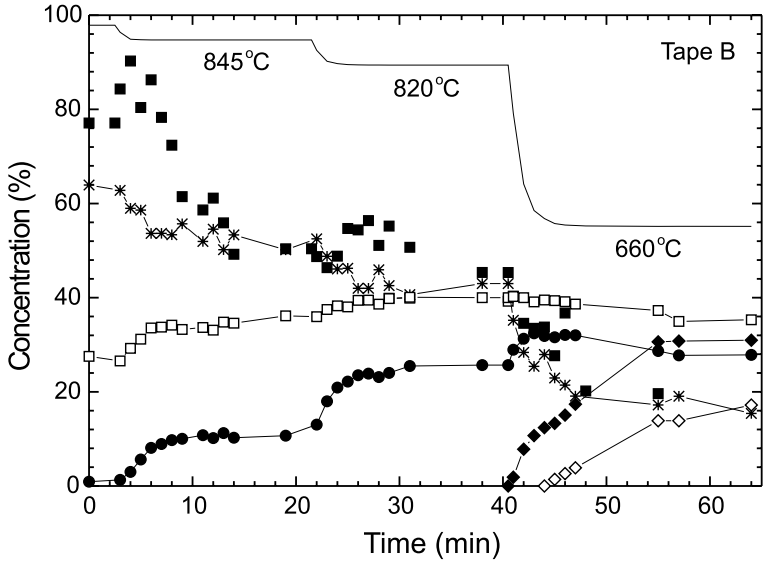

Figure 52. The concentration of the different phases during the cooling of Tape B as function of the cooling time. The symbols refer to: (•) Bi-2212 (115), (□) Bi-2223 (115), (■) $(Ca,Sr)_2CuO_3$, (∗) liquid and (⧫) Bi-2201. In addition, the concentration of a Pb rich phase (◇) is plotted. This may be either $(Ca,Sr)_2PbO_4$ or 3221 - with nearly identical XRD spectra. The concentration values shown relate to $(Ca,Sr)_2PbO_4$. The temperature profile is overlaid as a solid line. Data points are identical to the ones presented in Fig. 37 or figure 5 Paper 2. Additionally, the Bi-2201 phase and $(Ca,Sr)_2PbO_4$ or 3221 are included.

The observations for the two tapes are consistent with the following model:
Precipitation: Above a certain temperature T_1, $(Ca,Sr)_2CuO_3$ and the liquid transform to Bi-2212 + Bi-2223. Within the Bi-2223 single-phase regime, Bi-2212 may in turn be converted to Bi-2223. Below T_1 $(Ca,Sr)_2CuO_3$ and the liquid mainly transform to Bi-2201. From the combination of the two experiments we can conclude that 660 °C $< T_1 \leq$ 750 °C. Upon the change of the temperature from 820 °C to 660 °C the precipitation seems to encompass both fast (∼1 min) and slow reactions.
Bi-2223 Decomposition: Below a certain temperature T_2, Bi-2223 decomposes to form 3221 or $(Ca,Sr)_2PbO_4$. From Tape A: $T_2 \approx$ 780 °C. In connection with this the average Bi-2223 stoichiometry is changed, most likely due to the Pb-rich grains becoming unstable first. The reaction is rather slow: at 660 °C it is 0.6% of Bi-2223 per minute.

We may compare these results with the phase diagrams, such as the one established by Majewski *et al.* [61]. Such diagrams relate to pressed pellets under equilibrium conditions and with minor differences in the nominal stoichiometry of the precursor powder. Nevertheless, values for T_1 (735 °C) and T_2 ($T_2 > 750$ °C, depending on Pb stoichiometry) correspond reasonably well. In Ref. [61] it is shown that the Pb solubility of Bi-2223 has a maximum at 850 °C and that the Bi-2223 phase contains almost no Pb at ∼750 °C. Since no silver is present in the pressed pellets these temperatures are higher than in the case of silver clad tapes [31]. Our observations of the change in the Bi-2223 stoichiometry during cooling are in agreement with the temperature dependent Pb solubility.

Wang *et al.* have investigated the effects of the Bi-2201 and 3221 phases on J_c [62, 63]. During a post annealing at 780 °C, 3221 was formed in fully reacted tapes at an approximate rate of 1% per hour, while the Bi-2212 concentration remained constant [63]. The 3221 phase assembled in larger grains, some of them situated at grain boundaries, with detrimental effect on J_c as a result. Bi-2201 on the other hand was present in tapes quenched from high temperatures, but vanished after prolonged heating at 820 °C [62]. Work on pressed pellets has also demonstrated the formation of the 3221 phase in the range between 500 °C and 800 °C [64, 65] (also consistent with the phase diagram in 8% O_2 shown in Fig. 25). Finally, we note that during the slow heating of Tape B a 3221 phase was also present. It disappeared at 789 °C (cf. section 4.5 or Paper 2).

The model described above is in agreement with all these observations – provided that the low temperature phase is 3221 and not $(Ca,Sr)_2PbO_4$.

Note that the data from both "1st annealing in 8% O_2" (cf. Fig. 30) with a cooling rate of 100 °C/h and the "last annealing in 8% O_2" (cf. Fig. 33) with "furnace" cooling indicates no stoichiometry changes of Bi-2223 in contrast to the two just presented thermal treatments in air.

6.2 Two-step cooling

The multi-filamentary tape already annealed (cf. section 3.2) are investigated during cooling in 8% O_2. Different two-step temperature profiles are used for the final heat treatment (cf. Fig. 53). The temperature of the second step and the two cooling rates are systematically varied. The tapes are characterized by means of transport measurements (I_c) and by SEM. The phase assembly, after the cooling procedure, is investigated by means of synchrotron X-ray diffraction.

In Fig. 53 the two-step temperature profiles are shown. The annealing time for the second stage is chosen to 30 h to obtain a sufficient time for a conversion. Fig. 54 shows the results in the shape of the critical current versus the temperature of the second stage. The four curves refer to different cooling rates (ramp 1 and 2 in Fig. 53). We observe that the optimal annealing temperature for the second stage is around 800 °C, and that this result is independent of the cooling rates of ramp 1 and 2. The second stage temperature has to be low enough to complete a precipitation of the liquid phase but on the other hand not so low that secondary phases arise. The optimum value is 44 ± 0.7 A and obtained for ramp 1 = 5 °C/h and ramp 2 = 150 °C/h ((5,150) in Fig. 54). Our interpretation of these observations is that a slow rate to 800 °C provides time for precipitation of the liquid used as mass transport when forming the superconducting phase Bi-2223. The last rate has to be fast to reduce secondary phases (but not so fast that micro-cracks arise). We also observe that when the first cooling rate is slow, the temperature of the second stage is less important (between 800 °C and 700 °C). Fig. 54 includes data from tapes quenched at ramp 2. For second stage temperatures at 830 °C and 600 °C the critical current is as high as for the non-quenched tapes. In between

these temperatures the critical current is lower for quenched tapes. These results are consistent with those from previous experiments produced by Dou *et al.* [52] and Liu *et al.* [66].

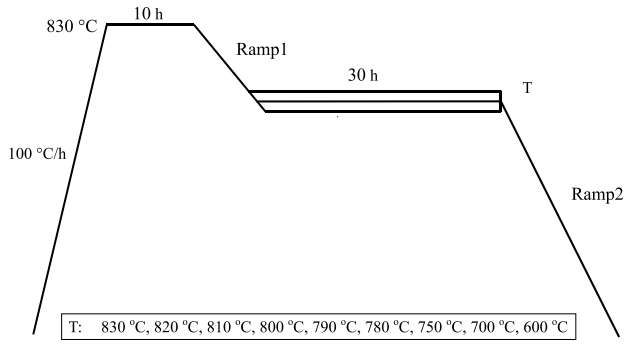

Figure 53. The two-step temperature profiles. The heating rate is 100 °C/h to the annealing temperature 830 °C. After 10 h at this temperature the tapes are cooled, with a rate of 5 °C/h or 30 °C/h, to different temperatures T and left there for 30 h. Finally, the tapes are either cooled to room temperature with a rate of 30 °C/h or 150 °C/h or quenched to room temperature.

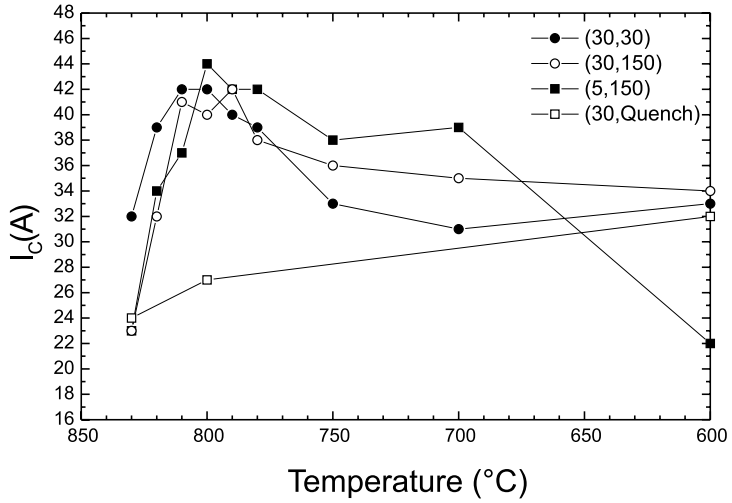

Figure 54. The critical current versus the temperature T of the second stage for four combinations of cooling rates at ramp 1 and 2, cf. Fig. 53. (30,150) refers to Ramp 1 = 30 °C/h and Ramp 2 = 150 °C/h etc. Each data point is obtained by averaging I_c results for the best three tapes out of four.

In Table 13 results obtained from X-ray diffraction patterns (as shown in Fig. 55) are listed. The intensity development of the secondary phases Ca_2CuO_3, 3221 and 3222 corresponding to three diffraction rings is studied. By means of EDS (energy dispersive X-ray analysis) in the SEM the stoichiometry of the 3222 phase is verified to be approximately $(Bi_2Pb)Sr_2Ca_2Cu_2$. Hence, the lead amount is twice that of the superconducting phase Bi-2223. The 3221 phase is Pb-rich (approximately $(BiPb_2)Sr_2Ca_2Cu$). The 3222 and the 3221 phases have the same *d* spacing. In the diffraction image the 3221 ring is dotted, indicating that the 3221 particles are larger than the 3222 particles. The Pb-rich phase 3221 appears at ∼800 °C. From ∼700 °C we observe instead the Bi-rich phase 3222. Ca_2CuO_3 is present at high (∼830 °C) and low (∼600 °C) temperatures.

(30,30)	3222	3221	CCO
d	4.95	4.95	3.17
Temp		(dots)	
830			X
820			
810			
800		X	
790		**X**	
780		X	
750		**X**	
700	X		
600	(X)		**X**

(30,150)	3222	3221	CCO
d	4.95	4.95	3.17
Temp		(dots)	
830			
820			
810		(X)	
800		X	
790		X	(X)
780		X	
750		**X**	
700	X		
600	X		

(5,150)	3222	3221	CCO
d	4.95	4.95	3.17
Temp		(dots)	
820			(X)
810			
800		X	
790		X	
780		X	
750		**X**	X
700		X	
600		X	**X**

(30,Quench)	3222	3221	CCO
d	4.95	4.95	3.17
Temp		(dots)	
830			X
800		X	
600	X	X	**X**

*Table 13. Phase appearance as determined from three X-ray diffraction rings corresponding to 3222, 3221 and Ca_2CuO_3 (CCO) for the four combinations of cooling rates. 'X' symbolizes the presence of the phase at the given temperature. '**X**' symbolizes a maximum in intensity and '(X)' a low intensity. 'd' is in (Å) and 'Temp' in (°C).*

From the data series (30,30) three tapes annealed with the second stage temperature at 600 °C, 800 °C and 830 °C, respectively, are selected for a compositional analysis of Bi-2223 and an examination of secondary phases using EDS in the SEM. The corresponding average critical current values (I_c) are 33 ± 1.8 A, 42 ± 0.6 A and 32 ± 0.5 A for T = 600 °C, 800 °C and 830 °C, respectively.

The average values of the atom % ratios: Bi/Pb, Sr/Ca, Cu/Sr and Cu/Bi of Bi-2223 from different areas are shown in Table 14. Within the uncertainty the Bi/Pb content seems to be the same in all three tapes or perhaps a little higher for T = 800 °C, which is the tape with the highest I_c value. The Pb amount in Bi-2223 was found to be the same in filaments at the center and the edge of the tape. For T = 800 °C the Cu/Bi amount is larger than for the two other temperatures. We can conclude that the Bi-2223 composition of the three tapes is almost identical. Note that the composition of Bi-2223 varies in the filament. Holesinger *et al.* [54, 67] have investigated the spatial variations of the Bi-2223 composition by EDS in the TEM. They have observed a depression of the lead content of the Bi-2223 phase in the vicinity of secondary phases. The average composition of Bi-2223 was found to be $Bi_{1.83}Pb_{0.28}Sr_{1.98}Ca_{1.93}Cu_{2.97}O_y$ away from secondary phases, $Bi_{1.92}Pb_{0.17}Sr_{1.93}Ca_{2.01}Cu_{2.98}O_y$ near the Pb-rich 3221 phase and $Bi_{1.88}Pb_{0.13}Sr_{1.87}Ca_{2.11}Cu_{3.02}O_y$ near 2:1 [54].

A backscattered SEM image for T = 600 °C is shown in Fig. 56. Another example showing two filaments from the center of the tape with T = 800 °C can

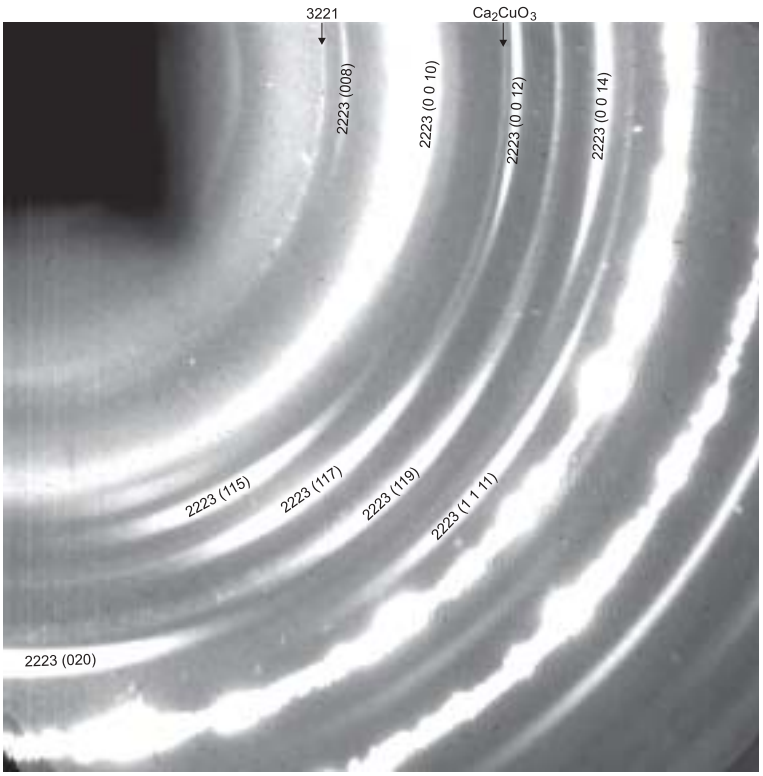

Figure 55. A raw image acquired by synchrotron X-ray diffraction on a tape annealed with a second stage temperature at 600 °C and ramp parameters: (5,150).

	Bi/Pb	Sr/Ca	Cu/Sr	Cu/Bi
600 °C	4.61 ± 0.28	0.98 ± 0.01	1.54 ± 0.04	1.35 ± 0.02
800 °C	5.08 ± 0.18	1.01 ± 0.01	1.52 ± 0.01	1.41 ± 0.00
830 °C	4.72 ± 0.19	1.00 ± 0.01	1.49 ± 0.01	1.35 ± 0.02

Table 14. Compositional analysis by EDS of Bi-2223 in tapes annealed with a second stage temperature of 600 °C, 800 °C and 830 °C, respectively. The values are obtained by averaging over 8, 9, and 13 data points for 600 °C, 800 °C and 830 °C, respectively.

be seen in Fig. 19. For T = 600 °C a larger amount of Pb-rich phases has been observed. One could think that since these particles usually are small and thin they will not limit the current significantly. But from the observations by e.g. Holesinger *et al.* it is known that the secondary phases disrupt the structure in a larger area than their physical size since the Bi-2223 contains less lead next to secondary phases [54].

Finally, the CuO (and Ca_2CuO_3) content has been investigated both in filaments at the center and the edge of the tape. The results are listed in Table 15. The observed CuO particles have a size of ∼1–100 μm^2. The average particle size in the center filaments is 18, 14 and 6 μm^2 for 600 °C, 800 °C and 830 °C, respectively, and 9, 6 and 8 μm^2 in the edge filaments[17]. From Table 15 we observe that a second stage annealing at 600 °C results in a higher content of CuO (in forms of larger particles) in both the center and edge filaments (2.7% CuO in the center filaments). In addition, we observe that for 830 °C the center filaments contain more but smaller CuO particles than for 600 °C.

[17] In the edge filaments for 800 °C and 830 °C an additional amount of very small CuO particles is possibly present.

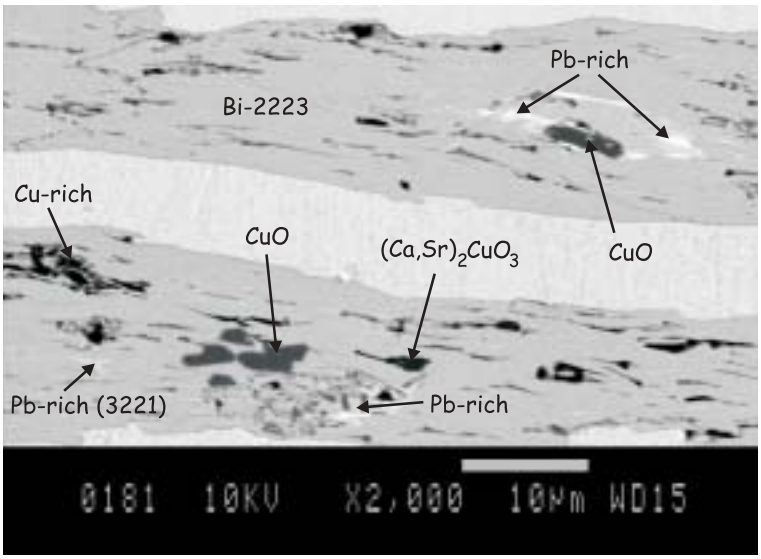

Figure 56. A backscattered SEM image for $T = 600\,^{\circ}C$. In the image a transversal cross-section of two pieces of filaments from the center can be seen.

CuO	Center		Edge	
	Number of particles	Content (%)	Number of particles	Content (%)
600 °C	22	2.7	10	1.0
800 °C	16	1.5	4	0.3
830 °C	31	1.2	6	0.6

Table 15. CuO (and Ca_2CuO_3) content in a transversal cross-section found by backscattered SEM imaging. The percentage of the CuO content is in the center an average using five filaments ($\sim 15 \cdot 10^3 \mu m^2$) and in the edge two filaments ($\sim 8 \cdot 10^3 \mu m^2$).

6.3 Decomposition

For further analysis of the cooling part a decomposition measurement is performed in 8% O_2. When 650 °C is reached on the way down to room temperature for the last annealing, the tapes are left at this temperature for different times before quenching. The annealing time varies from 0 h to 3 weeks (0, 1, 2, 3 and 6 h, 1, 2, 3, 4 and 7 days, 1, 2 and 3 weeks). The critical current values as function of the annealing time at 650 °C are shown in Fig. 57. After 3 weeks the current has decreased from 42 A to 22 A.

The phases present are investigated by means of (room temperature) synchrotron X-ray diffraction. A 2θ projection for the tape quenched after 7 days at 650 °C is shown in Fig. 58. Only the Bi-2223 phase and a reflection at $d = 4.95$ Å corresponding to 3222 are observed. In Fig. 59 the phase evolution is shown. The integrated intensity of the reflection corresponding to the secondary phase 3222 increases as function of the annealing time, but seems to saturate.

Based on the shape of the integrated intensity curve for the Bi-2223 phase (Fig. 59) and the critical current values in Fig. 57, we can conclude that the decomposition is very slow.

It should be mentioned that the experiment was initially performed up to 7 days annealing and later on increased to 3 weeks due to a slower decomposition than ex-

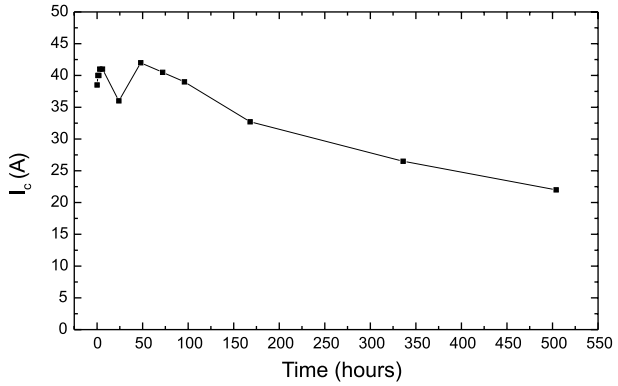

Figure 57. The critical current versus the annealing time at 650 °C before quenching to room temperature.

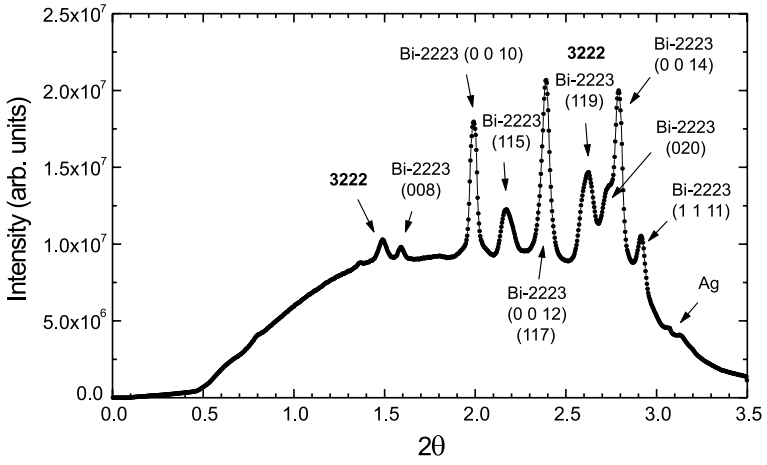

Figure 58. A 2θ projection of the normalized 2D image recorded for the tape quenched after 7 days at 650 °C. The silver peaks were screened by a lead disk since their high intensity could damage the image plate.

pected. The data from the first synchrotron radiation measurement (up to 7 days) has shown a high Ca_2CuO_3 amount (reflection at $d = 3.17$ Å), just as the temperature reaches 650 °C, which afterwards decreases to a constant value[18].

By EDS in the SEM the composition of 3222 is found to be $Bi_{1.6}Pb_{1.4}Sr_2Ca_2Cu_2$ in the tape annealed for 3 weeks (Sample 4). At this stage the 3222 phase covers 6% – in form of a lot of small particles (< 1 μm^2) – of the 3222 + Bi-2223 area in the 2D transversal cross-section. In addition, a lot of small Cu-rich particles of ~ 1 μm^2 with the average stoichiometry of 1117 have been observed. Furthermore, big CuO particles (up to 100 μm^2) are present partly in the silver next to the filament interface and partly in the interior of the filaments.

The Bi-2223 composition is investigated using EDS in the SEM. The tapes annealed for 3 h, 7 days and 3 weeks at 650 °C, respectively are selected. In Table 16 the compositions found by averaging over 10 different Bi-2223 areas in the transversal cross-section are shown. We observe a 40% loss of Pb in the Bi-2223 phase during the annealing time from 3 h to 3 weeks. Furthermore, we observe that during the first week of annealing nearly no change in the Pb content takes place, indicating a very slow reaction.

[18]The data from the first measurement was recorded by a CCD camera protected by lead (resulting in a smaller background) and not the image plate as the data from the later measurement including all tapes.

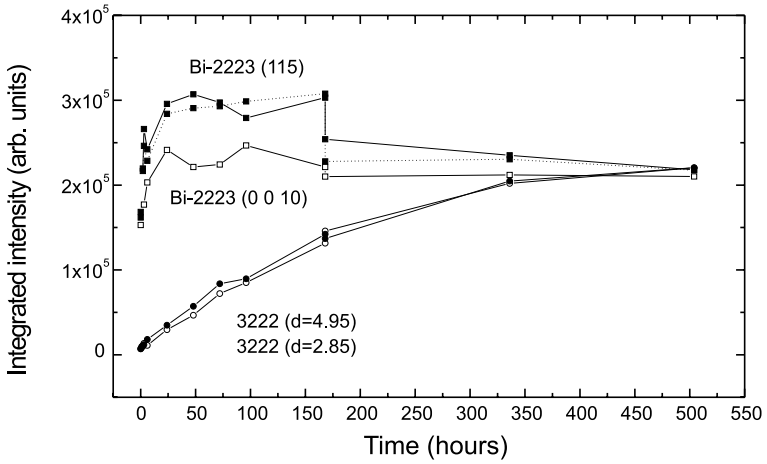

Figure 59. The integrated intensity (in arb. units) for the Bi-2223 and the 3222 phase as function of the annealing time at 650 °C before quenching to room temperature. The symbols refer to: (···■···) Bi-2223 (115) fitted alone by a squared Lorentzian, (■) Bi-2223 (115) fitted together with Bi-2223 (0 0 10) by two squared Lorentzians, (□) Bi-2223 (0 0 10), (•) 3222 (d = 4.95 Å) and (○) 3222 (d = 2.85 Å). Unfortunately, an injection took place between "7 days" and "1 week".

Time	Bi	Pb	Sr	Ca	Cu
3 h	2.11 ± 0.02	0.43 ± 0.01	1.65 ± 0.01	1.91 ± 0.01	2.91 ± 0.02
168 h	2.11 ± 0.02	0.40 ± 0.01	1.68 ± 0.01	1.93 ± 0.01	2.89 ± 0.01
504 h	2.24 ± 0.03	0.26 ± 0.02	1.70 ± 0.01	1.93 ± 0.01	2.87 ± 0.02

Table 16. Composition of Bi-2223 (atom % × $\frac{9}{100}$).

By comparing the change – compared to ∼700 °C – in the background level of the 2θ projection of the "high-cycle run" (Paper 2) at 860 °C with the "1st annealing in 8% O_2" at 830 °C we can estimate the amount of liquid to 5–10% for a "standard annealing". This amount is in agreement with that found by Giannini *et al.* [5].

Due to the fact that the lead amount in Bi-2223 decreases with the annealing time at 650 °C and that the amount of the 3222 phase after 3 weeks is similar to the amount of the transient liquid, one could propose the following reaction scheme during the 3 weeks: (Pb-rich) Bi-2223 + amorphous → (Pb-poor) Bi-2223 + 3222.

Finally, the tape annealed for 3 weeks at 650 °C (sample 4) is investigated by TEM. In this sample a lot of small holes ($\sim 10^{-2}\mu m^2$) has been observed. Some examples are shown in Fig. 60 and Fig. 61. If the ion-milling during preparation of the sample has made these holes then there may have been secondary phases or some other kind of "defects" present prior to the ion-milling. Note that the hole shown to the right in Fig. 60 was found after a second ion-milling of the sample and the other two shown before this second ion-milling. In addition, an amorphous phase between two grains in one colony is observed in the sample (Fig. 62).

EDS in the TEM was used for examination of the phase assembly. For testing the calibration of the EDS the composition of the Bi-2223 phase in the fully processed tape (sample 1) was investigated at different places far away from secondary phases. The amount of Cu was found to be 3.9 instead of ∼3.0 due to the EDS

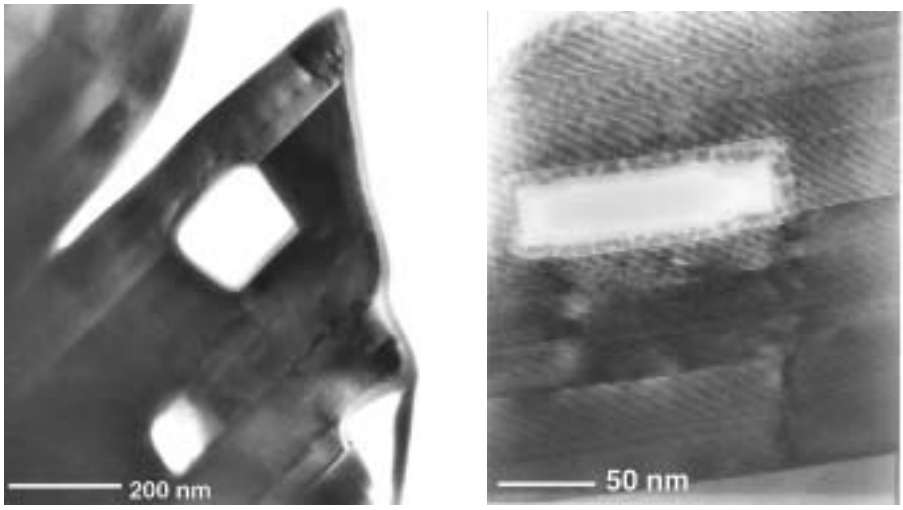

Figure 60. TEM bright field images of sample 4 showing holes.

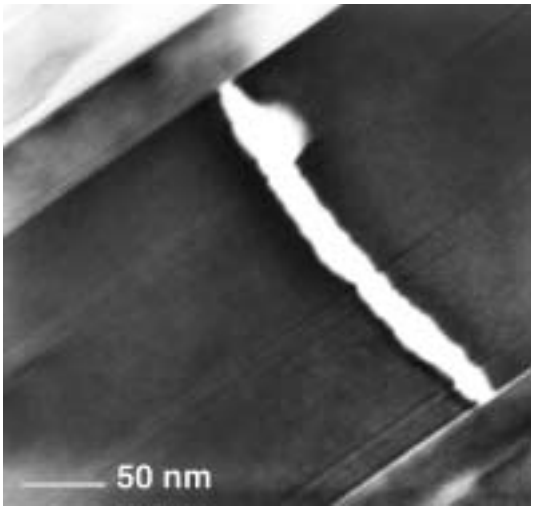

Figure 61. TEM bright field image of sample 4 showing a hole covered the whole grain thickness of 64 unit-cells.

sample holder is made of Cu. Furthermore, the Bi amount was found to be too low[19]. In Fig. 63 is shown an example of a TEM image with the EDS spot analysis. At this particular place a CuO particle is placed next to a Bi-2223 grain. Below the Bi-2223 grain a secondary phase with Sr/Ca $\approx$ 3 and Pb/Ca $\approx$ 1 and some Cu is placed. The Bi-2223 grain was found to contain less Pb than other Bi-2223 grains far away from secondary phases in agreement with Ref. [54]. In addition, secondary phases with Sr/Ca $\approx$ 1 and Sr/Pb $\approx$ 3, Sr/Ca $\approx$ 1 and Sr/Pb $\approx$ 2 (+ Cu) and a Cu-rich amorphous phase with a small amount Bi, Sr and Ca have been observed.

Further TEM studies of the microstructure are needed to further the understanding of the decomposition. A new TEM sample could reveal e.g. whether the observed holes are representative. However, the amorphous phase between grains, a larger amount of small secondary phases (in the size of the Bi-2223 grains) and the lower amount of Pb in Bi-2223 may explain the decrease by approximately a

[19]This has not been corrected since the EDS sample holder first arrived at the end of the TEM study.

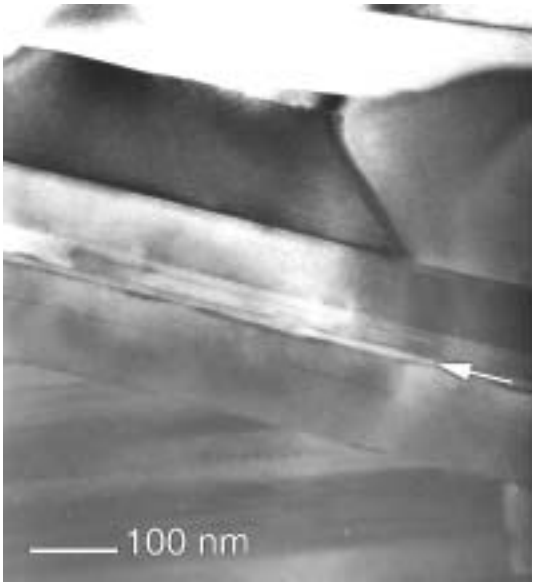

Figure 62. TEM bright field image of sample 4 showing amorphous phase (indicated by the arrow) in between two grains in one colony.

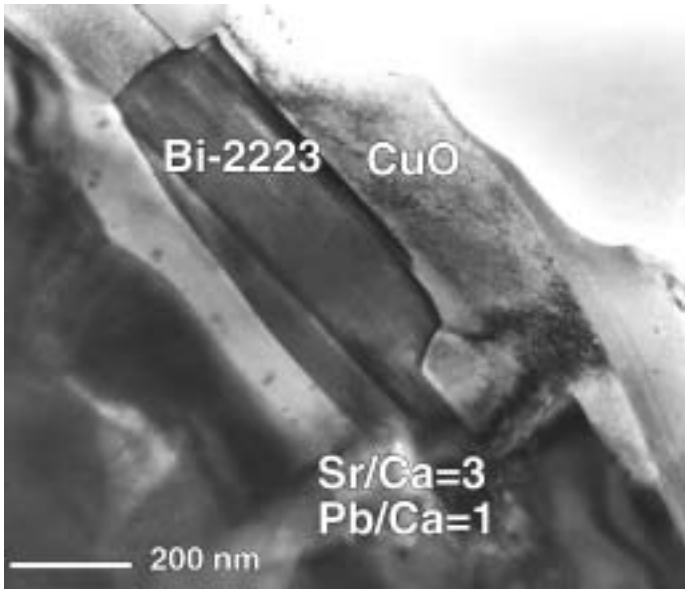

Figure 63. TEM bright field image of sample 4 with EDS analysis showing a Bi-2223 grain in the vicinity of a CuO particle and an other secondary phase.

factor of 2 in the critical current despite no significant decomposition of Bi-2223 is observed.

Since the grain size is proportional to the integrated intensity of a diffraction spot obtained by the 3DXRD microscope, it may be possible to examine whether entire Bi-2223 grains disappear or the decomposition occurs at the grain boundaries by performing a similar decomposition experiment *in situ*. In the first case, some diffraction spots will disappear, and in the second case, the size of the spots will gradually decrease. There is no doubt that the resulting critical current will be the lowest in the latter case.

7 Summary and discussion with outlook

The structural properties of $(Bi,Pb)_2Sr_2Ca_2Cu_3O_x$ (Bi-2223) tapes have been investigated by means of synchrotron X-ray diffraction, transmission electron microscopy (TEM) and scanning electron microscopy (SEM) with energy dispersive X-ray analysis (EDS).

By synchrotron X-ray diffraction *in situ* studies of the phase development during the transformation of $(Bi,Pb)_2Sr_2Ca_1Cu_2O_x$ (Bi-2212) into Bi-2223, the stoichiometry changes and the texture have been performed during annealing in 8% O_2 and in air. Furthermore, an annealing with a slow ramping (from 750 °C) followed by two high temperature cycles has been performed to study the equilibrium phenomena. In addition, a tape beforehand fully converted into Bi-2223 was studied *in situ* during a last annealing.

During heating the residual strain in the Bi-2212 grains is relieved. Between 700 °C and 840 °C the $(Ca,Sr)_2PbO_4$ phase decomposes. Simultaneously, the Bi-2212 lattice contracts, indicating an incorporation of Pb. Moreover, the grain misalignment decreases significantly. During the incorporation of Pb a grain growth of the Bi-2212 phase occurs, explaining the strain release and the texture improvement. In air we have observed that Bi-2212 partly dissociates into $(Ca,Sr)_2CuO_3$ and a liquid phase at temperatures above 812 °C. At the annealing temperature Bi-2212 and the $(Ca,Sr)_2CuO_3$ phase react with the liquid to form Bi-2223. Both in 8% O_2 and in air we have observed that the final texture of Bi-2223 and Bi-2212 is identical, Avrami plots of the transformation kinetics give exponents in the range of 1–2 and the linewidth of Bi-2212 is constant during conversion into Bi-2223, indicating that no strain and finite-size broadening of the diffraction peaks occur. The most probable transformation mechanism is concluded to be a nucleation-and-growth model with a fast decomposition of the individual Bi-2212 grains, followed by a growth of the Bi-2223 phase from the Bi-2212 melt reacting with $(Ca,Sr)_2CuO_3$ (in air and probably 14:24 in 8% O_2). During cooling a precipitation process and a Bi-2223 decomposition take place. Below ∼750 °C in air the $(Ca,Sr)_2CuO_3$ phase and the liquid mainly transform into Bi-2201. Below ∼780 °C Bi-2223 decomposes to 3221. During cooling in 8% O_2 the Bi-2201 phase and $(Ca,Sr)_2PbO_4$ or 3221 are also observed to appear.

By comparing the results obtained in 8% O_2 and in air we have observed a faster reaction rate in the case of 8% O_2. Furthermore, a larger increase in the integrated intensity – which is related to the incorporation of Pb – of the Bi-2212 phase is observed during heating, in agreement with the fact that a lower oxygen partial pressure results in a higher Pb solubility of Bi-2212.

The *in situ* experiment in air where the temperature was cycled between 845 °C and 860 °C has shown that the melting and precipitation process is reversible. However, the reaction of $(Ca,Sr)_2CuO_3$ is less reversible. Moreover, the formation and decomposition kinetics of $(Ca,Sr)_2CuO_3$ are slower than of Bi-2212, Bi-2223 and the liquid phase.

The *in situ* study of the tape beforehand fully converted into Bi-2223 has shown a constant amount of the Bi-2223 phase during annealing. The linewidth and the average grain mis-alignment are also seen to be constant. Furthermore, no stoichiometry changes of Bi-2223 are observed during this last annealing in 8% O_2. The $(Ca,Sr)_2PbO_4$ phase is present during heating until 825 °C.

Using synchrotron radiation and the 3DXRD microscope setup the dynamic behavior of the individual grains within a ceramic was observed for the first time. At 825 °C the diffraction spots from grains appear. In general, it will be feasible to

get information on the transformation mechanism and to study e.g. the kinetics as a function of the stoichiometry, orientation and/or grain size by using the 3DXRD microscope.

In addition, a two-step cooling experiment and a decomposition study have been performed in 8% O_2. The tapes were afterwards investigated by transport current measurements, SEM and synchrotron radiation. Our interpretation of the cooling experiments is that a slow cooling rate to 800 °C provides time for precipitation of a liquid phase used for mass transport when forming the Bi-2223 phase. The decomposition experiment has shown a very slow reaction during post annealing at 650 °C. The amount of the Bi-2223 phase seems to be almost constant. Simultaneously, the amount of a 3222 (Bi = 1.6 and Pb = 1.4) phase is observed to increase. It covers 6% of the Bi-2223 + 3222 area after 3 weeks at 650 °C. The Pb content in Bi-2223 is found to decrease with 40% from 3 h to 3 weeks annealing time. This Pb loss is observed to take place during the last part of the post annealing. The critical current decreases by a factor of 2 during the 3 weeks annealing.

Using TEM, structural parameters such as the grain and colony thickness in the *c*-axis direction and the angles of *c*-axis tilt grain boundaries have been investigated in tapes processed in different ways. By high-resolution TEM the grain and grain boundaries have been investigated on an atomic scale. The intergrowth content and distribution have been examined. It is observed that longer annealing times result in thicker grains and colonies in the *c*-axis direction as well as in smaller angles of the *c*-tilt grain boundaries. The intermediate pressing narrows these parameters, but does not affect the average values within the statistical uncertainty. A fully processed tape has on average 50% thicker grains than a tape after the 1st annealing. The angles of *c*-axis tilt grain boundaries are on average 14° and 26° for the fully processed tape and the tape after the 1st annealing, respectively. The studied microstructural parameters are not fully related to the critical current I_c. Density and connectivity are also crucial for the critical current. The intergrowth content is not responsible for the lower I_c value of the not fully processed tape compared to the value of I_c of the fully processed tape. The content of intergrowth (15%) and the distribution of the different intergrowths (e.g. Bi-2212 and Bi-2234) are the same during the tape processing (after the conversion into Bi-2223) whilst the critical current is increasing.

To further the understanding of the grain growth and the transformation mechanism a future study using high-resolution TEM on tapes quenched (as fast as possible so the liquid does not transform into Bi-2201) at the initial stage of the annealing is suggested.

Since the stability range of the Bi-2223 phase depends on the oxygen partial pressure [25] a possible improvement of the tapes with respect to the critical current value could be reached by reducing the oxygen partial pressure gradually during cooling.

A high intergrowth content (15%) has been observed in the studied tapes. Furthermore, this content does not decrease during further annealing. This points to an optimization of the precursor powder is needed. According to the study by Majewski *et al.* [68] – showing a diffusion of Cu into the silver sheath – the precursor powder has to be regulated in order to compensate the decrease of Cu due to the diffusion.

Instead of focusing on avoiding the high intergrowth content one can focus on improvement of the Bi-2212 phase. Deng *et al.* [69] have improved the critical current density J_c by low temperature–low oxygen pressure post annealing. During the post annealing Pb-poor Bi-2212 transforms to Pb-rich Bi-2212. This formation

has the effect that the T_c value of Bi-2212 increases to 76–80 K, and therefore reduce weak links, since the increased T_c value is $\gtrsim$ the temperature of the liquid nitrogen. This is a new idea of improving the J_c.

The amount of transient liquid during the transformation into Bi-2223 is an important factor for the quality of the fully processed tape. The liquid is necessary during the transformation. On the other hand, a too large amount of liquid will result in an uncontrollable transformation. The observed correlation between the Bi-2212 and the Bi-2223 texture and TEM studies [70] indicate that the Bi-2223 grains are growing on top of the Bi-2212 grains. If the annealing temperature is too high the Bi-2212 grains will decompose too rapidly and the growing Bi-2223 grains will not have the well-aligned Bi-2212 grains as substrate [71]. Zeimetz *et al.* [72] have observed that an annealing in reduced oxygen partial pressure results in a smaller grain size. They interpret this result as the small grain sizes origin in the faster formation of the Bi-2223 grains. A slower Bi-2223 formation rate provides time for recrystallization of the Bi-2212 colonies, which act as substrate for the Bi-2223 growth. In addition, they have found that a higher Bi/Pb ratio results in a larger grain size.

Holesinger *et al.* [73] have observed an initial formation of a Pb-rich liquid in the tape around isolated silver particles within the filaments. They have also observed that the amount of liquid increases with the annealing time and that the liquid is associated primarily with the 14:24 phase (in 8% O_2). Adding silver particles to the precursor powder to obtain initial local liquid away from the silver sheath, and thereby reduce the diffusion path could improve the tape. However, besides the amount of liquid the composition is also important. A sufficient supply of Ca and Cu to the liquid is needed [48].

It could be interesting to examine whether a tape processed with an applied pressure during the conversion into Bi-2223 or just hot-pressed after certain times to avoid heating/cooling several times can improve the tape properties. Zeng *et al.* [74] have hot-pressed tapes – beforehand annealed twice – for 10–360 min. The critical current density in self-field was found to increase significantly. By microstructural analysis they observed an improved grain connectivity, a higher density, a better grain alignment, a recovering of the micro-cracks and a reduction of small-sized secondary phases. However, the hot-pressing creates different types of defects.

For optimization of the tape processing factors such as the powder composition and the particle size, the density, the size of the secondary phases, the grain alignment and the number of filaments are important. Yoo *et al.* [75] have found that a Pb amount of 0.33 in the precursor powder and a particle size of 4 μm give the highest I_c value and conversion into Bi-2223. A particle size of < 2 μm will result in a bad texture [4]. Yamada *et al.* [76] have found a linear relation between J_c and the mass density in the fully processed tape. A density of 75–85% in the green tape is desirable, otherwise the compound cannot be densified afterwards [4]. Small secondary phases will result in a better grain alignment. Many thin filaments that are well-aligned are preferable, since this ensures a high content of silver interfaces with highly aligned Bi-2223 grains [56] that carry most of the current in the tape [58].

Acknowledgements

In Denmark the optimization of the Bi-2223 tapes is carried out in a collaboration between Nordic Superconductor Technologies A/S (NST), Risø National Laboratory (RISØ) and the Technical University of Denmark (DTU). Financial support is provided by the Danish Energy Agency and by the companies ELSAM and ELKRAFT. The synchrotron experiments took place within the framework provided by DANSYNC. The Ph.D. scholarship is granted by the Engineering Science Center for Structural Characterization and Modeling of Materials, Denmark (IVC).

The work and results presented in this thesis are obtained with the helpful assistance of many people. First of all I wish to thank my supervisor senior scientist Henning Friis Poulsen at the Materials Research Department at RISØ. Yi-Lin Liu and Jørgen Bilde-Sørensen have introduced me to the SEM technique. I also wish to thank the technicians at RISØ, especially Helmer Nilsson for preparation of SEM samples and Knud Jensen for furnace support and XRD measurements. Thomas Frello has introduced me to the synchrotron radiation data analysis and has made the ASC'98 conference unforgettable.

NST is gratefully acknowledged for supplying long length Bi-2223 tapes. Without them this project could not have been carried out.

At the beamline BW5 at HASYLAB an enormous support has been provided by Thomas Tschentscher. Thanks to all the other guys at BW5. The work at the beam both day and night wouldn't have been the same without the pleasant company of Thomas Frello, Henning Friis Poulsen, Jean-Claude Grivel, Asger Abrahamsen, Britt Hvolbæk Larsen, Birgitte Abery Jacobsen and Niels Hessel Andersen. At ESRF Ulrich Lienert has provided support.

A big thanks to the group at Electron Microscopy for Materials Science (EMAT) at the University of Antwerp (RUCA) in Belgium. Especially Sara Bals, who has introduced me to the TEM technique and recorded the fantastic high-resolution TEM images. Sara also helped me find a figure skating club, which made my three-month stay in Antwerp even better. Prof. Gustaaf Van Tendeloo, Oleg Lebedev, Freddy Schallenberg, Alexa de Leebeeck, Ludo Rossou and Gertie Stoffelen have all helped me. Ludo and Gertie prepared all the high-quality TEM samples.

I have had many fruitful discussions with Jean-Claude Grivel (who also carried my samples to NST for I_c transport measurements), Yi-Lin Liu, Bruno Kindl, Wei Guo Wang, Jørn Bindslev Hansen, Niels Hessel Andersen and all others attending the RISØ-NST-DTU joint meetings. Thanks to Søren Koch for LaTeX support and to my office-mate Søren Schmidt for good discussions. Finally, I wish to thank the love of my life Rasmus for proof reading this manuscript and for putting up with me every day.

References

[1] T. P. Orlando and K. A. Delin, *Foundations of Applied Superconductivity*, Addison-Wesley Publishing Company, USA, 1991.

[2] C. H. Rosner, Superconductivity: Star Technology for the 21st Century, Oral at the Applied Supercondutivity Conference, Sept. 2000.

[3] W. Hassenzahl, Superconductivity, An Enabling Technology for 21st Century Power Systems?, Oral at the Applied Supercondutivity Conference, Sept. 2000.

[4] R. Flükiger, Phase Formation in Bi,Pb(2223) Tapes, Oral at the Applied Supercondutivity Conference, Sept. 2000.

[5] E. Giannini, E. Bellingeri, R. Passerini, and R. Flükiger, Direct observation of the Bi,Pb(2223) phase formation inside Ag-sheathed tapes and quantitative secondary phase analysis by means of in situ high-temperature neutron diffraction, Physica C **315**, 185–197 (1999).

[6] T. R. Thurston, U. Wildgruber, N. Jisrawi, P. Haldar, M. Suenaga, and Y. L. Wang, Synchrotron x-ray scattering measurements of bulk structural properties in superconducting $(Bi,Pb)_2Sr_2Ca_2Cu_3O_{10}$-Ag tapes, J. Appl. Phys. **79**, 3122–3132 (1996).

[7] T. R. Thurston, P. Haldar, Y. L. Wang, M. Suenaga, N. M. Jisrawi, and U. Wildgruber, *In situ* measurements of texture and phase development in $(Bi,Pb)_2Sr_2Ca_2Cu_3O_{10}$-Ag tapes, J. Mater. Res. **12**, 891–905 (1997).

[8] T. Frello, H. F. Poulsen, L. G. Andersen, N. H. Andersen, M. D. Bentzon, and J. Schmidberger, An *in situ* study of the annealing behaviour of BiSCCO/Ag tapes, Supercond. Sci. Technol. **12**, 293–300 (1999).

[9] H. F. Poulsen, L. G. Andersen, T. Frello, S. Pratontep, N. H. Andersen, S. Garbe, J. Madsen, A. Abrahamsen, M. D. Bentzon, and M. von Zimmermann, In situ study of equilibrium phenomena and kinetics in a BiSCCO/Ag tape, Physica C **315**, 254–262 (1999).

[10] Y. L. Liu, W. G. Wang, H. F. Poulsen, and P. Vase, Microstructure, texture and critical current of Ag-sheathed 2223 multifilament tapes, Supercond. Sci. Technol. **12**, 376–381 (1999).

[11] D. P. Grindatto, *Transmission Electron Microscopic Study of $(Bi,Pb)_2Sr_2Ca_2Cu_3O_x$ Silver-Sheathed Tapes*, Ph.D. thesis, Swiss Federal Institute of Technology Zurich, 1997.

[12] Y. Zhu, M. Suenaga, and R. L. Sabatini, Misorientation angle distributions for large-angle grain boundaries in $Bi_2Sr_2CaCu_2O_8$ and $Bi_2Sr_2Ca_2Cu_3O_{10}$ composite tapes, Appl. Phys. Lett. **65**, 1832–1834 (1994).

[13] B. Hensel, G. Grasso, and R. Flükiger, Limits to the dritical transport current in superconducting $(Bi,Pb)_2Sr_2Ca_2Cu_3O_{10}$ silver-sheathed tapes: The railway-switch model, Phys. Rev. B **51**, 15456–15473 (1995).

[14] P. C. W. Chu, The race for High Temperature Superconductivity, Oral at the Applied Supercondutivity Conference, Sept. 2000.

[15] H. Maeda and K. Togano, *Bismuth-Based High-Temperature Superconductors*, volume 6 of Applied physics, Marcel Dekker, Inc., 270 Madison Avenue, New York, New York 10016, 1996.

[16] N. Kijima, H. Endo, J. Tsuchiya, A. Sumiyama, M. Mizuno, and Y. Oguri, Crystal Structure of the Hich-T_c Phase in the Pb-Bi-Sr-Ca-Cu-O System, Jpn. J. Appl. Phys. **28**, L787–L790 (1989).

[17] J. H. Cho, M. P. Maley, J. O. Willis, J. Y. Coulter, L. N. Bulaevskii, P. Haldar, and L. R. Motowidlo, Determination of the superconducting current path in Bi2223/Ag tapes, Appl. Phys. Lett. **64**, 3030–3032 (1994).

[18] O. Eibl, Crystal structure of $(Bi,Pb)_2Sr_2Ca_{n-1}Cu_nO_{4+2n+\delta}$ high-T_c superconductors, Physica C **168**, 215–238 (1990).

[19] H. W. Zandbergen, W. A. Groen, F. C. Mijlhoff, G. van Tendeloo, and S. Amelinckx, Models for the modulation in $A_2B_2Ca_nCu_{1+n}O_{6+2n}$, A, B=Bi, Sr or Ti, Ba and n=0, 1 ,2, Physica C **156**, 325–354 (1988).

[20] H. W. Zandbergen, W. A. Groen, A. Smit, and G. van Tendeloo, Structure and properties of $(Bi, Pb)_2Sr_2(Ca, Y)Cu_2O_{8+\delta}$, Physica C **168**, 426–449 (1990).

[21] M. D. Bentzon, Z. Han, L. O. Andersen, J. Goul, P. Bodin, and P. Vase, Influence of the Powder Calcination Temperature on the Microstructure in Bi(Pb)-2223 Tapes, IEEE Trans. Appl. Supercond. **7**, 1411–1414 (1997).

[22] M. Takano, J. Takada, K. Oda, H. Kitaguchi, Y. Miura, Y. Ikeda, Y. Tomii, and H. Mazaki, High-T_c Phase Promoted and stabilized in the Bi, Pb-Sr-Ca-Cu-O System, Jpn. J. Appl. Phys. **27**, L1041–L1043 (1988).

[23] M. Mizuno, H. Endo, J. Tsuchiya, N. Kijima, A. Sumiyama, and Y. Oguri, Superconductivity of $Bi_2Sr_2Ca_2Cu_3Pb_xO_y$ (x=0.2, 0.4, 0.6), Jpn. J. Appl. Phys. **27**, L1225–L1227 (1988).

[24] P. Strobel, J. C. Tolédano, D. Morin, J. Schneck, G. Vacquier, O. Monnereau, J. Primot, and T. Fournier, Phase diagram of the system $Bi_{1.6}Pb_{0.4}Sr_2CuO_6$-$CaCuO_2$ between 825°C and 1100°C, Physica C **201**, 27–42 (1992).

[25] U. Endo, S. Koyama, and T. Kawai, Preparation of the High-T_c Phase of Bi-Sr-Ca-Cu-O Superconductor, Jpn. J. Appl. Phys. **27**, L1476–L1479 (1988).

[26] Y. Iwai, Y. Hoshi, H. Saito, and M. Takata, Influence of the oxygen partial pressure on the solubility of PbO in $(Bi,Pb)_2Sr_2CaCu_2O_{\delta+y}$ superconducting oxides, Physica C **170**, 319–324 (1990).

[27] J. Baruchel, J. L. Hodeau, M. S. Lehmann, J. R. Regnard, and C. Schlenker, *Neutron and Synchrotron Radiation for Condensed Matter Studies*, volume 1 HERCULES, Les Editions de Physique, Z.A. de Courtaboeuf, B.P. 112, 91944 Les Ulis Cedex A, France, 1993.

[28] R. Bouchard, D. Hupfeld, T. Lippmann, J. Neuefeind, H. B. Neumann, H. F. Poulsen, U. Rütt, T. Schmidt, J. R. Schneider, J. Süssenbach, and M. von Zimmermann, A triple-crystal diffractometer for high-energy synchrotron radiation at the HASYLAB high-field wiggler beamline BW5, J. Synchrotron Rad. **5**, 90–101 (1998).

[29] http://www.desy.de.

[30] http://www.esrf.fr.

[31] P. Majewski, Phase diagram studies in the system Bi-Pb-Sr-Ca-Cu-O-Ag, Supercond. Sci. Technol. **10**, 453–467 (1997).

[32] P. Majewski, A. Aubele, and F. Aldinger, The influence of Ag on Bi-2212 and Bi-2223, Physica C **341**, 517–518 (2000).

[33] W. Wong-Ng, L. P. Cook, W. Greenwood, and A. Kearsley, Effect of Ag on the primary phase field of the high-T_c (Bi,Pb)-2223 superconductor, J. Mater. Res. **15**, 296–305 (2000).

[34] H. F. Poulsen, T. Frello, N. H. Andersen, M. D. Bentzon, and M. von Zimmermann, Structural studies of BSCCO/Ag-tapes by High-Energy Synchrotron X-ray Diffraction, Physica C **298**, 265–278 (1998).

[35] A. P. Hammersley, S. O. Svensson, M. Hanfland, A. N. Fitch, and D. Häusermann, Two-dimensional detector software: From real detector to idealised image or two-theta scan, High Pressure Research **14**, 235–248 (1996).

[36] M. Hatherly and W. B. Hutchinson, *An Introduction to Textures in Metals*, The Institution of Metallurgists, Monograph No. 5.

[37] O. V. Mishin, E. M. Lauridsen, N. C. K. Lassen, G. Brückner, T. Tschentscher, B. Bay, D. J. Jensen, and H. F. Poulsen, Application of high-energy synchrotron radiation for texture studies, J. Appl. Cryst. **33**, 364–371 (2000).

[38] H. F. Poulsen, S. Garbe, T. Lorentzen, D. J. Jensen, F. W. Poulsen, N. H. Andersen, T. Frello, R. Feidenhans'l, and H. Graafsma, Applications of high-energy synchrotron radiation for structural studies of polycrystalline materials, J. Synchrotron Rad. **4**, 147–154 (1997).

[39] D. J. Jensen, Å. Kvick, E. M. Lauridsen, U. Lienert, L. Margulies, S. F. Nielsen, and H. F. Poulsen, Plastic deformation and recrystallization studied by the 3D x-ray microscope, Mat. Res. Soc. Symp. Proc. **590**, 227–240 (2000).

[40] U. Lienert, C. Schulze, V. Honkimaki, T. Tschentscher, S. Garbe, O. Hignette, A. Horsewell, M. Lingham, H. F. Poulsen, N. B. Thomsen, and E. Ziegler, Focusing optics for high-energy X-ray diffraction, J. Synchrotron Rad. **5**, 226–231 (1998).

[41] P. J. Goodhew and F. J. Humphreys, *Electron Microscopy and Analysis*, Taylor & Francis Ltd, 4 John Street, London WCIN 2ET, 2nd edition, 1992.

[42] D. B. Williams and C. B. Carter, *Transmission Electron Microscopy: A Textbook for Materials Science*, Plenum Press, New York, 233 Spring Street, New York, N. Y. 10013, 1996.

[43] P. Majewski, Materials aspects of the high-temperature superconductors in the system Bi_2O_3–SrO–CaO–CuO, J. Mater. Res. **15**, 854–870 (2000).

[44] Y. Ikeda, H. Ito, S. Shimomura, Z. Hiroi, M. Takano, Y. Bando, J. Takada, K. Oda, H. Kitaguchi, Y. Miura, Y. Takeda, and T. Takada, Phase diagram studies of the $BiO_{1.5}$-PbO-SrO-CaO-CuO system and the formation process of the "2223 (high-T_c)" phase, Physica C **190**, 18–21 (1991).

[45] J.-C. Grivel, A. Jeremie, B. Hensel, and R. Flükiger, Effects of Pb in the first stages of the Bi(2223) phase formation, Supercond. Sci. Technol. **6**, 725–729 (1993).

[46] P. Majewski, H.-L. Su, and F. Aldinger, Engineered flux pinning centres in Pb-doped high temperature superconducting "$Bi_2Sr_2CaCu_2O_8$" ceramics, J. Mater. Sci. **31**, 2035–2042 (1996).

[47] A. Jeremie, K. Alami-Yadri, J.-C. Grivel, and R. Flükiger, Bi,Pb(2212) and Bi(2223) formation in the Bi-Pb-Sr-Ca-Cu-O system, Supercond. Sci. Technol. **6**, 730–735 (1993).

[48] Y. L. Liu, J.-C. Grivel, W. G. Wang, and H. F. Poulsen, Microstructural evolution at the initial stages of annealing in a Bi-2223 multifilament tape, Submitted to Supercond. Sci. Technol. (2001).

[49] W. G. Wang, B. Seifi, Y.-L. Liu, M. Eriksen, P. Skov-Hansen, J.-C. Grivel, and P. Vase, Engineering Critical Current Density Improvement in Ag-Bi-2223 Tapes, Conf. Proc. on Applied Superconductivity Conference 2000 .

[50] T. Fahr, H.-P. Trinks, R. Schneider, and C. Fischer, Investigation of the Formation of the Bi-2223 Phase in Multifilamentary Bi-2223/Ag Tapes by in situ High Temperature Neutron Diffraction, Conf. Proc. on Applied Superconductivity Conference 2000 .

[51] I. Matsubara, R. Funahashi, T. Ogura, H. Yamashita, Y. Uzawa, K. Tanizoe, and T. Kawai, Conversion of $Bi_2Sr_2CaCu_2O_x$ whiskers to the $Bi_2Sr_2Ca_2Cu_3O_x$ phase by annealing in powder, Physica C **218**, 181–190 (1993).

[52] S. X. Dou, R. Zeng, X. K. Fu, Y. C. Guo, J. Horvat, H. K. Liu, T.Beales, and M. Apperley, Critical role of phase transformation during processing of Ag/Bi:2223 tapes, IEEE Trans. Appl. Supercond. **9**, 2436–2439 (1999).

[53] B. Lehndorff, P. Hardenbicker, M. Hortig, and H. Piel, Evidence for enhanced grain connectivity due to second phase reduction of Bi-2223/Ag tapes, Physica C **312**, 105–111 (1999).

[54] T. G. Holesinger, J. F. Bingert, M. Teplitsky, Q. Li, R. Parrella, M. P. Rupich, and G. N. Riley, Jr, Spatial variations in composition in high-critical-current-density Bi-2223 tapes, J. Mater. Res. **15**, 285–295 (2000).

[55] T. G. Holesinger, D. J. Miller, and L. S. Chumbley, Solid solution region of the $Bi_2Sr_2CaCu_2O_y$ superconductor, Physica C **217**, 85–96 (1993).

[56] F. Yi, Y. E. High, D. C. Larbalestier, Y. S. Sung, and E. E. Hellstrom, Evidence for preferential formation of the $(Bi,Pb)_2Sr_2Ca_2Cu_3O_x$ phase at the Ag interface in Ag-sheathed $(Bi,Pb)_2Sr_2Ca_2Cu_3O_x$ tapes, Appl. Phys. Lett. **62**, 1553–1555 (1993).

[57] Y. Yamada, J. Q. Xu, J. Kessler, E. Seibt, W. Goldacker, W. Jahn, and R. Flükiger, Microstructual and transport-properties of high-J_c Bi(2223)Ag tapes, Physica C **185**, 2483–2484 (1991).

[58] M. Lelovic, P. Krishnaraj, N. G. Eror, and U. Balachandran, Minimum critical-current density of 10^5 A/cm^2 at 77 K in the thinlayer of $Bi_{1.8}Pb_{0.4}Sr_{2.0}Ca_{2.2}Cu_{3.0}O_y$ superconductor near the Ag in Ag-sheathed tapes, Physica C **242**, 246–250 (1995).

[59] M. Eriksen, J. I. Bech, N. Bay, and P. Skov-Hansen, Flat rolling of round and square superconducting multifilaments for HTS tapes, Conf. Proc. on 4th European Conference on Applied Superconductivity 1999 .

[60] L. G. Andersen, S. Bals, G. van Tendeloo, H. F. Poulsen, and Y. L. Liu, Transmission electron microscopy investigation of Bi-2223/Ag tapes, Physica C **353**, 251–257 (2001).

[61] P. Majewski, S. Kaesche, and F. Aldinger, Fundamentals of the Preparation of High-T_c Superconducting $(Bi,Pb)_{2+x}Sr_2Ca_2Cu_3O_{10+\delta}$ Ceramics, Adv. Materials **8**, 762–765 (1996).

[62] W. G. Wang, J. Horvat, B. Zeimetz, H. K. Liu, and S. Dou, Effect of $(Bi,Pb)_2Sr_2CuO_6$ phase on critical current density of $Ag/(Bi,Pb)_2Sr_2Ca_2Cu_3O_x$ tapes", Physica C **291**, 1–7 (1997).

[63] W. G. Wang, J. Horvat, J. N. Li, H. K. Liu, and S. X. Dou, Effect of $(Bi,Pb)_3Sr_2Ca_2CuO_6$ phase on critical current density of $Ag/(Bi,Pb)_2Sr_2Ca_2Cu_3O_x$ tapes, Physica C **297**, 1–9 (1998).

[64] J.-C. Grivel and R. Flükiger, Factors influencing the apparent activation energy for the formation of the $(Bi,Pb)_2Sr_2Ca_2Cu_3O_{10}$ compound, J. Alloys and Comp. **241**, 127–134 (1996).

[65] Y. Kusano, T. Nanba, J. Takada, T. Egi, Y. Ikeda, and M. Takano, Segregation and dissolution reaction of the 2223 phase in the Bi,Pb-Sr-Ca-Cu-O system on annealing in air, Physica C **219**, 366–370 (1994).

[66] H. K. Liu, R. Zeng, X. K. Fu, and S. X. Dou, Phase transformation and liquid phase conversion during the final processing of Bi-2223/Ag PIT tapes and their influence on critical current density, Physica C **325**, 70–76 (1999).

[67] T. G. Holesinger, J. F. Bingert, J. O. Willis, Q. Li, R. D. Parrella, M. D. Teplitsky, M. W. Rupich, and J. Gilbert N. Riley, Structural and Compositional Defects in High-J_c Bi-2223 Tapes, IEEE Trans. Appl. Supercond. **9**, 2440–2445 (1999).

[68] P. Majewski, A. Aubele, T. Fahr, and F. Aldinger, Diffusion of Cu into Ag sheath of BPSCCO tapes, Physica C **325**, 8–12 (1999).

[69] H. Deng, P. W. Hua, W. Q. Wang, C. Dong, H. Chen, F. Wu, X. H. Wang, Y. R. Zhou, and G. S. Yuan, Influence of low temperature-low oxygen pressure postannealing on critical current density of Bi(Pb)2223/Ag superconductors, Physica C **339**, 181–194 (2000).

[70] D. P. Grindatto, J.-C. Grivel, G. Grasso, H.-U. Nissen, and R. Flükiger, TEM study of the $(Bi,Pb)_2Sr_2Ca_2Cu_3O_x$ phase formation in $(Bi,Pb)_2Sr_2Ca_2Cu_3O_x$ silver-sheathed tapes, Physica C **298**, 41–48 (1998).

[71] J.-C. Grivel, H. F. Poulsen, L. G. Andersen, T. Frello, N. H. Andersen, E. Giannini, D. P. Grindatto, and R. Flükiger, Investigations on the formation mechanism of the Bi(2223) phase in bulk samples and Ag-sheathed tapes, Proc. on Int. Workshop on Superconductivity, Okinawa, July 12-15, Japan (1998).

[72] B. Zeimetz, S. X. Dou, and H. K. Liu, Recrystallization effects and grain size in Bi-2223 tapes, Supercond. Sci. Technol. **11**, 1082–1086 (1998).

[73] T. G. Holesinger, A. Ayala, R. M. Baurceanu, and V. A. Maroni, Investigation of the Initial Stages of Processing Bi-2223 Multifilamentary Tapes by Analytical Electron Microscopy, Conf. Proc. on Applied Superconductivity Conference 2000 .

[74] R. Zeng, B. Ye, J. Horvat, Y. C. Guo, B. Zeimetz, X. F. Yang, T. P. Beales, H. K. Liu, and S. X. Dou, Grain connectivity and flux pinning in Bi-2223/Ag PIT tapes, Physica C **307**, 29–45 (1998).

[75] J. Yoo, Effects of lead content and particle size of precursor powders on formation rate, grain growth and critical current density of BSCCO 2223 tapes, Oral at the Applied Supercondutivity Conference, Sept. 2000.

[76] Y. Yamada *et al.*, Adv. Supercond. **VI**, 609 (1994).

List of papers

Paper 1
T. Frello, H.F. Poulsen, L. Gottschalck Andersen, N.H. Andersen, M.D. Bentzon and J. Schmidberger, *An in situ study of the annealing behaviour of BiSCCO/Ag tapes*, Supercond. Sci. Techn. 12, 293–300 (1999).

Paper 2
H.F. Poulsen, L. Gottschalck Andersen, T. Frello, S. Pratontep, N.H. Andersen, S. Garbe, J. Madsen, A. Abrahamsen, M.D. Bentzon and M. von Zimmermann, *In situ study of equilibrium phenomena and kinetics in a BiSCCO/Ag tape*, Physica C 315, 254–262 (1999).

Paper 3
L. Gottschalck Andersen, H.F. Poulsen, T. Frello, N.H. Andersen and M. von Zimmermann, *Cooling Behavior of BSCCO/Ag Tapes*, IEEE Trans. Appl. Supercond. 9, 2758–2761 (1999).

Paper 4
L. Gottschalck Andersen, S. Bals, G. Van Tendeloo, H.F. Poulsen and Y.L. Liu, *Transmission electron microscopy investigation of Bi-2223/Ag tapes*, Physica C 353, 251–257 (2001).

Bibliographic Data Sheet **Risø–R–1271(EN)**

Title and author(s)

Structural Properties of Superconducting Bi-2223/Ag Tapes

Lotte Gottschalck Andersen

ISBN	ISSN
87–550–2888–8; 87–550–2889–6 (Internet)	0106–2840

Dept. or group	Date
Materials Research Department	May 2001

Groups own reg. number(s) Project/contract No.

Pages	Tables	Illustrations	References
79	16	63	76

Abstract (Max. 2000 char.)

The structural properties of silver clad high-T_c superconducting ceramic tapes of $(Bi,Pb)_2Sr_2Ca_2Cu_3O_x$ (Bi-2223) have been investigated by means of synchrotron X-ray diffraction (including the 3DXRD microscope setup), transmission electron microscopy (TEM) and scanning electron microscopy (SEM) with energy dispersive X-ray analysis (EDS). By synchrotron X-ray diffraction *in situ* studies of the phase development during the transformation of $(Bi,Pb)_2Sr_2Ca_1Cu_2O_x$ (Bi-2212) into Bi-2223, the stoichiometry changes and the texture have been performed during annealing in 8% O_2 and in air. Furthermore, an annealing with two high temperature cycles has been performed to study the equilibrium phenomena. During heating $(Ca,Sr)_2PbO_4$ decomposes at temperatures between 700 °C and 840 °C. Simultaneously, the Bi-2212 lattice contracts, indicating an incorporation of Pb. Moreover, the grain mis-alignment decreases significantly. In air we have observed that Bi-2212 partly dissociates into $(Ca,Sr)_2CuO_3$ and a liquid at temperatures above 812 °C. At the annealing temperature Bi-2212 and $(Ca,Sr)_2CuO_3$ react with the liquid to form Bi-2223. The transformation mechanism is discussed. During cooling below ∼750 °C $(Ca,Sr)_2CuO_3$ and the liquid mainly transform into Bi-2201. Below ∼780 °C Bi-2223 decomposes to 3221. In addition, a two-step cooling experiment and a decomposition study have been performed in 8% O_2. By TEM the grain and colony size in the *c*-axis direction, the angles of *c*-axis tilt grain boundaries and the intergrowth content are investigated. A fully processed tape has on average 50% thicker grains than a tape after the 1st annealing. The angles of *c*-axis tilt grain boundaries are on average 14° and 26° for the fully processed tape and the tape after the 1st annealing, respectively. The intergrowth content (15%) and distribution are similar in these two tapes.

Descriptors INIS/EDB

Bismuth compounds; Cooling; Critical current; Grain growth; Grain size; High-Tc superconductors; Phase transformations; Scanning electron microscopy; Synchrotron radiation; Texture; Transmission electron microscopy; X-ray diffraction.

Available on request from:
Information Service Department, Risø National Laboratory
(Afdelingen for Informationsservice, Forskningscenter Risø)
P.O. Box 49, DK–4000 Roskilde, Denmark
Phone (+45) 46 77 46 77, ext. 4004/4005 · Fax (+45) 46 77 40 13